Aerodynamic Characteristics Estimation of Variable Geometry Airfoil in Supersonic Air Flow

Matak, Leo

UNIVERSITY OF ZAGREB
FACULTY OF TRANSPORT AND TRAFFIC SCIENCES

Leo Matak

AERODYNAMIC CHARACTERISTICS ESTIMATION OF VARIABLE GEOMETRY AIRFOIL IN SUPERSONIC AIR FLOW

GRADUATE THESIS

Zagreb, 2021.

UNIVERSITY OF ZAGREB
FACULTY OF TRANSPORT AND TRAFFIC SCIENCES
MASTER THESIS COMMITTEE

Zagreb, 27 April 2021

MASTER THESIS ASSIGNMENT No. 6257

Student: **Leo Matak (0135240437)**
Study: Aeronautics

Title: **Aerodynamic Characteristics Estimation of Variable Geometry Airfoil in Supersonic Air Flow**

Description:

Supersonic airfoils are designed to achieve maximum efficiency in design flight regimes.They can be of different thickness, curvature, and at different angles of attack. It is necessary to analyze the influence of airfoil geometry on the coefficient of pressure, drag, and lift in the supersonic airflow considering linearized supersonic flow over a thin airfoil at a low angle of attack and using a CFD software program. The results should be compared and commented on.

Mentor: Committee Chair:

Assistant Professor Karolina Krajček Nikolić, PhD

University of Zagreb
Faculty of Transport and Traffic Sciences

GRADUATE THESIS

AERODYNAMIC CHARACTERISTICS ESTIMATION OF VARIABLE GEOMETRY AIRFOIL IN SUPERSONIC AIR FLOW

Mentor: doc. dr. sc. Karolina Krajček Nikolić

Student: Leo Matak
JMBAG: 0135240437

Zagreb, May 2021

Abstract

The primary objective of this research project is to evaluate the aerodynamics behavior of the NACA 64_A-204 airfoil used in the F-16 wings. The reason for selecting the F-16 wing, and therefore the airfoil used in the wing, is the characteristic behavior of in-flight changes to the airfoil geometry. The changes are made by deflecting the leading and trailing edge flaps which result in changing the wing and airfoil geometry.

Two approaches were selected for obtaining the results. Linearized supersonic airfoil theory and Computational Fluid Dynamics. Linear theory offers concise results but with certain limitations, such as thin airfoil and small angles of attack. CFD solves for full Navier-Stokes equations taking into account viscosity, wall shear and stresses; which are not found in the linear theory terms.

Lift coefficient values obtained are very similar for both approaches, what differs them is the drag value. As expected, the CFD approach gives higher values for drag. However, it is worth noting how the linear theory offers almost identical results for both drag and lift values under certain conditions which do not go over the imposed limitations.

The paper reveals how the change in the airfoil geometry, when going from subsonic to supersonic flight, affects the lift to drag ratio. It is shown how for supersonic flight regime the supersonic flight configuration provides over 10% higher value for CL/CD ratio at 1-degree angle of attack based on the CFD results, and over 6% higher value for the same conditions based on the linear theory. Such an increase is detrimental for combat aircraft which rely on afterburner and heavy fuel consumption.

Key words: F-16, NACA 64_A-204, Supersonic linear airfoil theory, cambered airfoil, CFD

Sažetak

Cilj ovog rada bio je procjena promjene aerodinamičkih karakteristika aeroprofila NACA 64_A-204 korištenog u krilima borbenog zrakoplova F-16. Razlog odabira krila F-16 jest njegova mogućnost promjene geometrije krila tijekom leta. Mjenjajući položaj prednjih i stražnjih krilaca zrakoplov ima mogućnost promjene zakrivljenosti aeroprofila, pa tako i krila.

Dva su pristupa korištena za proračune koeficijenata. Linearizirana teorija nadzvučnog aeroprofila i metode Računalne Dinamike Fluida (CFD). Linearna teorija pruža dosta točne rezultate ali pri određenim ograničenja kao što su – tanki aeroprofili i mali napadni kutovi. Računalna dinamika fluida nema takvih ograničenja, i rezultate dobiva rješavajući kompletne Navier-Stokes jednadžbe uzimajući u obzir sile viskoznosti, trenja i naprezanja.

Rezultati dobiveni za koeficijente uzgona dosta su slični u oba pristupa, ono što ih razlikuje su vrijednosti koeficijenta otpora. Očekivano, CFD pristup daje veće vrijednosti otpora. Međutim, bitno je istaknuti kako linearna teorija pruža gotovo identične rezultate i za uzgon i za otpor pri određenim uvjetima koji ne idu iznad ograničenja teorije.

Na kraju rada prikazano je kako i koliko utječe promjena u geometriji aeroprofila pri prelasku iz podzvučnog u nadzvučan let. Pokazano je kako za režim nadzvučnog kruziranja konfiguracija sa smanjenom zakrivljenosti – konfiguracija za nadzvučno kruziranje – pruža i preko 10% veći odnos Cl/Cd za napadni kut od 1 stupanj na temelju CFD rezultata, i preko 6% veći odnos predviđen linearnom teorijom za iste uvjete. Za borbene zrakoplove koji dosta zavise o potrošnji goriva i korištenju učinaka afterburner-a, takvo povećanje je dosta bitno.

Ključne riječi: F-16, NACA 64_A-204, linearna teorija nadzvučnog aeroprofila, zakrivljeni aeroprofil, računalna dinamika fluida

Table of contents

1. Introduction

Ever since the first development of heavier-than-air aircraft the study of the aerodynamic design has played a major role. From the first successful flight performed by the Wright brothers, it has been an ongoing quest for the aerodynamicists to find and develop a design or a shape of wings which could provide better performances for specified flight regimes.

Traditionally it has been in the hands of the designer's experience, flight tests and wind tunnel experiments to provide a method of systematic study and to create a way of making inexpensive adjustments to key parameters in designing of lift generating surfaces. As the years passed, so did the technology advanced forward. We now live in a very modern, high-tech, computerized world where most of the scientific calculations are done using highly advanced software which incorporates all the theoretical and numerical knowledge amassed throughout the years of scientific development. At the present time, Computational Fluid Dynamics has come to complement the experimental studying, reducing the cost in tests and time for the generations of aircraft to come.

This paper will focus on a study of the NACA 64_A-204 airfoil used by the F-16 aircraft. The specified airfoil is selected because during the flight, the F-16 has an ability to change the geometry of its wings, and thus its airfoil, by deflecting the leading or trailing edge flaps or both. By doing so it effectively changes the curvature and the camber line of the airfoil. And since the curvature and camber line have a significant impact on the airfoil characteristics, it results in changes in lift, drag and pressure coefficients.

Theoretical analysis will be presented at the beginning, explaining how and why the flow is classified based on the Mach number, and what is the connection between Mach number, speed of sound and compressibility of the fluid. Afterwards a more detailed explanation about the airfoil and its name is given. Then, the linearized theory along with its restrictions and applicability is explained. The analytical terms on which the theory is based are derived from the fundamental formula of the thin airfoil theory. Finally, MATLAB software is introduced along with the code used to compute the lift, drag and pressure coefficients. Results obtained via linearized theory through MATLAB are given at the end of chapter 3.

Next major chapter is the Computational Fluid Dynamics part. After a brief introduction along with the history of development, core principles are discussed and explained. It is shown how the CFD software goes from differential equations of the fluid flow, which are based on the century old conservation laws, all the way to extracting the desired variables in the flow field. Furthermore, the ANSYS Fluent software is introduced and it is disseminated how it was used for obtaining results relevant to this study. Everything from importing and creating the airfoil geometry, to post-processing and result obtaining is discussed. CFD obtained results are then given for supersonic cruise, along with some figures for subsonic cruise.

In the discussion part, the results obtained by linearized theory and the results obtained by the computational fluid dynamics are compared and discussed. It is shown when and why the results align best, and when do the discrepancies occur. Since the results obtained by both approaches were as predicted, it can be stated how the study was conducted successfully.

Finally, the conclusion chapter gives the final remarks and insights obtained by conducting the study.

2. Supersonic airfoil theory

This chapter gives brief explanation of how the flow is classified based on Mach number, and how does the value of Mach number determine the compressibility of the flow. It is then shown how the Mach number, compressibility and speed of sound are connected, and why is that connection important. Furthermore, the airfoil studied in this paper is disseminated along with its codename. It is explained how and why it is used in the F-16 aircraft. Finally, linearized theory which is based on the thin airfoil theory is explained and discussed along with the analytical terms on which the theory is based. MATLAB analysis is expanded at the end by commenting how the analytical terms can be used for computations of major aerodynamical coefficients, such as lift and drag coefficients.

2.1. Flow classification

In the twentieth century, manned flight has been a major impetus for the advancement of fluid dynamics in general, and compressible flow in particular. Hence, although the fundamentals of compressible flow are applied to a whole spectrum of modern engineering problems, their application to aerodynamics and propulsion geared to airplanes and missiles is frequently encountered [1].

It is useful to illustrate different regimes of compressible flow by considering an aerodynamic body in a flowing gas, as sketched in Fig. 1. Let us define certain definitions first. Far away from the body, the flow is uniform with a freestream *velocity* V_∞,. *A streamline* is a curved line in the flow field that is tangential to the vector of local velocity *V* at every point along the streamline. Figure 1. illustrates only a few of the infinite number of streamlines around a body.

Now think of an arbitrary point in the flow field, where *p*, *T*, ρ, and *V* are local pressure, temperature, density, and vector velocity at that point. All of these values are point characteristics and vary from one point to another on the streamline. If *a*, is the speed of sound in the uniform free stream, then the ratio V_∞/a_∞defines the free-stream Mach number Ma_∞. In a very similar matter, the local Mach number M is defined as M = *V/a*, and varies from point to point in the flow field. Further physical importance of Mach number will be discussed later. In the present chapter value *M* simply will be used to define four different fluid flow regimes [1].

Subsonic flow

Consider the flow over an airfoil section as sketched in fig. 1.a. The local Mach number is everywhere less than one. Such a flow regime where $M < 1$ at every point in the flow field, and subsequently the entire flow velocity field is less than the speed of sound is defined as *subsonic* flow. This type of flow is defined by smooth streamlines along the entire surface of the airfoil. Note that the initially straight and parallel streamlines in the free stream begin to deflect far upstream of the body. It is like the flow that is about to touch the airfoil is forewarned of the presence of the body. This is an important property of subsonic flows. Also, as the flow

passes over the airfoil, the local velocity and Mach number on the top surface increase above their free-stream values. However, if *M*, is sufficiently less than 1 the local Mach number everywhere will remain subsonic. For airfoils in common use, if $M <= 0.8$, the flow field can be considered completely subsonic. It can be stated how for aerodynamics engineers, the subsonic regime is defined with a free stream where $M<=0.8$.

Transonic flow

If M_∞, remains subsonic, but is sufficiently near 1, the flow expansion over the top surface of the airfoil may result in local areas with supersonic velocities, as sketched in fig. 1.b. Such a combination of flow velocities is defined as *transonic flow.* In fig. 1.b, M_∞, is less than 1 but high enough to produce a region of locally supersonic flow. In most cases, as sketched in fig. 1.b, this part of the supersonic region is terminated with a normal shock wave across which there are discontinuous and sometimes rather drastic changes in flow properties. If M_∞, is increased to slightly above one, the shock position will move more to the rear part, or the trailing edge of the airfoil, and a second shock wave may appear in front of the leading edge. This second shock wave is called the bow *shock,* and is sketched in Fig. 1.c. In front of the bow shock, the streamlines are straight and parallel, with a uniform supersonic free-stream Mach number. In passing through that part of the bow shock that is nearly normal to the free stream, the flow becomes subsonic. However, an extensive supersonic region again forms as the flow expands over the airfoil surface, and again terminates with a trailing-edge shock. Both flow patterns sketched in Figs. 1.b and *c* are characterized by mixed regions of locally subsonic and supersonic flow. Such mixed flows are defined as *transonic flows***,** and $0.8 < M_\infty < 1.2$ is loosely defined as the *transonic regime.*

Supersonic flow

A flow field where $M_\infty > \mathbf{1}$ everywhere is defined as *supersonic*. Observe the supersonic flow over the wedge-shaped body in Fig. 1.d. A straight, oblique shock wave is attached to the sharp nose of the wedge. Across this shock wave, the streamline direction changes discontinuously. Ahead of the shock, the streamlines are straight, parallel, and horizontal; behind the shock they remain straight and parallel but in the direction of the wedge surface. Unlike the subsonic flow in Fig. 1.a, the supersonic uniform free stream is not forewarned of the presence of the body until the shock wave is encountered. The flow is supersonic both upstream and (usually, but not always) downstream of the oblique shock wave. There are dramatic physical and mathematical differences between subsonic and supersonic flows.

Hypersonic flow

The temperature, pressure, and density of the flow increase almost explosively across the shock wave shown in Fig. 1.d. As $\boldsymbol{M}$ is increased to higher supersonic speeds, these increases become more severe. At the same time, the oblique shock wave moves closer to the surface, as sketched in Fig. 1.e. For values of $\boldsymbol{M} > 5$, the shock wave is very close to the surface, and the flow field between the shock and the body (the shock layer) becomes very hot-indeed,

hot enough to dissociate or even ionize the gas. These effects-thin shock layers and hot, chemically reacting gases - add complexity to the analysis of such flows. For this reason, the flow regime for $\boldsymbol{M} > 5$ is given a special label-hypersonic flow. The choice of $\boldsymbol{M} = 5$ as a dividing point between supersonic and hypersonic flow is a rule of thumb. In reality, the special characteristics associated with hypersonic flow appear gradually as $\boldsymbol{M}$ is increased, and the Mach number at which they become important depends greatly on the shape of the body and the free-stream density [1].

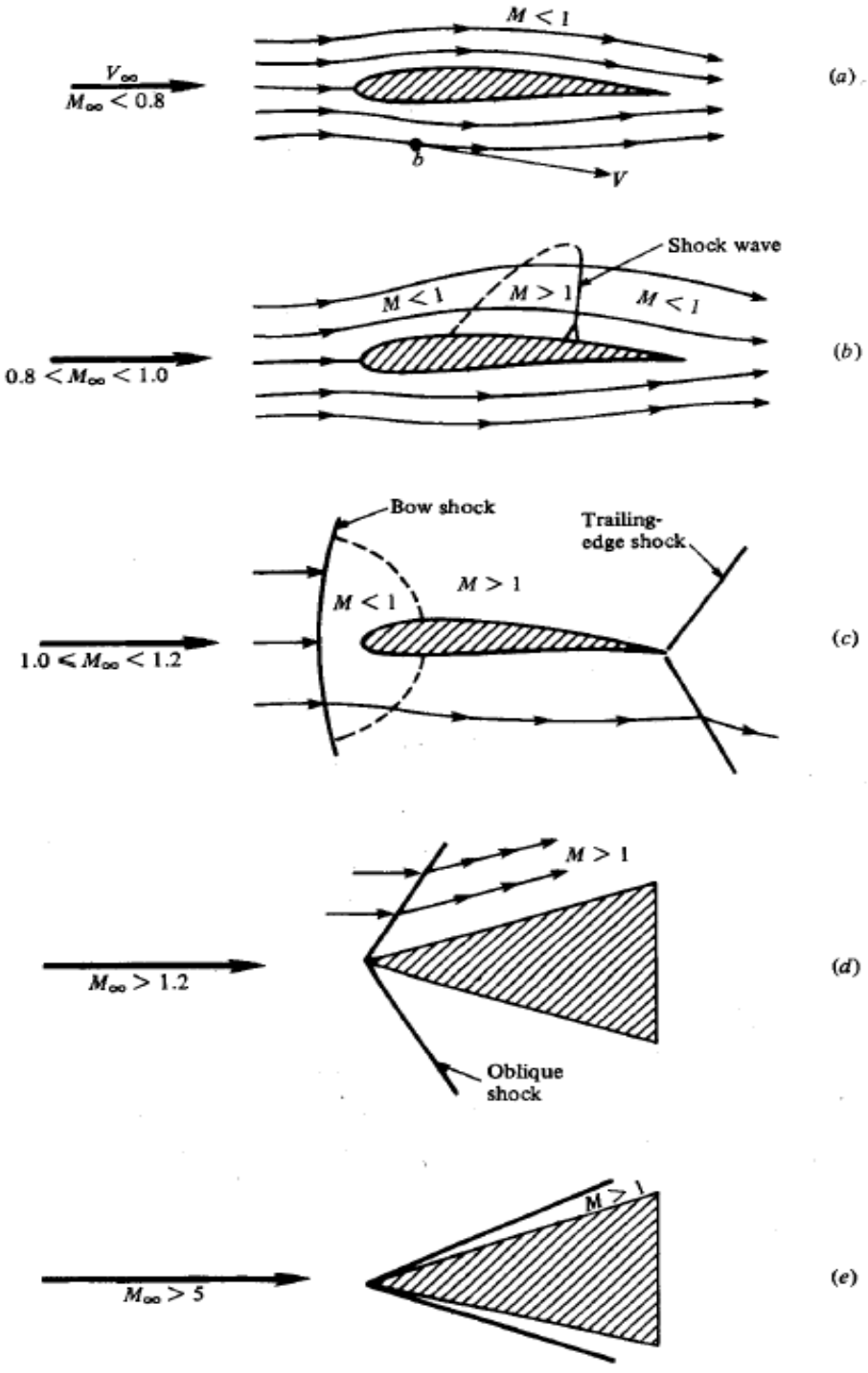

Figure 1. Flow regimes

There are other ways of classifying flow fields. For example, flows where the effects of viscosity, thermal conduction, and mass diffusion are important are called **viscous flows**. Such phenomena are dissipative effects that change the entropy of the flow, and are important in regions of large gradients of velocity, temperature, and chemical composition. Examples are boundary layer flows, flow in long pipes, and the thin shock layer on high-altitude hypersonic vehicles. Friction drag, flow field separation, and heat transfer all involve viscous effects. Therefore, viscous flows are of major importance in the study of fluid dynamics. In contrast, flows in which viscosity, thermal conduction, and diffusion are ignored are called **inviscid flows**. At first glance, the assumption of inviscid flows may appear highly restrictive; however, there are a number of important applications that do not involve flows with large gradients, and that readily can be assumed to be inviscid. Examples are the large regions of flow over wings and bodies outside the thin boundary layer on the surface, flow through wind tunnels and rocket engine nozzles, and the flow over compressor and turbine blades for jet engines. Surface pressure distributions, as well as aerodynamic lift and moments on some bodies, can be accurately obtained by means of the assumption of inviscid flow [1] [2].

In this study, calculations will be made both with viscous and inviscid flow treatment. It will also be shown how the linear theory which doesn't include viscous effects is very accurate in certain conditions, such as thin airfoils with small angles of attack. For the viscous part of the calculations, numerical analysis will be conducted by using the Ansys FLUENT software.

2.1.1. Speed of sound

The air is composed of molecules that are moving about in a random motion with different instantaneous velocities and energies at different times. However, over a period of time, the average (mean) molecular velocity and energy can be defined. If there was a source of instantaneous energy expansion (e.g. explosion) somewhere in the room which is filled with air – the air molecules would absorb the energy in a way that they would increase their velocity and internal energy and thus started to collide with neighboring molecules. Those neighboring molecules would then continue to collide with molecules adjacent to them, and the process would go on until all of the energy released by the energy source isn't absorbed – and during the process the mean velocity of the air would be increased. Through the wave, the energy increase also causes the pressure (as well as density, temperature, etc.) to change slightly. If there was a human nearby, he would pick up that waves change in pressure with his ears – sound wave. The speed of sound through a gas is one of the most important quantities in a study of compressible flow.

Because there are changes in the flow properties through the wave, the flow behind the wave moves away at a different velocity. These changes can be depicted from the figure 2. However, these changes are slight. A sound wave, by definition, is a weak wave. If the changes through the wave are strong, it is identified as a shock wave, which propagates at a higher velocity than the speed of sound. Therefore, it is considered that the change in velocity through the sound wave is an infinitesimal quantity, *da*.

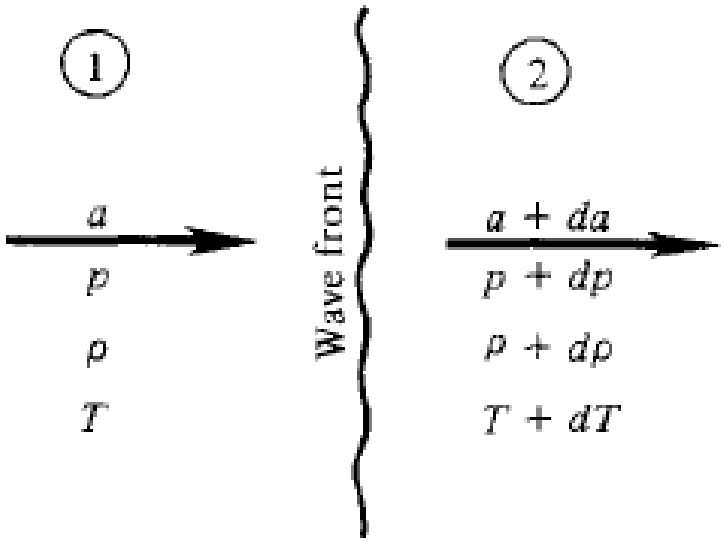

Figure 2. Schematic of a sound wave

Considering that, the changes within the wave are slight, i.e., the flow gradients are small. This implies that the irreversible, dissipative effects of friction and thermal conduction are negligible. Moreover, there is no heat addition to the flow inside the wave (the gas is not being irradiated by a laser, for example). Hence, the process inside the sound wave must be isentropic. In turn, the rate of change of pressure with respect to density, $dp/d\rho$, can be seen as an isentropic process, and the relation is shown in equation 1 [1] [2].

$$a^2 = \left(\frac{dp}{d\rho}\right)_s \tag{1}$$

Equation (1) is a fundamental expression for the speed of sound. It shows that the speed of sound is a direct measure of the compressibility of a gas.
It can be expanded using terms such as: $\rho = 1/v,\ d\rho = -dv/u^2$ to become:

$$a = \sqrt{\frac{\partial p}{\partial \rho}} = \sqrt{\frac{v}{\tau_s}} \tag{2}$$

Where v is specific volume. The term (2) implies that incompressible flow ($\tau_s = 0$) happens when the speed of sound goes to infinity. Furthermore, by including the equation of state: $p/\rho = RT$ into the previous equation:

$$a = \sqrt{\gamma RT} \tag{3}$$

This equation holds true only for calorically perfect gasses. It gives the speed of sound as a function of temperature only. It is worth noting how the speed of sound in air at standard sea level conditions is $a = 340{,}9$ m/s

Finally, the reason why the speed of sound is explained is because of its contribution to calculating the Mach number, because $M = V/a$ which leads to the general flow classification:

$$M < 1 \text{ (subsonic flow)}$$
$$M = 1 \text{ (sonic flow)}$$
$$M > 1 \text{ (supersonic flow)}$$

2.1.2. Compressibility

The compressibility is generically defined as:

$$\tau = -\frac{1}{v}\frac{dv}{dp} \tag{4}$$

Hence:

$$d\rho = \rho\tau dp \tag{5}$$

Which means that the flow must be treated as compressible when the pressure gradients in the flowfield are large enough such that, in combination with a large enough value of the compressibility, τ, the resulting density changes are too large to ignore. For gases, this occurs when the flow Mach number is greater than about 0.3. In short, for high-speed flows, the density becomes a variable; such variable-density flows are called *compressible flows*.

High-speed, compressible flow is also high-energy flow. Thermodynamics is the science of energy and entropy; hence a study and application of compressible flow involves a coupling of purely fluid dynamic fundamentals with the results of thermodynamics.

Compressible flow pertains to flows at Mach numbers from 0.3 to infinity. In turn, this range of Mach number is subdivided into four regimes, each with its own distinguishing physical characteristics and different analytical methods [1]. These regimes were discussed earlier, and they are: subsonic, transonic, supersonic and hypersonic flow. This paper is based on subsonic and supersonic regimes.

2.2. NACA 6 series airfoils

The early NACA airfoil series, the 4-digit, 5-digit, and modified 4-/5-digit, were generated using analytical equations that describe the camber (curvature) of the mean-line (geometric centerline) of the airfoil section as well as the section's thickness distribution along the length of the airfoil. Later families, including the 6-Series, are more complicated shapes derived using theoretical rather than geometrical methods. Before the National Advisory Committee for Aeronautics (NACA) developed these series, airfoil design was rather arbitrary with nothing to guide the designer except past experience with known shapes and experimentation with modifications to those shapes.

This methodology began to change in the early 1930s with the publishing of a NACA report entitled *The Characteristics of 78 Related Airfoil Sections from Tests in the Variable Density Wind Tunnel* [3]. In this landmark report, the authors noted that there were many similarities between the airfoils that were most successful, and the two primary variables that affect those shapes are the slope of the airfoil mean camber line and the thickness distribution above and below this line. They then presented a series of equations incorporating these two variables that could be used to generate an entire family of related airfoil shapes. As airfoil design became more sophisticated, this basic approach was modified to include additional variables, but these two basic geometrical values remained at the heart of all NACA airfoil series, as illustrated below in fig. 3 [4].

Although NACA experimented with approximate theoretical methods that produced the 2-Series through the 5-Series, none of these approaches was found to accurately produce the desired airfoil behavior.

The 6-Series was derived using an improved theoretical method that, like the 1-Series, relied on specifying the desired pressure distribution and employed advanced mathematics to derive the required geometrical shape. The goal of this approach was to design airfoils that maximized the region over which the airflow remains laminar. In so doing, the drag over a small range of lift coefficients can be substantially reduced [4].

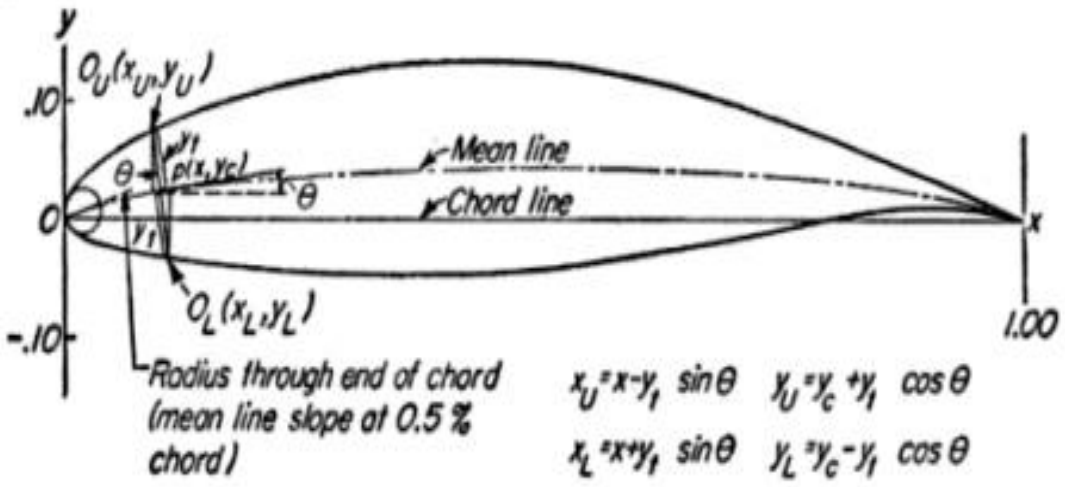

Figure 3. Mean and Chord line used for airfoil design

The naming convention of the 6-Series can easily become confusing. The airfoil used in this study is NACA 64_A-204. The codename starts with number 6 - denoting the series and indicates that this family is designed for greater laminar flow than the Four- or Five-Digit Series. The second digit, 4, is the location of the minimum pressure in tenths of chord (0.4c). The subscript A indicates that rear part of the airfoil mostly remains parallel.

The design lift coefficient (0.2) is specified by the first digit after the dash in tenths. The final two digits specify the thickness in percentage of chord, 4%. Usually there is a fraction specified by a =___ which indicates the percentage of the airfoil chord over which the pressure

distribution on the airfoil is uniform. If not specified, the quantity is assumed to be 1, or the distribution is constant over the entire airfoil. Figure 4 shows a summary of the 6-Series family of the NACA airfoils.

Family	Advantages	Disadvantages	Applications
6-Series	1. High maximum lift coefficient 2. Very low drag over a small range of operating conditions 3. Optimized for high speed	1. High drag outside of the optimum range of operating conditions 2. High pitching moment 3. Poor stall behavior 4. Very susceptible to roughness	1. Piston-powered fighters 2. Business jets 3. Jet trainers 4. Supersonic jets

Figure 4. Summary of the NACA 6 series characteristics and applciations

2.3. The supersonic airfoil linear theory

The shock-expansion theory provides a simple and general method for computing the lift and drag on a supersonic airfoil, and is applicable as long as the flow is not compressed to subsonic speeds, and the shock waves remain attached to the airfoil. However, the results of this theory cannot generally be expressed in concise analytic form. In fact, the theory is mostly used to obtain numerical solutions. However, if the airfoil is thin, and the angle of attack small, then the shocks and expansion fans attached to the airfoil become weak. In this situation, shock-expansion theory can be considerably simplified by using approximate expressions for weak shocks and expansion fans [5].

The basic approximate expression is:

$$\frac{\Delta p}{p} \cong \left(\frac{\gamma Ma^2}{\sqrt{Ma^2-1}}\right)\Delta\theta \tag{6}$$

And it specifies the relative change in pressure across either a weak oblique shock or a weak expansion fan that deflects flow of Mach number Ma through an angle $\Delta\theta$.

Because, in the weak wave approximation, the pressure, p , never greatly differs from the upstream pressure, p_1 , and the Mach number, Ma , never differs appreciably from the upstream Mach number, Ma_1 , the term can be written as:

$$\frac{p-p_1}{p_1} \cong \left(\frac{\gamma Ma^2}{\sqrt{Ma^2-1}}\right)\theta \tag{7}$$

Now, θ is the deflection angle relative to the upstream flow.

By further analyzing these equations it becomes very convenient to define a dimensionless quantity known as the *pressure coefficient:*

$$C_p = \frac{p - p_1}{q_1} \tag{8}$$

where, $q_1 = \frac{1}{2}\rho_1 w_1^2$ and $\rho_1$and $w_1$are the upstream density and flow speed, respectively.

Figure 5 shows the convention on which determining the sign of the θ angle is based on. When the surface is inclined into the freestream direction, supersonic linear theory predicts a positive θ, and thus a positive *Cp,* whereas when the surface is inclined away from the freestream direction, supersonic linear theory predicts a negative θ, and thus a negative *Cp* [2].

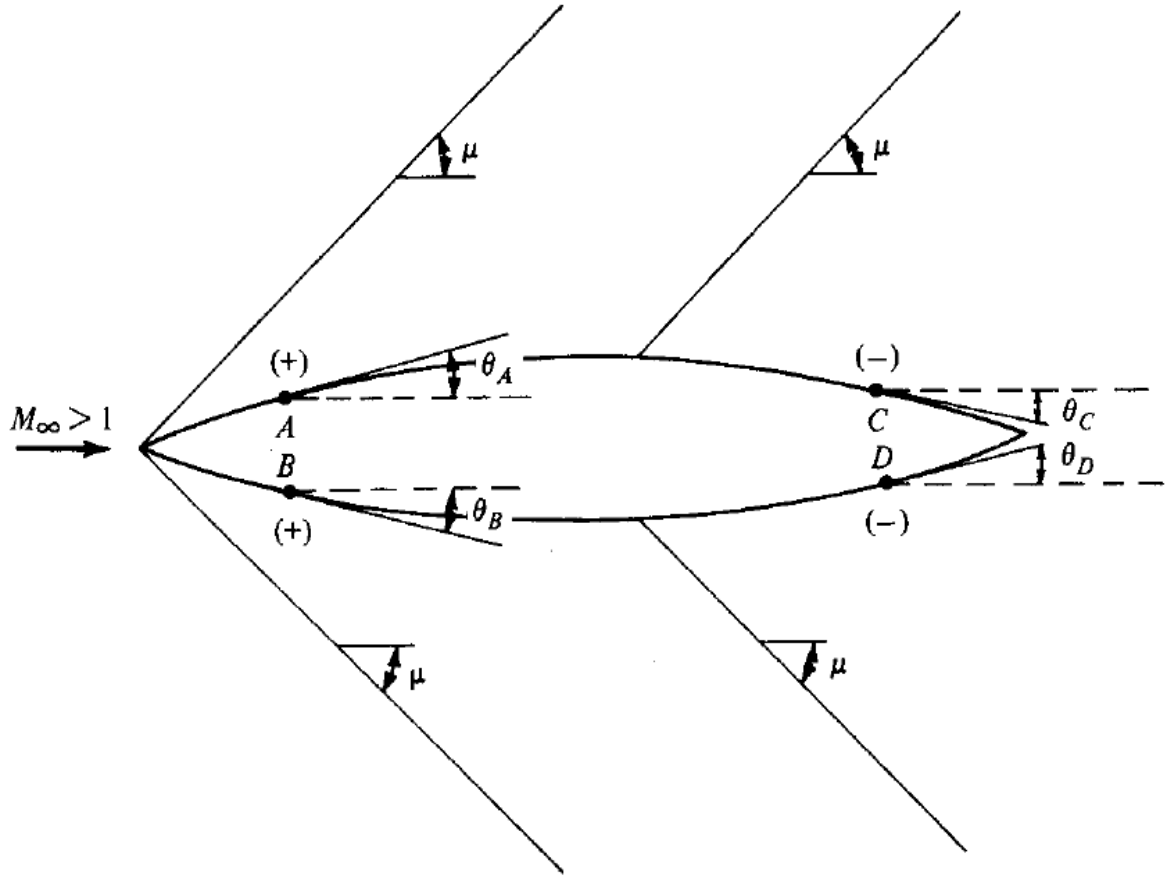

Figure 5. Linearized supersonic flow over a biconvex airfoil

Given that the upstream sound speed is $a_1 = \sqrt{\gamma \frac{p_1}{\rho_1}}$, and $Ma_1 = \frac{w_1}{a_1}$, it follows that:

$$C_p = \frac{2}{\gamma Ma_1^2}\frac{p - p_1}{p_1} \tag{9}$$

Which can finally be rearranged as:

$$C_p = \frac{2\theta}{\sqrt{Ma_1^2 - 1}} \tag{10}$$

This term (10) is the **fundamental formula** of thin-airfoil theory. It states that the pressure coefficient is proportional to the local deflection of the flow from the upstream direction.

However, in order to apply the thin airfoil theory to an arbitrary type of an airfoil additional analytical modelling is required. One such cross section of an arbitrary airfoil in the x-y plane is shown in figure 6. Z-direction will not be taken into consideration. It can be assumed that the airfoil is uniform in the z-direction. The stream flow is parallel with the **x**-axis.

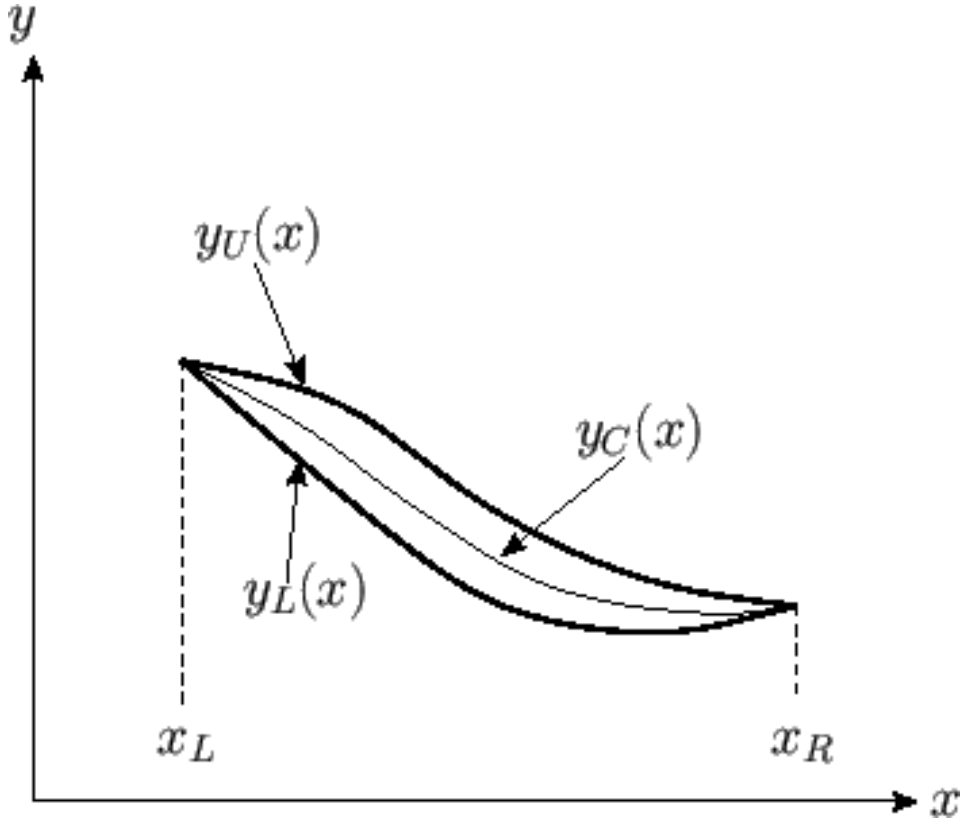

Figure 6. Arbitrary form of an airfoil

The upper surface of the airfoil corresponds to the curve $y = y_U(x)$, the lower surface to the curve $y = y_L(x)$, and the *camber line* (i.e., the centerline) to the curve $y = y_C(x)$. Furthermore, the leading and trailing edges of the airfoil lie at $x = x_L$ and $x = x_R$, respectively. Hence, $y_U(x_L) = y_C(x_L) = y_L(x_L)$ and $y_U(x_R) = y_C(x_R) = y_L(x_R)$.
From those relations it can be seen how:

$$y_c(x) = \frac{y_U(x) + y_L(x)}{2} \tag{11}$$

Stands for all the $x_L \leq x \leq x_R$. Next, it is helpful to define the airfoils *half-width:*

$$h(x) = \frac{y_U(x) - y_L(x)}{2} \tag{12}$$

Which also stand for all the $x_L \leq x \leq x_R$.
Next, it is necessary to define the *mean angle of attack* of the airfoil:

$$\alpha_0 = \frac{y_U(x_L) - y_U(x_R)}{x_R - x_L} = \frac{y_L(x_L) - y_L(x_R)}{x_R - x_L} = \frac{y_C(x_L) - y_C(x_R)}{x_R - x_L} \tag{13}$$

From that the *camber function* can be defined as:

$$y_C(x) = y_C(x_L) - \alpha_0(x - x_L) - \alpha_C(x) \tag{14}$$

Where $\alpha_C(x_L) = \alpha_C(x_R) = 0$. Here,

$$\alpha(x) = \alpha_0 + \alpha_C(x) \tag{15}$$

is the local angle of attack of the *camber-line*. Thus, the *camber function* $\alpha_C(x)$, parametrizes the deviations of $\alpha(x)$ from α_0 across the width of the airfoil.
Using the terms from (11),(12) and (14) another form of the y_U and y_L can be written:

$$y_U(x) = y_c(x) + h(x) = y_C(x_L) - \alpha_0(x - x_L) - \alpha_C(x) + h(x) \tag{16}$$
$$y_L(x) = y_c(x) - h(x) = y_C(x_L) - \alpha_0(x - x_L) - \alpha_C(x) + h(x) \tag{17}$$

Taking all the above terms into consideration pressure coefficients for the upper and lower surfaces can be expressed as:

$$C_{pU} = \frac{2}{\sqrt{Ma^2 - 1}} \frac{dy_U}{dx} \tag{18}$$

$$C_{pL} = \frac{2}{\sqrt{Ma^2 - 1}} \left(\frac{-dy_L}{dx} \right) \tag{19}$$

Furthermore, using the terms (15),(16) and (17) it follows that

$$\frac{dy_U}{dx} = -\alpha(x) + \frac{dh}{dx} \tag{20}$$

$$\frac{dy_L}{dx} = -\alpha(x) - \frac{dh}{dx} \tag{21}$$

Now, using the derived terms for pressure coefficients the lift and drag forces per unit transverse length acting on the airfoil can be given by:

$$L = q_1 \int_{x_L}^{x_R} (C_{pL} - C_{pU}) dx \tag{22}$$

$$D = q_1 \int_{x_L}^{x_R} \left[C_{pL} \left(\frac{-dy_L}{dx} \right) + C_{pU} \left(\frac{dy_U}{dy} \right) \right] dx \tag{23}$$

By implementing terms (18) - (21) into (22) and (23) it follows:

$$D = \frac{4q_1}{\sqrt{Ma^2 - 1}} \int_{x_L}^{x_R} \alpha(x) dx \tag{24}$$

$$L = \frac{4q_1}{\sqrt{Ma^2 - 1}} \int_{x_L}^{x_R} \left[\left(\frac{dh}{dx} \right)^2 + \alpha^2 \right] dx \tag{25}$$

It is now helpful to define the chord-average operator:

$$\bar{y} \equiv \frac{1}{c} \int_{x_L}^{x_R} y(x) dx \tag{26}$$

Where $c = x_R - x_L$ is the chord-length. Taking the average of equation (20), making use of (13), as well as the fact that $h(x_L) = h(x_R) = 0$ the following relation is obtained:

$$\bar{\alpha} = \alpha_0 \tag{27}$$

However, the average of the equation (15) yields:

$$\bar{\alpha} = \alpha_0 + \overline{\alpha_C} \tag{28}$$

Which implies that $\overline{\alpha_C} = 0$. It can also be written as:

$$\overline{\alpha^2} = \overline{(\alpha_0 + \alpha_C)^2} = \overline{\alpha_0^2} + 2\overline{\alpha_0 \alpha_C} + \overline{\alpha_C^2} \tag{29}$$

Combining most of the terms defined on the previous pages, the coefficients of lift and drag, $L/(q_1 c)$ and $D/(q_1 c)$, are written as :

$$C_L = \frac{4\bar{\alpha}}{\sqrt{Ma^2 - 1}} = \frac{4\alpha_0}{\sqrt{Ma^2 - 1}} \tag{30}$$

$$C_D = \frac{4}{\sqrt{Ma^2 - 1}} \left[\overline{\left(\frac{dh}{dx} \right)^2} + \overline{\alpha^2} \right] = \frac{4}{\sqrt{Ma^2 - 1}} \left[\overline{\left(\frac{dh}{dx} \right)^2} + {\alpha_0}^2 + \overline{\alpha_C^2} \right] \tag{31}$$

respectively. Thus, in thin-airfoil theory, the lift only depends on the mean angle of attack, whereas the drag splits into three components. Namely, a drag due to thickness, a drag due to lift, and a drag due to camber.

An interesting point worth noting about the cambered airfoil and cambered wings in supersonic flight regime is the prediction of the lift coefficient at zero degrees angle of attack. The prediction is given by the supersonic airfoil theory of the second order [6]. Because first and second order supersonic airfoil theory is relatively simple analytically, numerous studies finding optimum aerodynamic characteristics have been made. They will not be covered here, but rather refer to an entire book that covers the subject at [7].

Looking at the literature, almost all data used for comparison with airfoils comes from the wind tunnel tests conducted by Antonio Ferri at Guidonia in Italy [8]. To answer how well the supersonic linear theory agrees with data, refer to figure 7.

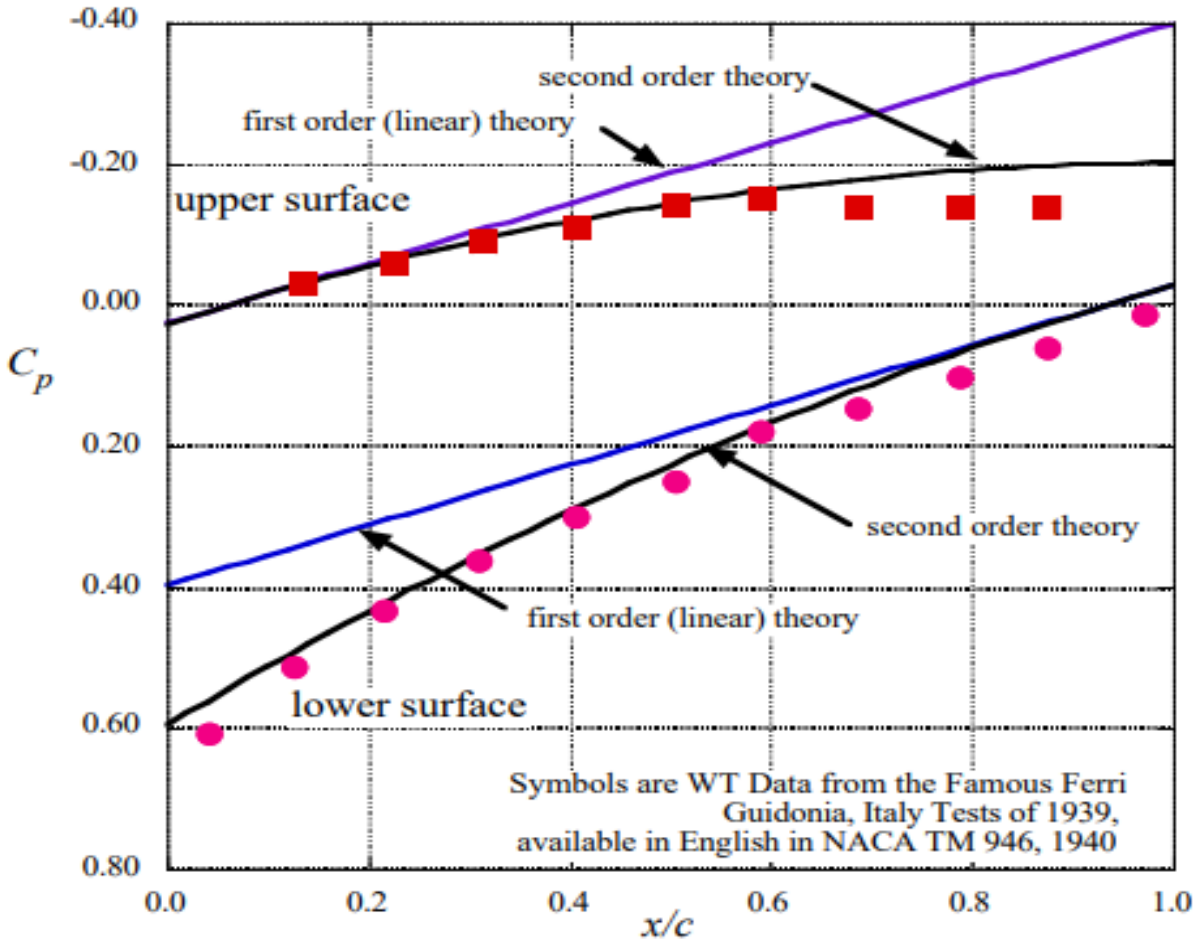

Figure 7. Supersonic airfoil pressure distribution comparison 10% thick biconvex airfoil at α=10°, M=2.13

First order linear theory only considers the leading and trailing edge values, camber and thickness don't affect lift. This is not true for second order supersonic airfoil theory [6]. For a flat lower surface and a curved upper surface, generally considered positive camber, the lift at zero angle of attack is negative. Figure 8. shows this effect for one of the airfoils tested by Ferri. This case is for a one-sided wedge 6.3% thick. Although not a huge effect, it is noticeable.

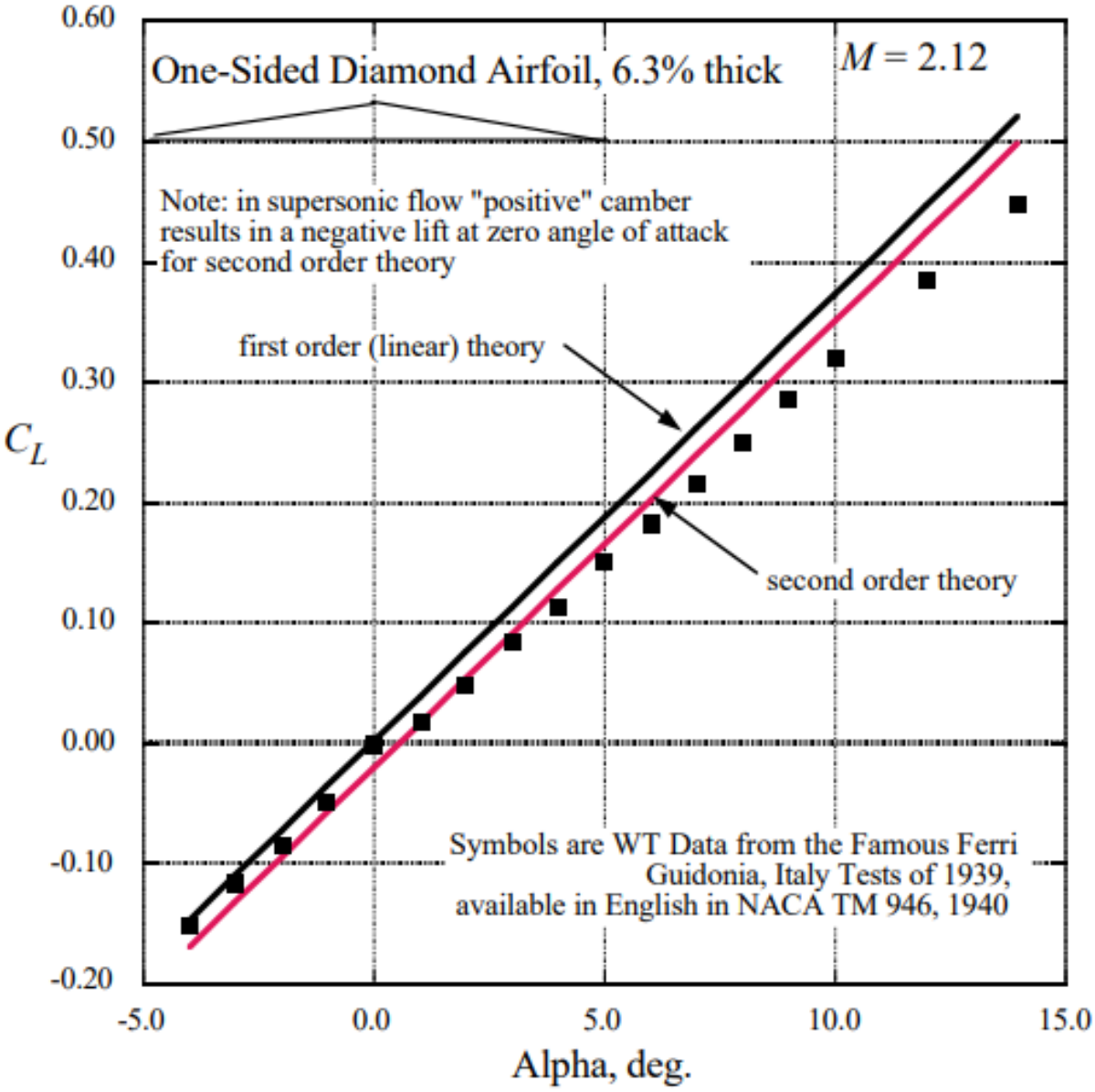

Figure 8. Second order linear theory lift prediction

3. Linearized supersonic theory - NACA 64_A-204 application

Supersonic airfoil theory is particularly interesting in that it explains the F-16 device deflection schedule. At supersonic speed the F-16 automatic device schedule includes leading and trailing edges with a negative deflection, as shown in Figure 9. – the fourth configuration (supersonic cruise). The F-16 has a NACA 64_A-204 airfoil, and the leading and trailing edges use an automatic -2 degree deflection at supersonic speeds in order to mitigate the negative lift.

Although the flaps are continuously variable, the five basic positions are shown in Figure 9. For takeoff and landing, the TEF is commanded to the full-down (20 deg) position by the landing gear handle, and the LEF is scheduled as a function of Mach number, AOA, and weight on wheels. For subsonic cruise, the basic wing camber is unmodified. During subsonic maneuvering the LEF is commanded to deflect downward as AOA increases (high 'g' maneuvering). For supersonic flight the wing is decambered as shown in the lower left-hand corner of Figure 9.

Leading edge flap is automatically programmed for best flap position (max lift/drag as a function of Mach number and angle of attack). Variable camber shapes airfoil to match desired flight condition in order to maximize lift/drag ratio, improve directional stability and minimize buffet.

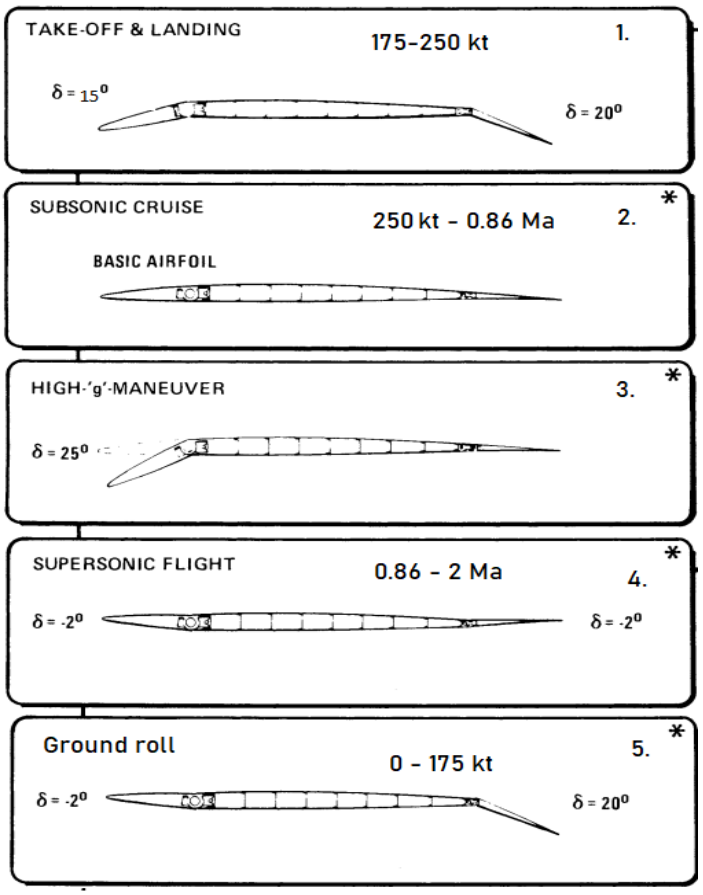

Figure 9. Automatic variable camber of the NACA 64_A-204 airfoil used by F-16

Table 1. Flaps deflection angles for different flight phases

Flight phase	Velocity/ Mach number	Leading edge flap angle	Trailing edge flap angle
Ground roll	0-175 kts [IAS]	-2°	20°
Take-off and landing	175-250 kts [IAS]	15°	20°
Subsonic cruise	0.86 Ma [TAS]	0°	0°
Supersonic cruise	0.86-2 Ma [TAS]	-2°	-2°

The F-16 aircraft is equipped with a single Pratt&Whitney F100_PW_229 turbo fan engine. It has the option of turning on the engines afterburner for short durations in order to enhance its thrust. Since the afterburner consumes lots of fuel, it is switched off at subsonic speeds. Regular thrust is enough for achieving velocities of about 0.86 Mach at 35000 ft, which is the optimal speed and altitude for subsonic cruise. The flight ceiling at the subsonic cruise is around 50000 ft.

However, the F-16 was designed in order to perform quick dashes at supersonic speeds in order to infiltrate the enemy territory, deliver its load and safely come back. While performing such maneuvers the afterburner is turned on and it delivers massive increase in thrust which allows the airplane to fly at speeds up to 2 Mach and at altitudes up to 60000 ft. The performance comparison for flight with no afterburner and with full afterburner are presented in figure 10.

The F-16 does not have the ability to cruise at supersonic speeds. The afterburner is very demanding on the fuel consumption. The aircraft spends most of its flight time at subsonic speeds, and only when necessary uses the afterburner to achieve its maximum speed and altitude.

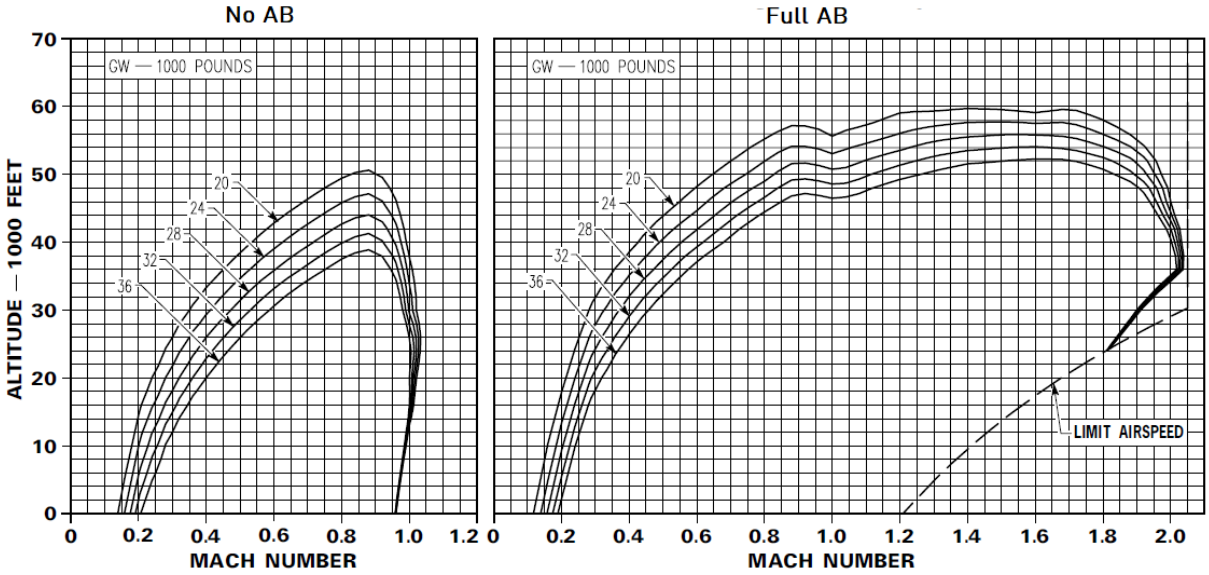

Figure 10. No AB vs Full AB performance

A standard deployment mission is presented in figure 11. It shows the trajectory of the airplane along with the standard performances. The F-16 can equip enough fuel tanks to sustain flight ranges of up to 2000 NM. The performance numbers, altitude and speeds, are given in table 1.

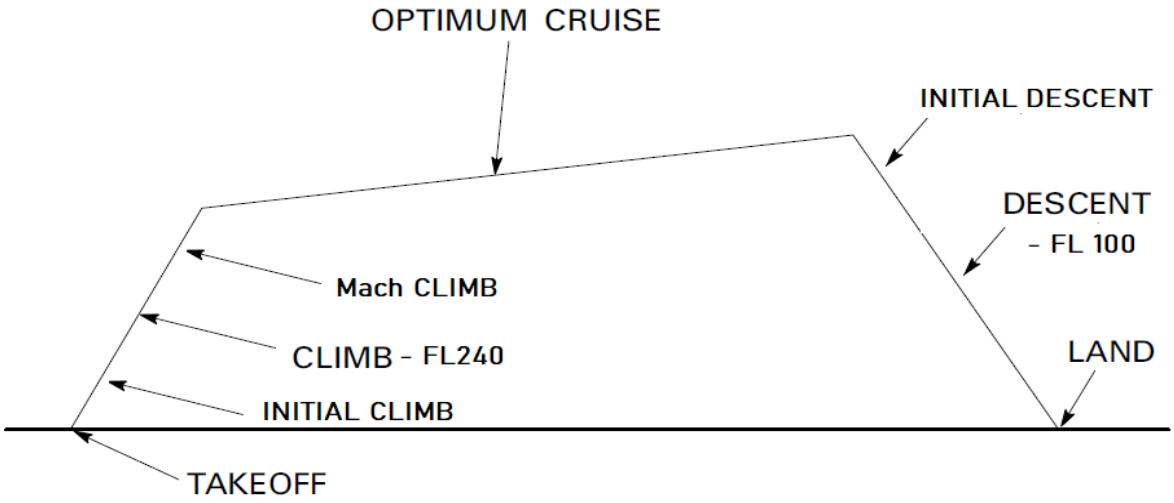

Figure 11. F-16 deployment mission

There are various types of missions that F-16 is designed to perform. The one shown on figure 11. is only a basic deployment mission shown in order to provide visual representation at which velocity does it fly with which wing configuration. Table 2, shown below, presents the changes in leading and trailing edge flaps, along with the position of the landing gear depending on the segment of the flight.

Table 2. F-16 performance data

Take-off	160 kts	LEF: -2°	TEF: 20°	LG: ↓
Initial climb (up to 5k ft)	175 kts	LEF: 15°	TEF: 20°	LG: ↑
Climb to FL 240	300 kts	LEF: 0°	TEF: 0°	LG: ↑
Mach climb to cruise height	0.8 Mach	LEF: 0°	TEF: 0°	LG: ↑
Cruise (ceiling at 50k ft)	0.86 Mach	LEF: 0/-2°	TEF: 0/-2°	LG: ↑
Initial descent to FL 240	0.85 Mach	LEF: 0°	TEF: 0°	LG: ↑
Descent to FL 100	350 kts	LEF: 0°	TEF: 0°	LG: ↑
Approach	250 kts	LEF: 15°	TEF: 20°	LG: ↓
Landing	150 kts	LEF: -2°	TEF: 20°	LG:↓

For all the analytical computations, MATLAB 2018a was used. Firstly, the coordinate file was downloaded from the airfoil tools plotter web-page, which can be found at [9]. Figure 12. shows the coordinate points plotted inside MATLAB.

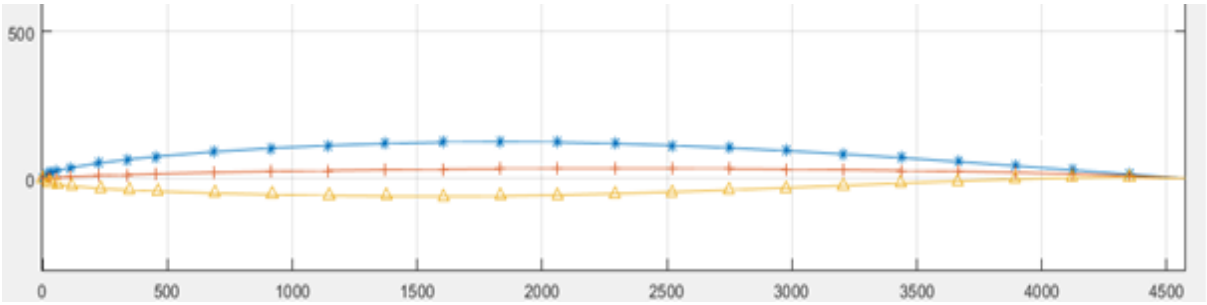

Figure 12. Original NACA 64A-204 airfoil coordinate dataset

Then, since the amount of coordinate points was limited to 25 points, MATLAB was used to expand the number to over 200 points per surface. This was done by numerical interpolation between the original points.

Furthermore, all three surfaces were then split into 3 different parts. The leading and trailing parts had to be made as movable, while the center part was kept in place. In order to proceed with the analysis of variable geometry a rotation matrix had to be employed as part of a function which controlled the shape of an airfoil.

$$\begin{bmatrix} x' \\ y' \end{bmatrix} = \begin{bmatrix} cos\ \theta & -\sin\theta \\ sin\ \theta & cos\ \theta \end{bmatrix} \begin{bmatrix} x \\ y \end{bmatrix} \tag{32}$$

Expression (32) shows the tool used for rotating the leading and trailing parts of the airfoil around a specified x-y point. By plugging in a number which represents the degree value of the deflection into θ, and then by multiplying the vector array with the prepared matrix (32) rotation was obtained.

A function named *Curvature_change* was defined as a function that takes up to three arguments – configuration number, Mach number, and the third argument is optional since it is only used for plotting the airfoil which will be returned by the function. The values that the function returns are: change in slopes for camber, upper and lower surfaces, $\frac{dh}{dx}$ and coordinates of a newly formed – deflected airfoil. Figure 13. Presents various configurations plotted by MATLAB.

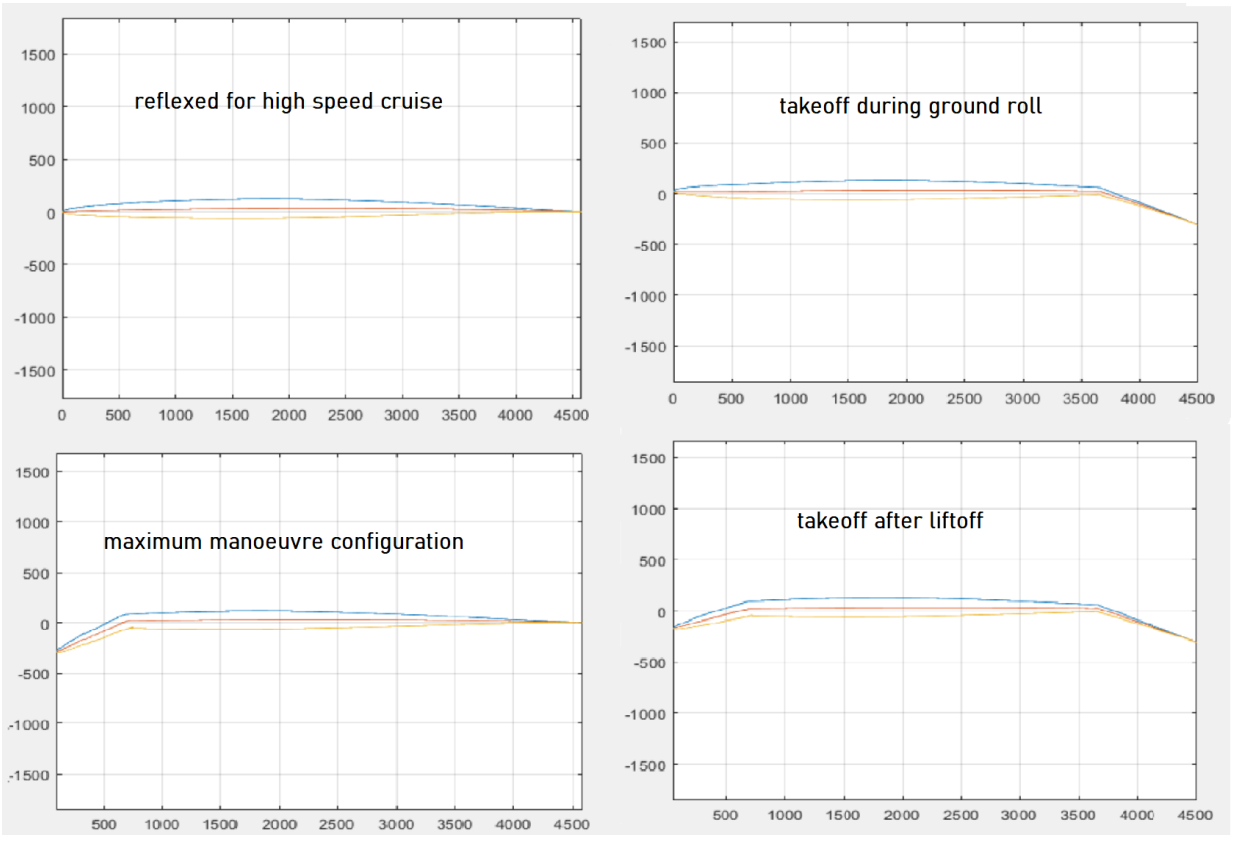

Figure 13. NACA 64A-204 airfoil configurations used by F-16

Function offers additional arguments to be returned, arguments such as C_{pU} and C_{pL}. By plotting these values throughtout the length of the airfoil chord very convenient figures were obtained. Figures which complied with the predictions of linear theory for changes in pressure coefficients based on the changes in the airfoil surfaces. Those figures, along with other results will be shown in the third chapter – application of the theory.

Another script was created called *Graph_draw* and it was used for plotting and calculation of lift and drag coefficients. Inside the script, Mach number was defined, along with the range of AoA for over which the calculations would be made. The calculations were conducted using the terms (30) and (31) derived in the previous chapter.

Curvature_change

```
function [dhdx,nagib_camber,nagib_gornjaka,nagib_donjaka,Cpu,Cpl,x_donjaka_sto_dvjesto,...
y_donjaka_sto_dvjesto,x_gornjaka_sto_dvjesto,y_gornjaka_sto_dvjesto]=curvature_change(pozicija,Ma,cr
tanje)
```

```
Get_coordinates; %a script used for defining numerous data points that define the surfaces of the
airofil, divides the original coordinate vector into 3 sections

%Depending on the first argument given to the function, the "position argument", var "a", takes the
values of the amount of degrees the leading and trailing edge are going to deform

if pozicija == 1
    a(1)=-2;
    a(2)=-20;
elseif pozicija == 2
    a(1)=15;
    a(2)=-20;
elseif pozicija == 3
    a(1)=-2;
    a(2)=2;
elseif pozicija == 4
    a(1)=25;
    a(2)=0;
elseif pozicija == 0
    a(1)=0;
    a(2)=0;
else

    error('try again with numbers 0-4.');
end
```

```
%setting 2 vector arrays into single matrix in a proper order
mlef_gornjaka=[xlef_gornjaka';ylef_gornjaka'];
mlef_srednjaka=[xlef_srednjaka';ylef_srednjaka'];
mlef_donjaka=[xlef_donjaka';ylef_donjaka'];

centar_gornjaka=[mlef_gornjaka(:,end)];
centar_srednjaka=[mlef_srednjaka(:,end)];
centar_donjaka=[mlef_donjaka(:,end)];

m2lef_gornjaka=mlef_gornjaka-centar_gornjaka;
m2lef_srednjaka=mlef_srednjaka-centar_gornjaka;
m2lef_donjaka=mlef_donjaka-centar_gornjaka;

% Applying the rotation matrix to newly formed leading edge matrices containing coordinate points in
order to rotate them around a focal point based on the cartesian coordinate system

z=[cos(deg2rad(a(1))) -sin(deg2rad(a(1)));sin(deg2rad(a(1))),cos(deg2rad(a(1)))];
```

```
rotacija_lef_gornjaka= z*m2lef_gornjaka+centar_gornjaka;
rotacija_lef_srednjaka= z*m2lef_srednjaka+centar_gornjaka;
rotacija_lef_donjaka = z*m2lef_donjaka+centar_gornjaka;

xlef_gornjaka_rotiran = rotacija_lef_gornjaka(1,:);
ylef_gornjaka_rotiran = rotacija_lef_gornjaka(2,:);
xlef_srednjaka_rotiran=rotacija_lef_srednjaka(1,:);
ylef_srednjaka_rotiran=rotacija_lef_srednjaka(2,:);
xlef_donjaka_rotiran=rotacija_lef_donjaka(1,:);
ylef_donjaka_rotiran=rotacija_lef_donjaka(2,:);
```

```
mtef_gornjaka=[xtef_gornjaka';ytef_gornjaka'];
mtef_srednjaka=[xtef_srednjaka';ytef_srednjaka'];
mtef_donjaka=[xtef_donjaka';ytef_donjaka'];

centar_gornjaka=[mtef_gornjaka(:,1)];
centar_srednjaka=[mtef_srednjaka(:,1)];
centar_donjaka=[mtef_donjaka(:,1)];

m2tef_gornjaka=mtef_gornjaka-centar_gornjaka;
m2tef_srednjaka=mtef_srednjaka-centar_gornjaka;
m2tef_donjaka=mtef_donjaka-centar_gornjaka;

%trailing edge rotation

z=[cosd(a(2)) -sind(a(2));sind(a(2)),cosd(a(2))];
rotacija_tef_gornjaka= z*m2tef_gornjaka+centar_gornjaka;
rotacija_tef_srednjaka= z*m2tef_srednjaka+centar_gornjaka;
rotacija_tef_donjaka = z*m2tef_donjaka+centar_gornjaka;

xtef_gornjaka_rotiran = rotacija_tef_gornjaka(1,:);
ytef_gornjaka_rotiran = rotacija_tef_gornjaka(2,:);
xtef_srednjaka_rotiran=rotacija_tef_srednjaka(1,:);
ytef_srednjaka_rotiran=rotacija_tef_srednjaka(2,:);
xtef_donjaka_rotiran=rotacija_tef_donjaka(1,:);
ytef_donjaka_rotiran=rotacija_tef_donjaka(2,:);
```

```
x_gornjaka_sto_dvjesto=[xlef_gornjaka_rotiran,xsredina_gornjaka',xtef_gornjaka_rotiran];
y_gornjaka_sto_dvjesto=[ylef_gornjaka_rotiran,ysredina_gornjaka',ytef_gornjaka_rotiran];

x_camber_sto_dvjesto = [xlef_srednjaka_rotiran,xsredina_srednjaka',xtef_srednjaka_rotiran];
y_camber_sto_dvjesto = [ylef_srednjaka_rotiran,ysredina_srednjaka',ytef_srednjaka_rotiran];

x_donjaka_sto_dvjesto = [xlef_donjaka_rotiran,xsredina_donjaka',xtef_donjaka_rotiran];
y_donjaka_sto_dvjesto = [ylef_donjaka_rotiran,ysredina_donjaka',ytef_donjaka_rotiran];
```

```
if nargin > 2 && crtanje ==1
    figure;
plot(x_gornjaka_sto_dvjesto,y_gornjaka_sto_dvjesto,x_camber_sto_dvjesto,y_camber_sto_dvjesto,x_donja
ka_sto_dvjesto,y_donjaka_sto_dvjesto)
hold on, axis equal, grid on;
end
```

```
for i = 1 : length(y_gornjaka_sto_dvjesto)
    h(i)=(y_gornjaka_sto_dvjesto(i)-y_donjaka_sto_dvjesto(i))/2 ;
end
```

```
for i = 1 : length(x_gornjaka_sto_dvjesto)-1
dhdx(i)=(h(i+1)-h(i))/(x_gornjaka_sto_dvjesto(i+1)-x_gornjaka_sto_dvjesto(i));

end
dhdx(end)=dhdx(end-1);
```

```
for i = 1 : length(x_gornjaka_sto_dvjesto)-1

    nagib_gornjaka(i)=((y_gornjaka_sto_dvjesto(i+1)-
y_gornjaka_sto_dvjesto(i))/(x_gornjaka_sto_dvjesto(i+1)-x_gornjaka_sto_dvjesto(i)));
    nagib_camber(i)=(y_camber_sto_dvjesto(i+1)-y_camber_sto_dvjesto(i))/(x_camber_sto_dvjesto(i+1)-
x_camber_sto_dvjesto(i));
    nagib_donjaka(i)=-1*((y_donjaka_sto_dvjesto(i+1)-
y_donjaka_sto_dvjesto(i))/(x_donjaka_sto_dvjesto(i+1)-x_donjaka_sto_dvjesto(i)));
end
nagib_gornjaka(end+1)=nagib_gornjaka(end);
nagib_donjaka(end+1)=nagib_donjaka(end);
```

```
figure;
if nargin >=2
    Cpu = (2.*(nagib_gornjaka))./sqrt((Ma^2)-1);
Cpl = (2.*(nagib_donjaka)) ./sqrt((Ma^2)-1);
indx=find(Cpl<-1.5);
Cpl(indx)=Cpl(indx-1);  %Necessary to fix the sudden and false increase of value caused by the 2
points at the hinge
nagib_gornjaka(end+1)=nagib_gornjaka(end);
nagib_donjaka(end+1)=nagib_donjaka(end);
% plots the pressure coefficient throughout the length of the airfoil (used for ansys comparison!)
plot(x_gornjaka_sto_dvjesto,Cpu,'r-'), grid on, hold on;
plot(x_gornjaka_sto_dvjesto,Cpl,'b-'), legend("Cp-top","Cp-bottom"), xlabel('Position
[cm]'),ylabel('Cp');

end
% used for calculating the slope of the airfoil chord in order to control the correct angle of
attack of the free stream!
a=[x_gornjaka_sto_dvjesto(1),y_gornjaka_sto_dvjesto(1)];
b=[x_gornjaka_sto_dvjesto(end),y_gornjaka_sto_dvjesto(end)];
slope=(b(2)-a(2))/(b(1)-a(1));
kut_nagiba = rad2deg(atan(slope));
```

```
end
```

Ggraph_draw

```
%%Script used for drawing various graphs, such as the airfoil polar, drag
%%distribution, lift distribution. Changes are made by varying the mach number
%%and by varying the angle of attack
```

```
napadni_kut=0:12;  %Angle of Attack
Ma = 1.5;
```

```
for i = 0:4

    [dhdx,nagib_camber,nagib_gornjaka,nagib_donjaka,Cpu,Cpl,x_donjaka_sto_dvjesto,...
        y_donjaka_sto_dvjesto,x_gornjaka_sto_dvjesto,y_gornjaka_sto_dvjesto]=curvature_change(i,Ma);
    Cl = 4.*deg2rad(napadni_kut)./sqrt(Ma.^2-1);
    Cd = 4.*(deg2rad(napadni_kut).^2+mean(dhdx)^2+mean(nagib_camber)^2)./sqrt(Ma.^2-1);
    plot(Cd,Cl,'^-'),hold on, grid on,title(sprintf('Cl v Cd @ Ma = %2.2f',Ma)),
xlabel('Cd'),ylabel('Cl');
    legend('starting position','takeoff during ground roll','takeoff after lift off','reflexed for
high speed cruiuse','maximum manoeuvre configuration')

end
```

By employing the terms discussed in the second chapter under the supersonic airfoil theory, MATLAB was used to calculate the polar graphs for all the airfoil configurations. Flow velocity was set at Ma = 1.5, and angle of attack ranges from -24 to 24 degrees. That range was selected for AoA in order to demonstrate how symmetric are the results obtained by linear theory. Results can be seen on the figure below:

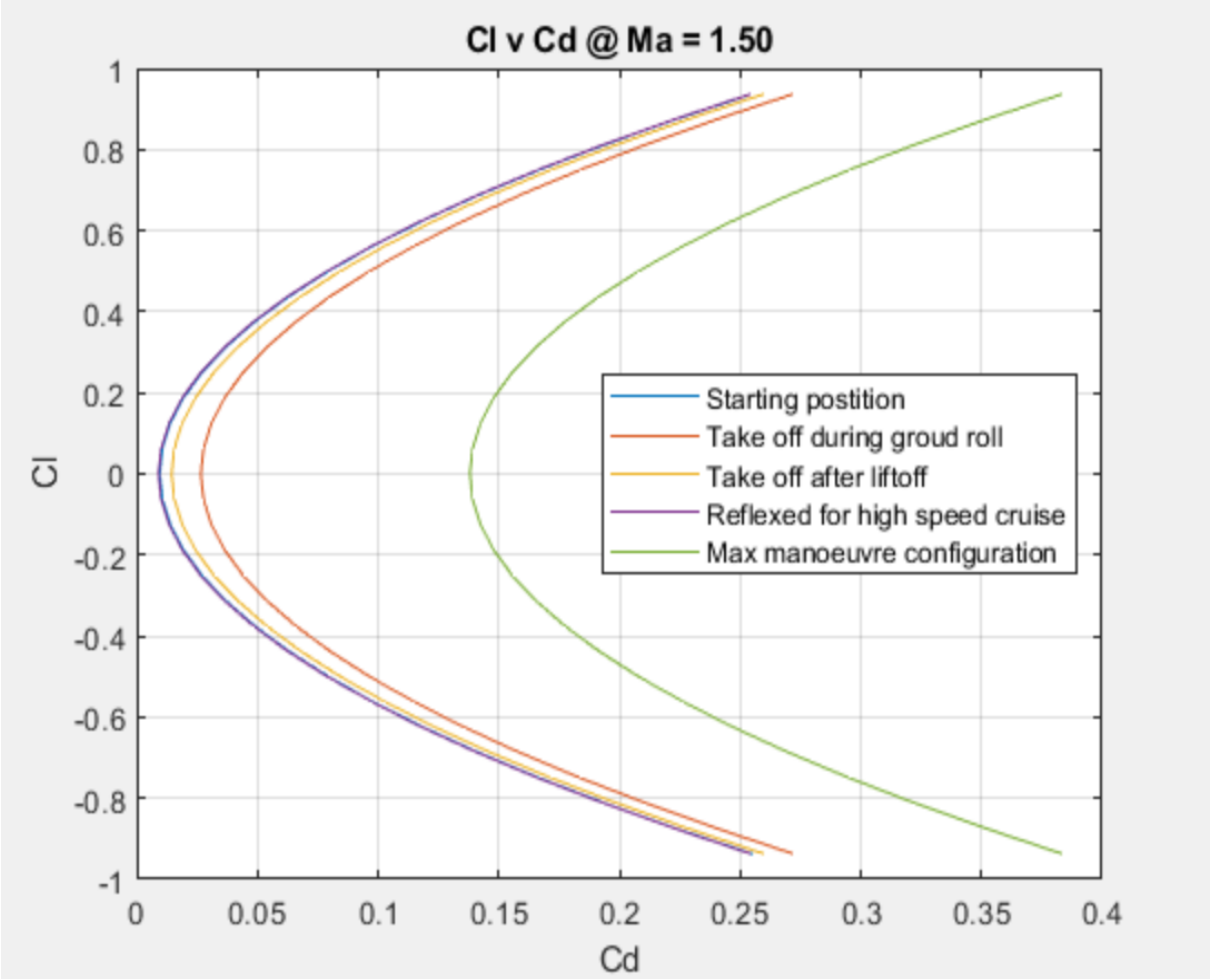

Figure 14. Supersonic airfoil linear theory results for Ma=1.5, AoA=-24:24

Only the starting position along with the reflexed for high speed cruise are of true importance, because the linear theory holds true only for airfoils with no diverse stream deflections. It can be seen how they align almost perfectly. All other configurations are never employed during such high speed regimes. The supersonic airfoil linear theory cannot really predict true behavior of lift and drag for configurations that have larger changes in their geometry and diverse gradient changes that come along.

Figure 15. shows comparison of the subsonic and supersonic configurations. Mach value is set at Ma=1.5, whereas the angle of attack now ranges from 0 to 12°.

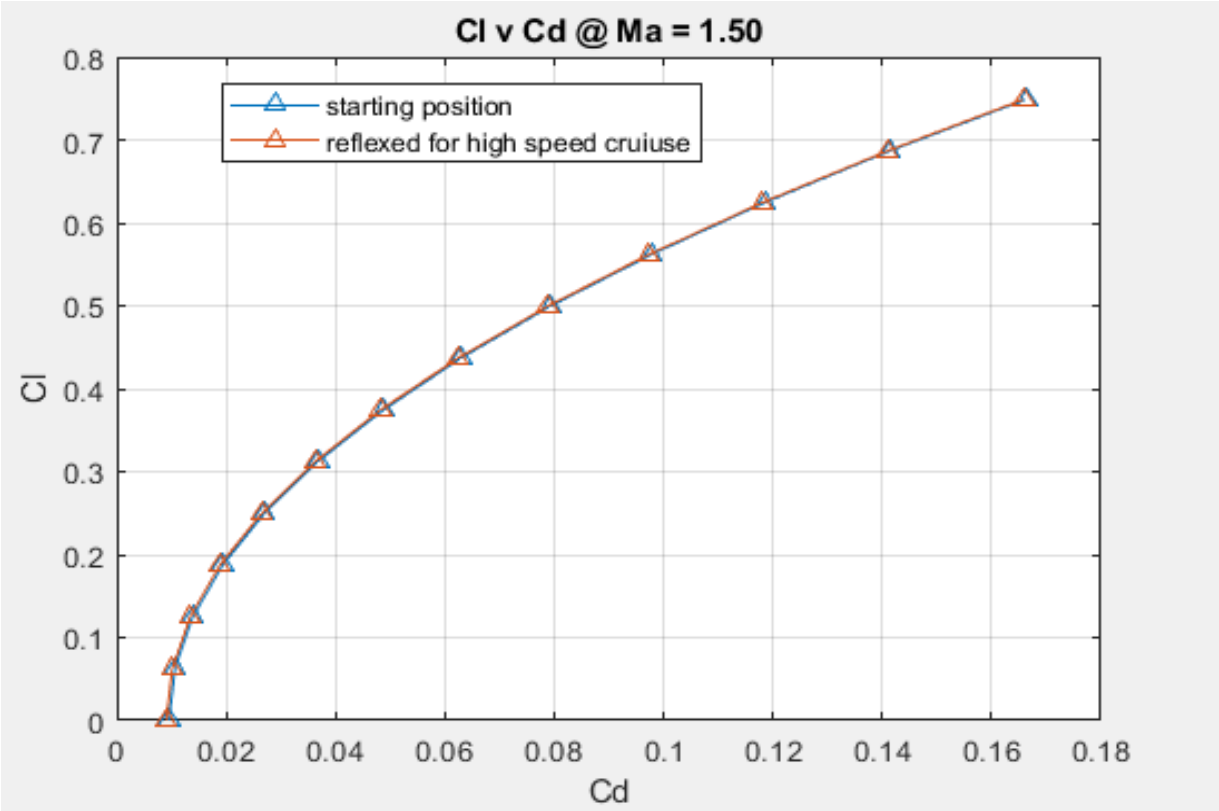

Figure 15. Subsonic and supersonic cruise configuration comparison for Ma=1.5, AoA=0:12

As expected, since the theory bases the lift coefficient solely on the angle of attack, both configurations have equal values. The only thing differing them is the drag coefficient, and since the difference in the airfoil shape is minimal – the difference in drag values is also minimal.

Table 3. Subsonic and Supersonic configuration comparison, Ma=1.5

Angle of Attack	Subsonic configuration		Supersonic configuration	
	Cl	Cd	Cl	Cd
0°	0	0.0097	0	0.0092
1°	0.0624	0.0108	0.0624	0.0103
2°	0.1249	0.0141	0.1249	0.0135
3°	0.1873	0.0195	0.1873	0.0190
4°	0.2498	0.0271	0.2498	0.0266
5°	0.3122	0.0369	0.3122	0.0364
6°	0.3747	0.0489	0.3747	0.0484
7°	0.4371	0.0631	0.4371	0.0626
8°	0.4995	0.0794	0.4995	0.0789
9°	0.5620	0.0980	0.5620	0.0974
10°	0.6244	0.1187	0.6244	0.1181
11°	0.6869	0.1416	0.6869	0.1410
12°	0.7493	0.1666	0.7493	0.1661

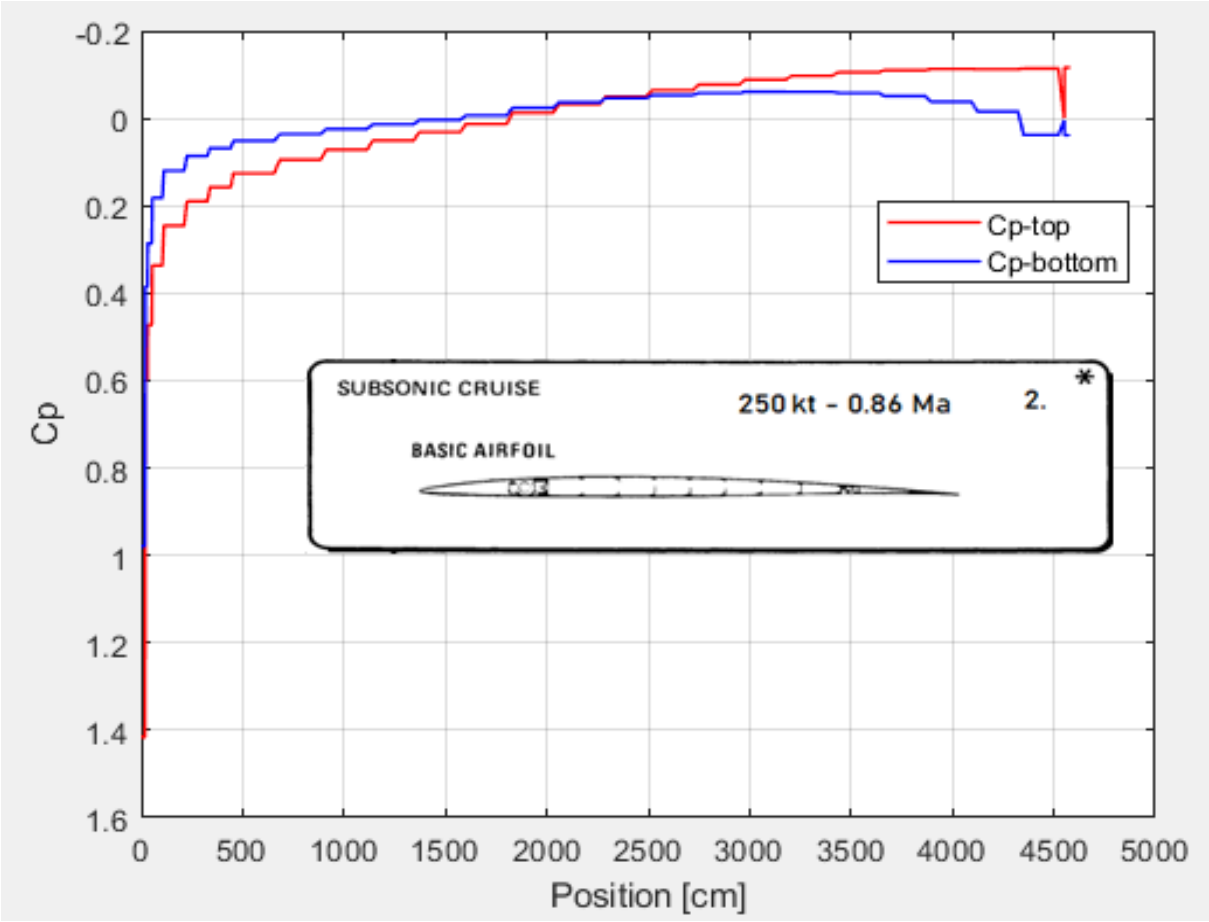

Figure 16. Linear theory Cp distribution – subsonic cruise configuration

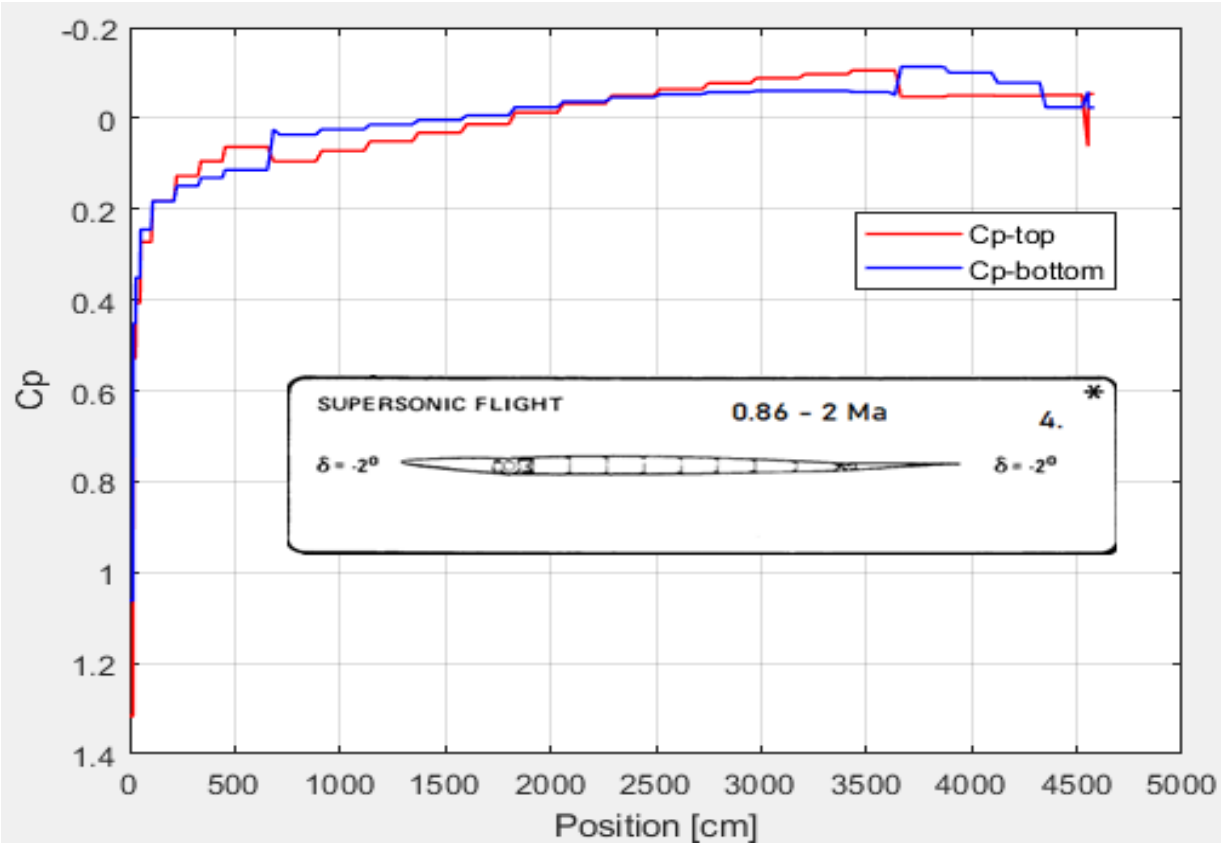

Figure 17. Linear theory Cp distribution – reflexed for high speed cruise configuration

Figure 16. shows the pressure coefficient distribution along the upper and lower surfaces of the airfoil for the subsonic (basic) cruise configuration. Prediction is based on the supersonic airfoil linear theory.

The difference between lines in the above figure is what generates aerodynamical forces such as lift and drag. It can be observed how there is a change in behavior at around 0.4c which is the point of the greatest thickness.

Figure 17 shows the pressure coefficient distribution along the upper and lower surfaces of the airfoil for the supersonic configuration. It is somewhat different than the subsonic cruise configuration distribution, however there are similarities.

Only minor differences are visible for the pressure distribution – only minor differences exist in the above configurations.

4. Basic principles of Computational Fluid Dynamics

Computational fluid dynamics (CFD) is a branch of fluid dynamics that uses numerical analysis and data structures to analyze and solve problems that involve fluid flows. Computers are used to perform the calculations required to simulate the free-stream flow of the fluid, and the interaction of the fluid with surfaces defined by boundary conditions. With high-speed supercomputers, better solutions can be achieved, and are often required to solve the largest and most complex problems. Ongoing research yields software that improves the accuracy and speed of complex simulation scenarios such as transonic or turbulent flows. Initial validation of such software is typically performed using experimental apparatus such as wind tunnels. In addition, previously performed analytical or empirical analysis of a particular problem can be used for comparison. A final validation is often performed using full-scale testing, such as flight tests.

CFD is applied to a wide range of research and engineering problems in many fields of study and industries, including aerodynamics and aerospace analysis, weather simulation, natural science and environmental engineering, industrial system design and analysis, biological engineering, fluid flows and heat transfer, and engine and combustion analysis.

4.1. Brief history of CFD

The fundamental basis of almost all CFD problems are the Navier–Stokes equations, which define many single-phase (gas or liquid, but not both) fluid flows. These equations can be simplified by removing terms describing viscous actions to yield the Euler equations. Further simplification, by removing terms describing vorticity yields the full potential equations. Finally, for small perturbations in subsonic and supersonic flows (not transonic or hypersonic) these equations can be linearized to yield the linearized potential equations.

Historically, methods were first developed to solve the linearized potential equations. Two-dimensional (2D) methods, using conformal transformations of the flow about a cylinder to the flow about an airfoil were developed in the 1930s [10].

One of the earliest type of calculations resembling modern CFD are those by Lewis Fry Richardson, in the sense that these calculations used finite differences and divided the physical space in cells. Although they failed dramatically, these calculations, together with Richardson's book "Weather prediction by numerical process", [11], set the basis for modern CFD and numerical meteorology. In fact, early CFD calculations during the 1940s using ENIAC used methods close to those in Richardson's 1922 book [12].

History can briefly be summarized in a following manner:

- **Until 1910:** Improvements on mathematical models and numerical methods.
- **1910 – 1940:** Integration of models and methods to generate numerical solutions based on hand calculations.

- **1940 – 1950:** Transition to computer-based calculations with early computers (ENIAC). Solution for flow around a cylinder by Kawaguti et al. with a mechanical desk calculator in 1953.
- **1950 – 1960:** Initial study using computers to model fluid flow based on the Navier-Stokes equations by Los Alamos National Lab, US. Evaluation of vorticity – stream function method. First implementation for 2D, transient, incompressible flow in the world.
- **1960 – 1970:** First scientific paper "Calculation of potential flow about arbitrary bodies" was published about computational analysis of 3D bodies by Hess and Smith in 1967 [13]. Generation of commercial codes. Contribution of various methods such as k-ε turbulence model, Arbitrary Lagrangian-Eulerian, SIMPLE algorithm which are all still broadly used.
- **1970 – 1980:** Codes generated by Boeing, NASA and others have unveiled and started to use several yields such as submarines, surface ships, automobiles, helicopters and aircrafts.
- **1980 – 1990:** Improvement of accurate solutions of transonic flows in the three-dimensional case by Jameson et. al. Commercial codes have started to implement through both academia and industry.
- **1990 – Present:** Thorough developments in Informatics: worldwide usage of CFD virtually in every sector.

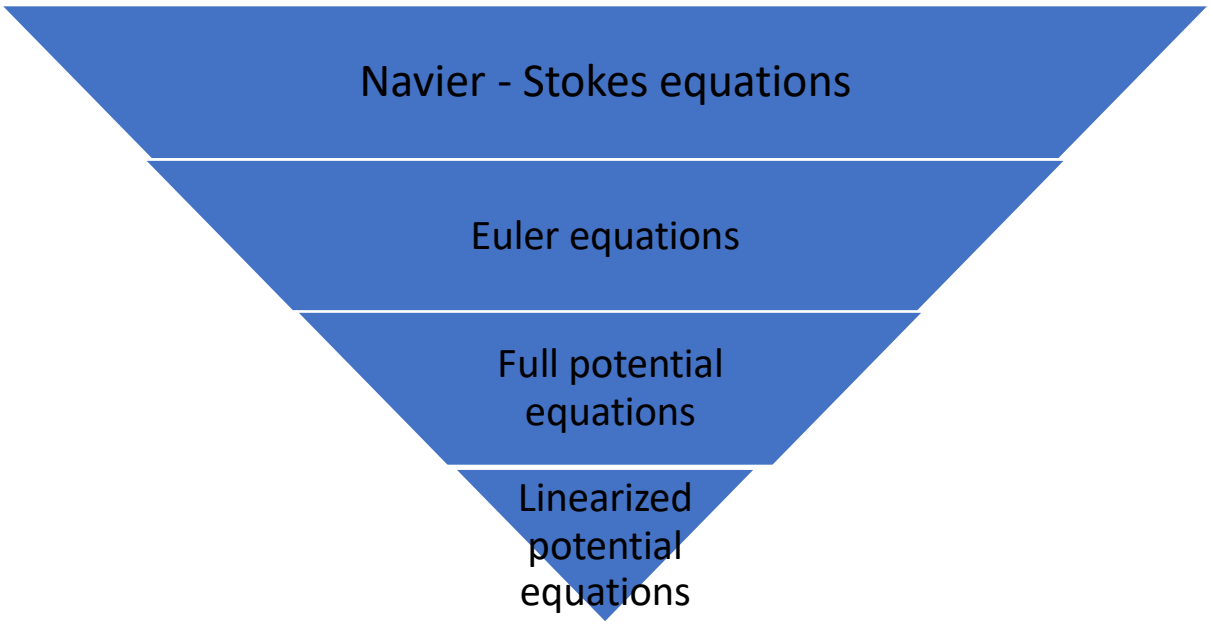

4.2. Core principles

Fluid flow is governed by three fundamental conservation laws:

1. conservation of mass,
2. conservation of momentum, and
3. conservation of energy.

Mathematical formulation of these laws leads to the governing equations for fluid flow. And these could be partial differential equations or integral equations. If one applied the governing equations to an infinitesimal fluid particle moving within the flow, one gets the partial differential equations.

A complementary view is to apply the conservation laws to a fixed volume in the flow domain, the control volume. And in that case, one gets the integral form of the governing equations. The two are equivalent. In either case, these equations are coupled and nonlinear. This means that they can be solved exactly for a very small number of special cases. In computational fluid dynamics, or CFD, the governing equations are solved approximately, on the computer using software. The software converts the governing equations to a large set of algebraic equations. That is, it uses numerical methods. It goes from calculus to linear algebra. And the large set of algebraic equations is inverted on the computer. Current CFD technology can handle flow around realistic geometries and complex physics.

The numerical technique used to solve the governing equations of fluid flow is the finite volume method. ANSYS Fluent uses this method, as do many other commercial CFD codes. And the basic idea of the finite volume method is to take the flow domain and divide it into smaller control volumes and apply conservation to each little part. And this is done using the integral form of the governing equations. The net result is a set of algebraic equations. The finite volume method applies conservation directly rather than indirectly, so for each little volume element, it is applying conservation and it conserves quantities in a discrete sense.

In order to move from from the mathematical model to the numerical solution, finite volume method is employed. For software to properly solve for the required variables it follows the steps outlined in the figure 18.

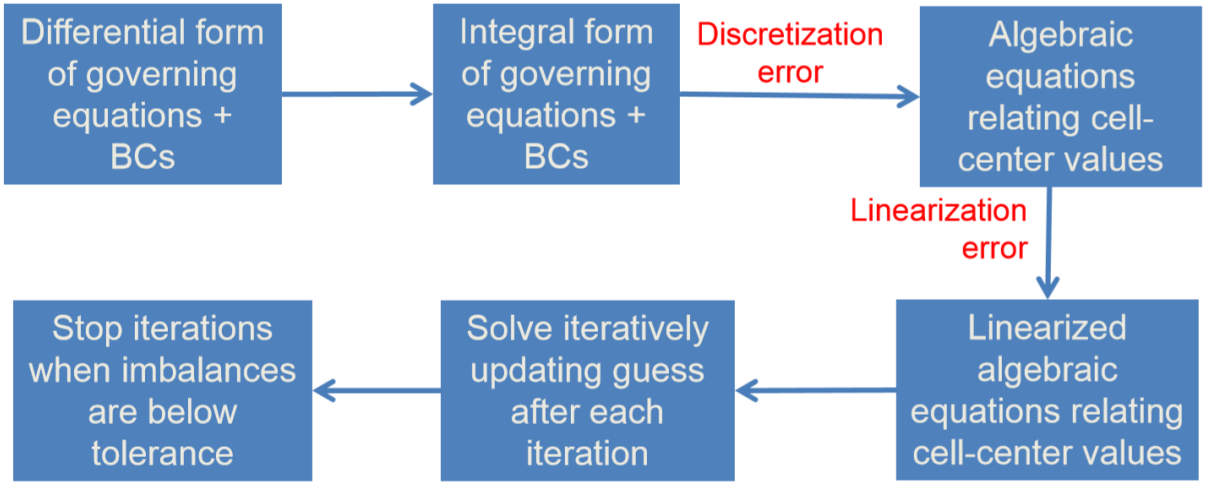

Figure 18. Flowchart for going from differential equations to set of variables

The first step in the finite volume method is to divide the domain into multiple control volumes or cells. The idea is not to try and determine the unknown functions, but to try and determine the necessary variables at the selected points, which are usually cell centers, of the small volume elements. This process is called discretization – when the problem is reduced to determining just a finite set of values.

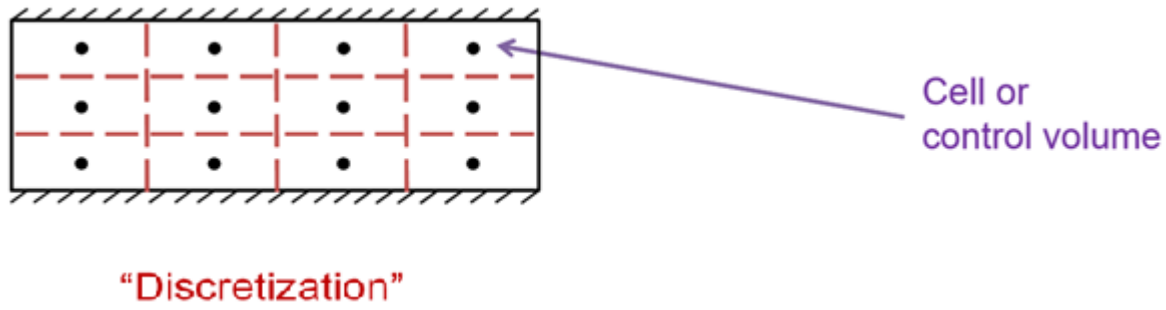

Figure 19. Discretization scheme

Cell center values are approximations of the cell average values. And this flavor of the finite volume method is called the cell centered finite volume method. There are other flavors of the finite volume method, particularly the so-called node centered, or the vertex centered finite volume, where the unknowns are determined directly at the corners or the vertices. That methodology is a variation on the cell centered methodology. Focus of this paper will be on the cell centered methodology. That is the methodology implemented in ANSYS Fluent.

In order to find velocity and pressure at each cell, software starts with the mathematical model, which is a boundary value problem (differential equations plus boundary conditions) and then derives a system of algebraic equations in the cell center values from that. These equations are generated by performing a control volume balance for each cell.

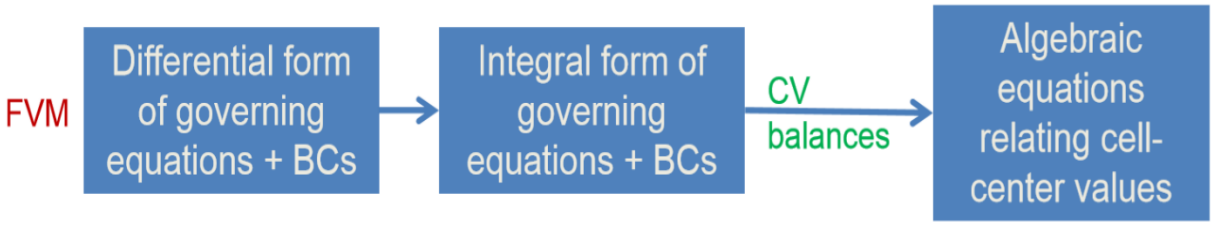

Figure 20. Control volume balance diagram

Each algebraic equation will relate a cell center value to its neighbors. And then the system of algebraic equations will be solved. Computer can invert it to get the cell center values for necessary variables. In this case, due to software licensing and personal computer power, not more than 250 thousand algebraic equations can be solved, however, engineers are now doing problems with more than billion unknown values.

Everything else is extracted from those cell center values for u, v, p, T, e. For instance, the pressure field, the velocity field, wall shear, et cetera, and that is done through the process called post-processing. That is the framework of how the software finds the velocity, pressure, and other variables at the cell centers and derive everything else needed to know from that.

The two major ideas are discretization and linearization. And the end point of the discretization is a set of algebraic equations relating neighboring cell-center values. And that is derived from the integral form of the governing equations by doing control volume balances

cell by cell. And in the process of going from the integral form to the set of algebraic equations, an error is introduced called the **discretization** error. The discretization error can be reduced by using more cells in the domain. That is called mesh refinement. Or it can be decreased by increasing the order of accuracy of the interpolation.

The algebraic equations derived are nonlinear, so they must be linearized about a guess value. And when going from the nonlinear set of algebraic equations to linearized algebraic equations relating cell-center values, another error is introduced called the **linearization** error. These two errors are different. And to decrease a linearization error, software tries to solve iteratively, and after each iteration, it updates the guess. And it stops iterating when imbalances of mass and momentum are below some selected tolerance. If there were exact solutions to the nonlinear algebraic equations, the imbalances of mass and momentum would be zero. But since there is a linearization error, it is never going to be zero. But if it is below a tolerance, then the linearization error is acceptable.

There is a common misconception that by refining the mesh and thus increasing the number of cells the linearization error should go down. However, what happens is that the iterations become harder to converge. What is achieved, is that the discretization error has gone down, but linearization error has increased. These are two entities that must be balanced. Their relationship along with the total numerical error are shown in fig. 21.

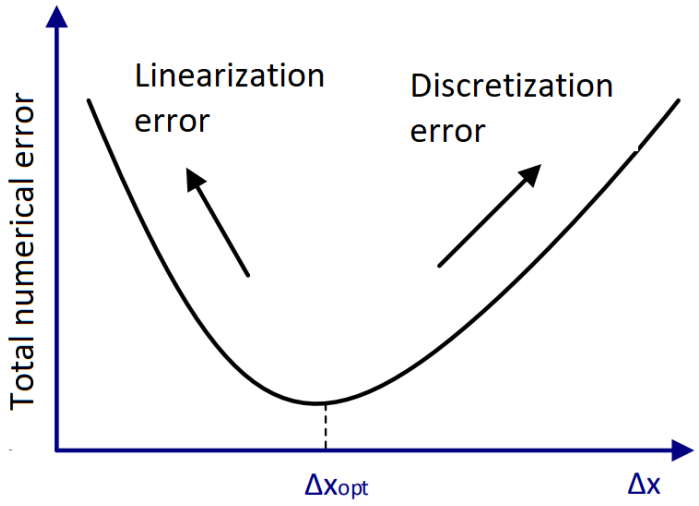

Figure 21. Total numerical error

The aggregate mass imbalance or a mass residual is a key parameter when solving iteratively. It is a sum of all the mass imbalances in all the cells. The iteration process is repeated until the cumulative mistake or residual is under a limit. It is also referred to as the continuity residual. The numerator is the absolute value of the mass residual for each cell and it is added all up. Equation 33 Shows how the **residual value** is calculated.

$$R = \frac{\Sigma\,|R_i|}{Scaling\ factor} \tag{33}$$

It is the absolute value, because whether this residual is positive or negative, it is an error. The reason a scale factor is used is that what would seem like a small mass imbalance for

a supersonic flow might be a large imbalance for a low-speed flow. So, the scaling factor ensures that it is the aggregate mass imbalance, relative to the aggregate kind of mass inflow or mass outflow to each cell.

The solver stops iterating when this aggregate mass imbalance is less than some tolerance. And the tolerance, the default is 10^{-3} in the Fluent solver, but that can be changed. And the same idea applies to the momentum equation, too. So, if looking at x-momentum, the net x-momentum outflow should be balanced by the net forces in the x-direction on the control volume. And any part of the momentum outflow that is not balanced by the forces is an error. And so, it is the momentum residual which is analogues to the mass residual.

Let us now go through a step by step process of obtaining the simulation results. The first step was the geometry setup, for which the coordinate data was computed in MATLAB and then imported and finalized in the Design modeler. Afterwards, mesh controls and setup were selected. Later in the chapter it will be explained what the various options are used for, and how do they aid in the algorithm guidance for the grid generation. Next, solver settings and solver preference is commented, along with the boundary and flow conditions. It is pointed out why the k-w SST model along with the pressure-based coupling algorithm is selected. Finally, results obtained via the selected settings are commented with multiple graphic outputs of the generated simulation.

To complement the explanations and discussion further down the chapter, please refer to [14]. It is an official help manual from Ansys Inc., and it is explained in much greater detail and depth on how and why selected properties and settings are suitable for this studies simulation. All of the text later in this chapter is mostly from [14].

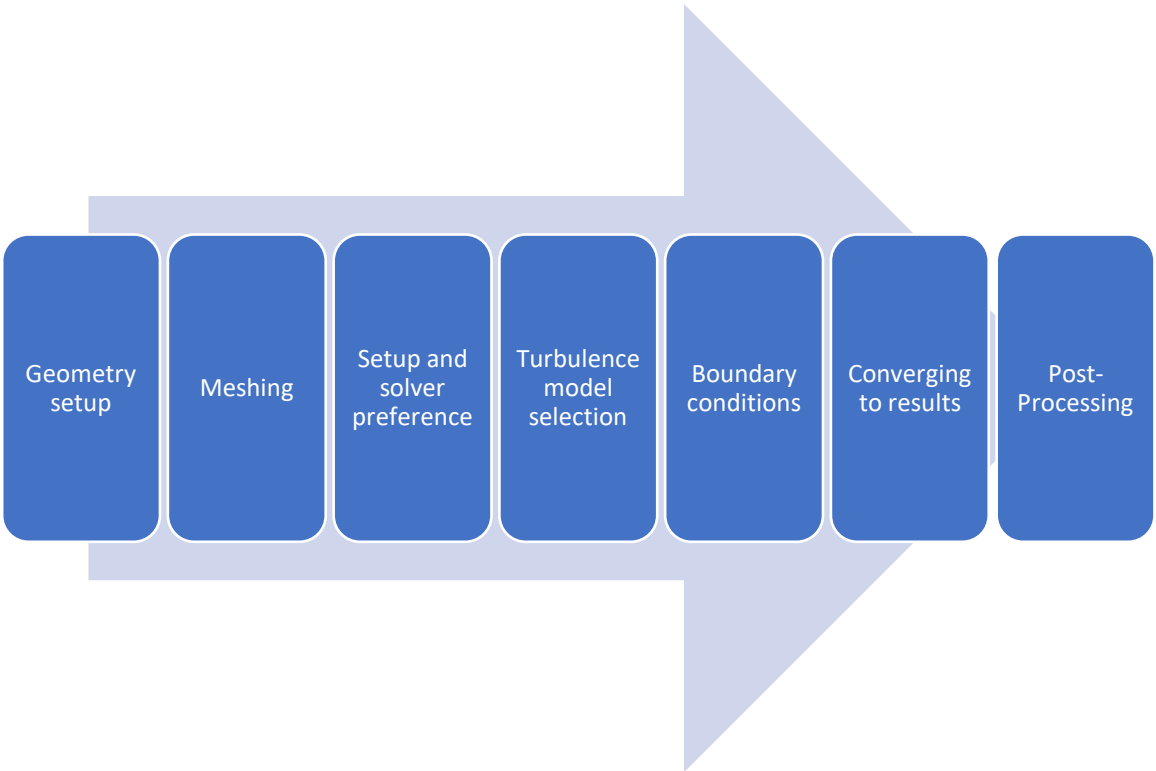

4.3. Geometry setup in Design Modeler

For the geometry of the airfoil, coordinate file was manufactured and then exported from MATLAB into the Design Modeler –a CAD part of the Ansys software. The flow field was then created around the airfoil, and it was created in a C-section type. The radius of the half circle in front of the airfoil was 10 chords long, whereas the length of the area behind the airfoil was 12 chords. Those length values have been proven to be enough, as to not receive the reverse back flow, and other various effects which may occur if the flow field area is too small. The idea is to simulate the flow through the flow domain, and to cut out the surface of an airfoil from the flow domain, so it acts as a wall over which the free stream flows.

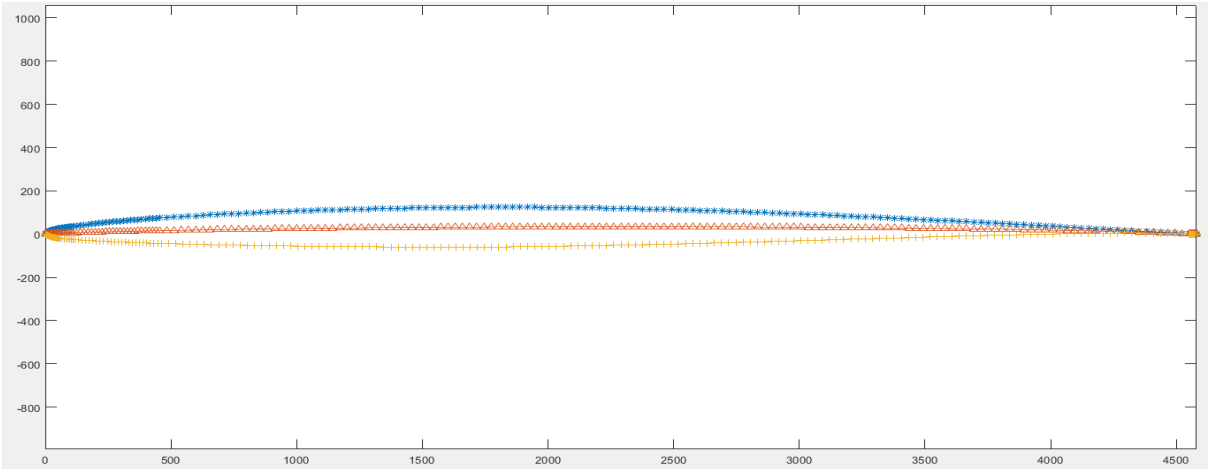

Figure 22. Matlab computed coordinate points

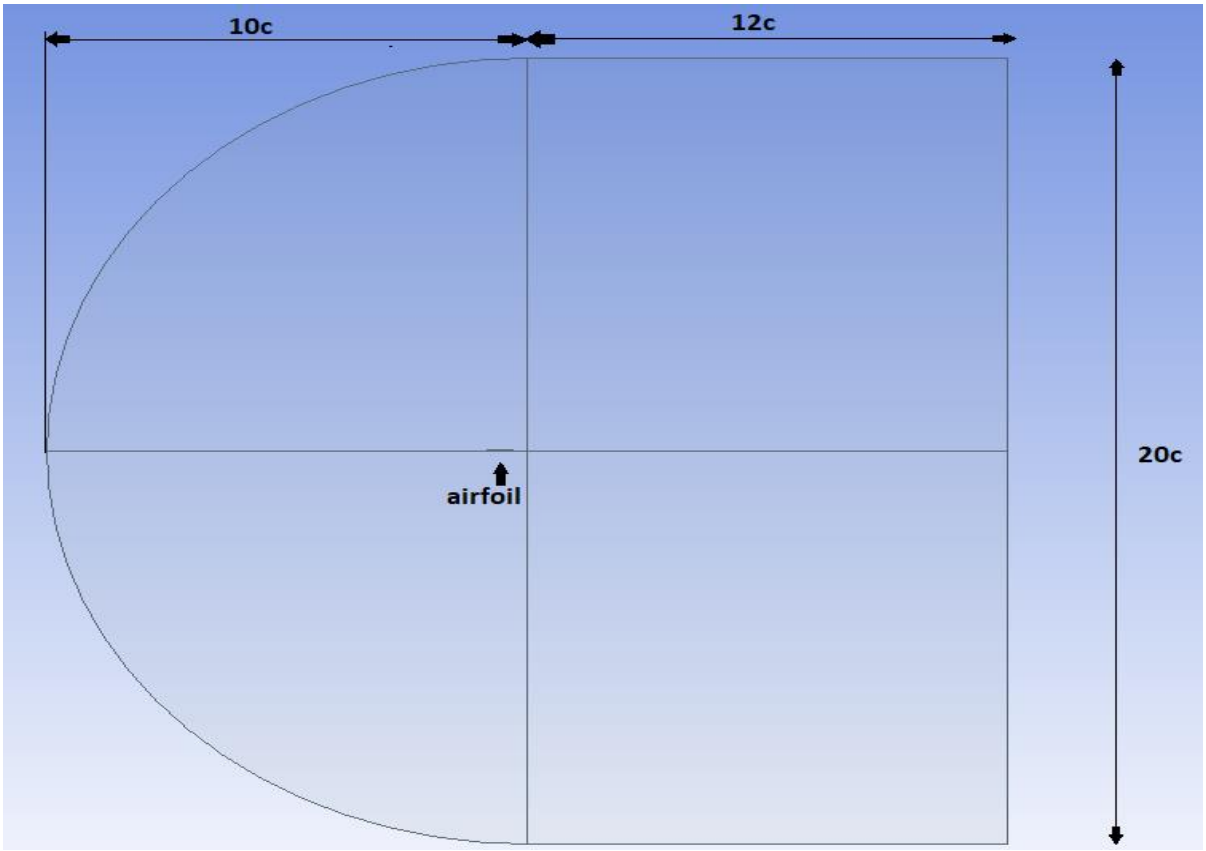

Figure 23. Flow domain

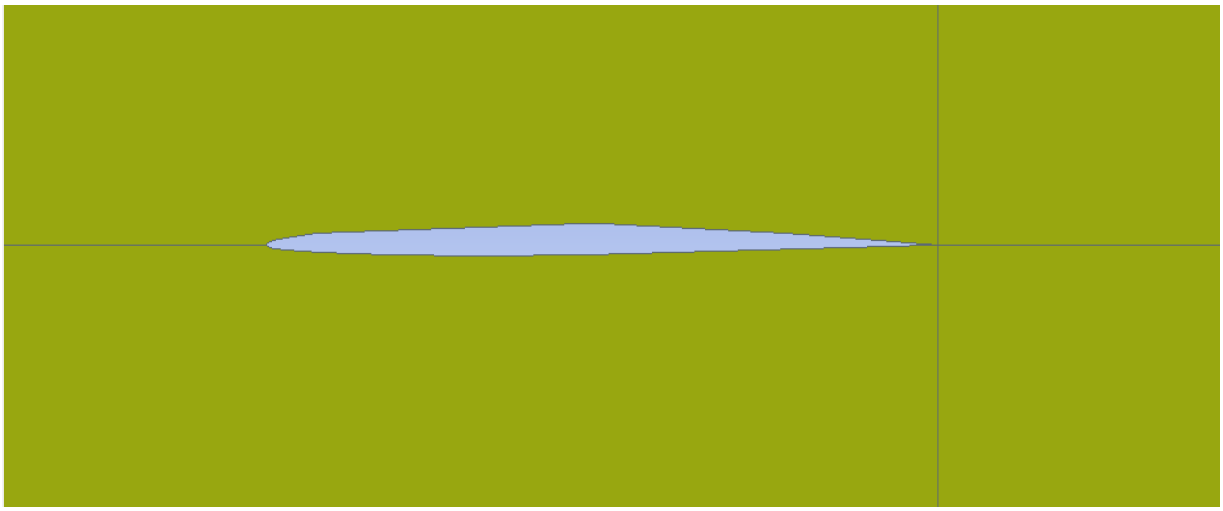

Figure 24. Airfoil surface cut-out

4.4. Meshing

After successfully creating the geometries of both the airfoil and the surrounding flow field, the next step in the process of obtaining the required results is discretization of the area or as it is better known – meshing. Meshing process is about 50% of the work. After a successful transition of the model from the design modeler, meshing can be approached in two ways: global and local. Global mesh controls are applied to the entire grid whereas local meshing options are available from the mesh control menu and they are applied locally to selected features. There are various options to select from, like: mesh methods, different sizing options, mapped mashing for structured geometry appliances, inflation layers for capturing near surface behavior, and many other fine-tuning options.

By choosing the CFD for physics preference, option to select a preferred solver becomes available. For this study, the FLUENT solver is selected. Based on the selection, the software will try to generate the mesh which fits the solver.

Important setting for global meshing options is selecting the **element size**. Too small of a size can result in a too fine of a mesh which will devourer the working memory and thus require large quantities of time to converge. However, setting the element size too big will result in a coarse mesh which probably will not capture all the fine details necessary.

During mesh generation, an element's quality is calculated. The meshing algorithm uses error limits to obtain a valid mesh. It performs extra mesh cleanup to ensure the error limits are met, such that a valid mesh is one that satisfies the minimum conditions and can be received by the solver. The meshing algorithm then attempts to improve quality based on the targeted limits.

For the CFD physics preference, the most important mesh metric option is the **Orthogonal Quality.** When a mesh metric is selected, min, max, average and standard deviation values are reported. Figure 25. portrays the orthogonal quality inspection.

It can be seen how most of the elements are in the range from 0.88 to 1.00, which means that most of the elements are good quality. Even though there are elements with 0.25 and lower quality, the solver can work with them if they are surrounded by enough of the good elements.

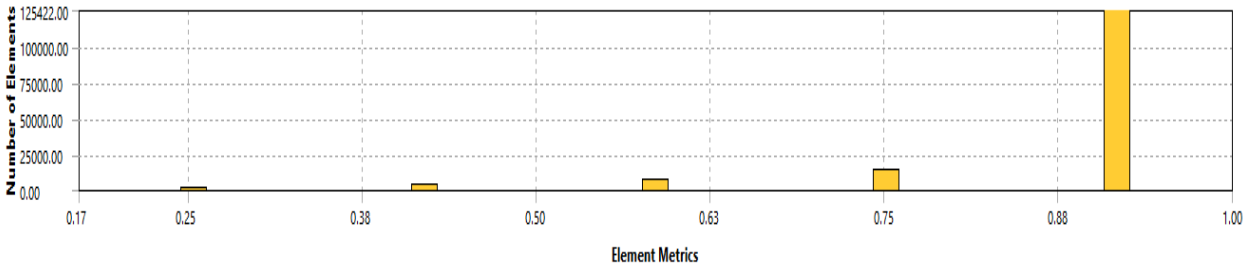

Figure 25. Element quality - Orthogonal Quality

Orthogonal quality can range from 0 (worst) to 1 (best). The orthogonal quality for cells is computed using the face normal vector, $\overrightarrow{A_i}$ for each face; the vector from the cell centroid to the centroid of each of the adjacent cells, $\overrightarrow{c_i}$; and the vector from the cell centroid to each of the faces, $\vec{f_i}$. Figure 26. Shows the vector relations between cell centers, and the vectors used for determining the orthogonal quality of a cell.

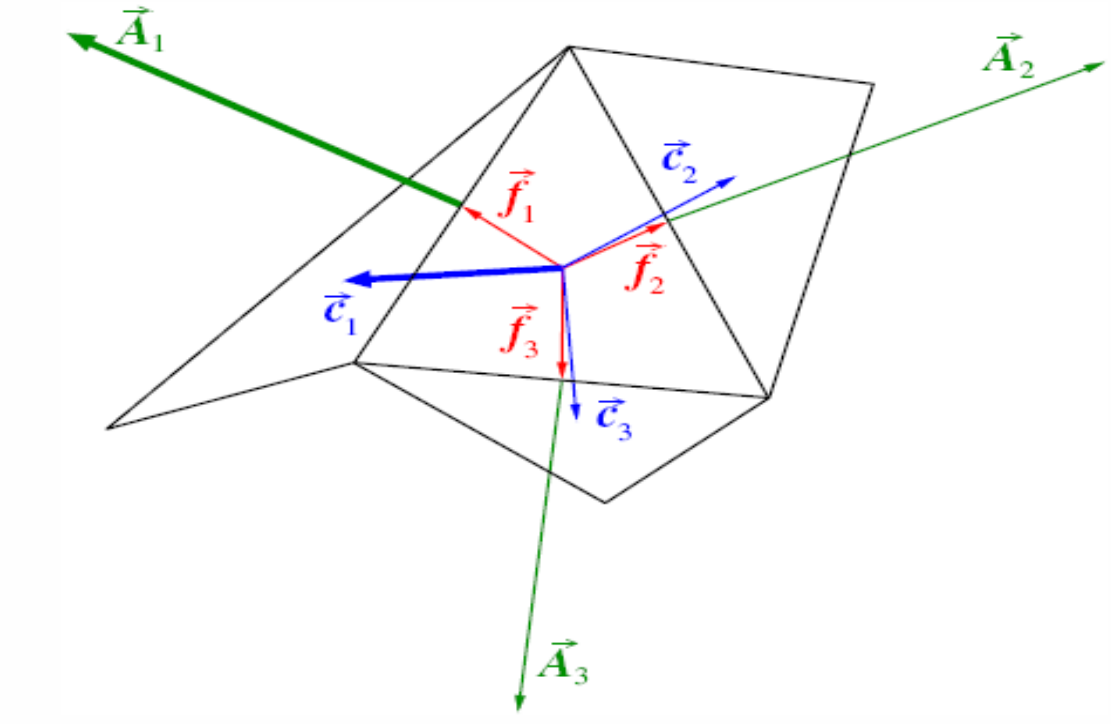

Figure 26. Orthogonal quality calculation

For each face, the cosines of the angle between $\overrightarrow{A_i}$ and $\overrightarrow{c_i}$, and between $\overrightarrow{A_i}$ and $\vec{f_i}$, are calculated. The smallest calculated cosine value is the orthogonality of the cell.

4.5. Condition and solver option setup

After completing the mesh procedure, next step is setting up the conditions and preferred solver options. The General task page allows to set various generic problem settings, such as those related to the mesh or the solver.

For this study a **pressure-based coupled** solver is selected. Historically speaking, the pressure-based approach was developed for low-speed incompressible flows, while the density-based approach was mainly used for high-speed compressible flows. However, recently both methods have been extended and reformulated to solve and operate for a wide range of flow conditions beyond their traditional or original intent.

In both methods the velocity field is obtained from the momentum equations. In the pressure-based approach, the pressure field is extracted by solving a pressure or pressure correction equation which is obtained by manipulating continuity and momentum equations. Using either method, ANSYS Fluent will solve the governing integral equations for the conservation of mass and momentum, and (when appropriate) for energy and other scalars such as turbulence and turbulence dissipation rate.

The pressure-based solver employs an algorithm which belongs to a general class of methods called the projection method. In the projection method, wherein the constraint of mass conservation (continuity) of the velocity field is achieved by solving a pressure (or pressure correction) equation. The pressure equation is derived from the continuity and the momentum equations in such a way that the velocity field, corrected by the pressure, satisfies the continuity. Since the governing equations are nonlinear and coupled to one another, the solution process involves iterations wherein the entire set of governing equations is solved repeatedly until the solution converges.

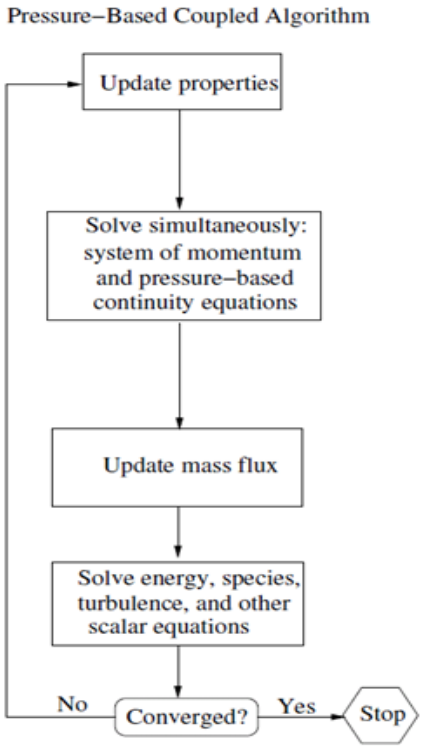

Figure 27. Pressure-Based Coupled Algorithm flow chart

The pressure-based coupled algorithm solves a coupled system of equations comprising the momentum equations and the pressure-based continuity equation. Since the momentum and continuity equations are solved in a closely coupled manner, the rate of solution convergence significantly improves when compared to the segregated algorithm. However, the memory requirement increases by 1.5 – 2 times that of the segregated algorithm since the discrete system of all momentum and pressure-based continuity equations must be stored in the memory when solving for the velocity and pressure fields.

After selecting the solver, the next major decision is choosing the turbulence model. The **k-omega SST** turbulence model is a two-equation turbulent-viscosity model that is used for many aerodynamic applications. It is a hybrid model combining the k-omega and the k-epsilon models. It uses blending functions to activate the k-w model near the wall and the k-epsilon model in the free stream. This ensures that the appropriate model is utilized throughout the flow field:

- The k-omega model is well suited for simulating flow in the viscous sub-layer.
- The k-epsilon model is ideal for predicting flow behavior in regions away from the wall.

The **k-e** model was developed first, and it was found that the damping functions for the near-wall treatment used in the k-e model became unreliable when applied to the variety of the flows different to the original flows used for calibration. So the **k-w** model was developed to give better near-wall treatment, that is less sensitive and doesn't require near wall damping functions. It was then discovered that the solution values from the **k-w** model were very sensitive to the free stream turbulence values applied at the inlet for the computations. Even a small change in the starting values could have a big impact on the results.

For both the **k-w** and **k-e** models it was found that the flow was not separating correctly from the smooth surface of the body when compared to the experimental results, and this was primarily because the wall shear stress was too high from these models. So the **k-w SST** model was proposed by Menter in 1993 [15]. In an attempt to address some of these problems and give better separation results for external aerodynamical flows. For additional explanation and discussion about model differences and reasons for selecting the k-w SST please refer to appendix A.

4.6. Boundary conditions

Boundary conditions in fluid dynamics are the set of constraints to boundary value problems in computational fluid dynamics. These boundary conditions include inlet boundary conditions, outlet boundary conditions, wall boundary conditions, constant pressure boundary conditions, axisymmetric boundary conditions, symmetric boundary conditions, and periodic or cyclic boundary conditions.

The governing equations are the same for whatever the flow is. Weather it is over a large transport aircraft or past a windmill. However, the flow fields are quite different for these cases,

although the governing equations are the same. The difference enters with the Boundary conditions which are quite different for each of the above mentioned.

Boundary conditions, sometimes called the initial conditions, dictate the particular solutions to be obtained from the governing equations. When the geometric shape of a large transport aircraft is treated, when certain physical boundary conditions are applied on that particular geometric surface, and when the appropriate boundary conditions associated with the free-stream far ahead of the airplane are invoked, then the resulting solution of the governing partial differential equations will yield the flow filed over the transport aircraft

This is in contrast to the flow-field solutions that would be obtained for a windmill if the geometric shape and freestream conditions pertinent to the windmill were treated. Hence, once the governing flow equations are obtained, then the real driver for any particular solution is the *boundary conditions.* This has a particular significance in CFD; any numerical solution of the governing flow equations must be made to see a strong and compelling numerical representation of the proper boundary conditions [16].

For a viscous flow, the boundary condition on a surface assumes zero relative velocity between the surface and the gas immediately at the surface. This is called the ***no-slip*** condition. As for the inlet and outlet boundary conditions, particularly interesting is the ***pressure far-field*** condition. Pressure far-field conditions are used in ANSYS Fluent to model a free-stream condition at infinity, with free-stream Mach number and static conditions being specified. The pressure far-field boundary condition is often called a characteristic boundary condition, since it uses characteristic information (Riemann invariants) to determine the flow variables at the boundaries.

Pressure far-field boundary condition is applicable only when the density is calculated using the ideal-gas law. Using it for other flows is not permitted. To effectively approximate true infinite-extent conditions, the far field boundary must be placed far enough from the object of interest.

4.7. Converging to results

The way of obtaining results was discussed in previous chapters. After specifying the flow and boundary conditions, the software goes from partial differential equations to algebraic equations and tries to iteratively guess the values for all the variables that we wish to obtain. Ansys solver allows the user to specify the mass, momentum, energy, k and w residuals for which to aim as to accept the results as correct. It is not always easy to achieve smooth convergence of the results. If there are low quality mesh cells, or if the specified conditions are not physically possible, or if there are too large gradient changes in variable fields it is very easy for software to diverge and never to obtain proper results. That is why with the experience the user learns how to guide the software in order to achieve the wanted convergence.

On the three figures below (28-30) a case is presented in which it can be seen how the result chart looks after 2500 iterations. Even though the results seem to converge after around ~500 iterations, if there is enough time it is always recommended to allow the software additional iterations. Next to the defaults monitoring of the *continuity*, *velocity*, *energy and k* &

w residual values, it is a usual practice to monitor additional terms. In this case, the *lift* and *drag* coefficients are monitored. It serves as additional proof and validation of the result convergence. It can be seen how the result is unstable in the first ~ 250 iterations. That can especially be seen in the lift and drag coefficients which act very unstable. However, after further assessment and cell center value guessing, after additional iterations, the software, based on the selected settings and the preferred solver along with the correct turbulence model starts converging and finally arrives at a stable state. Even though the largest (continuity) residual is only at around 10^-3, based on other residuals and on the *lift* and *drag* coefficient behavior, it is enough to call it correct.

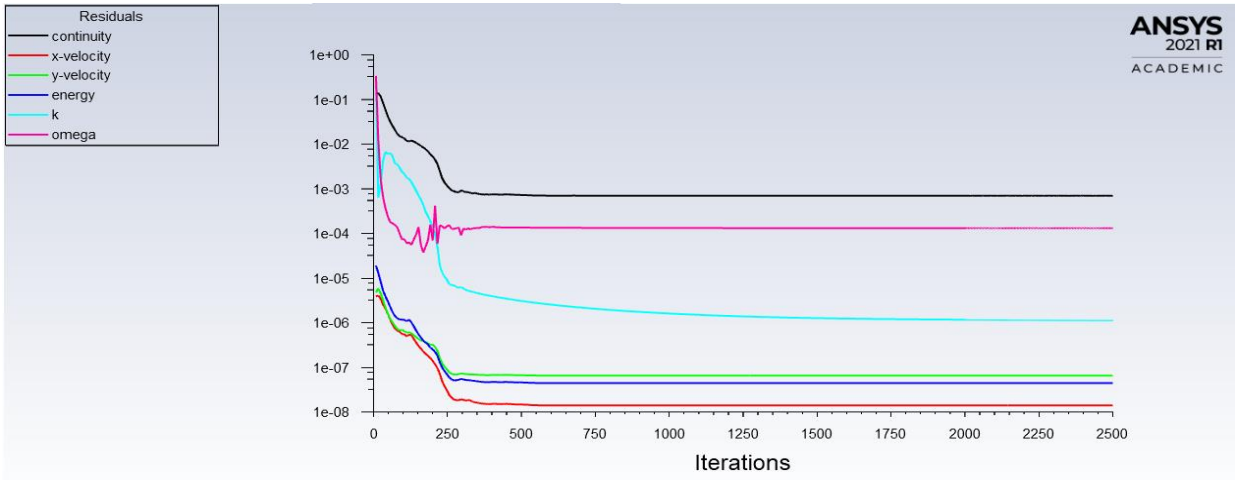

Figure 28. Residual behavior

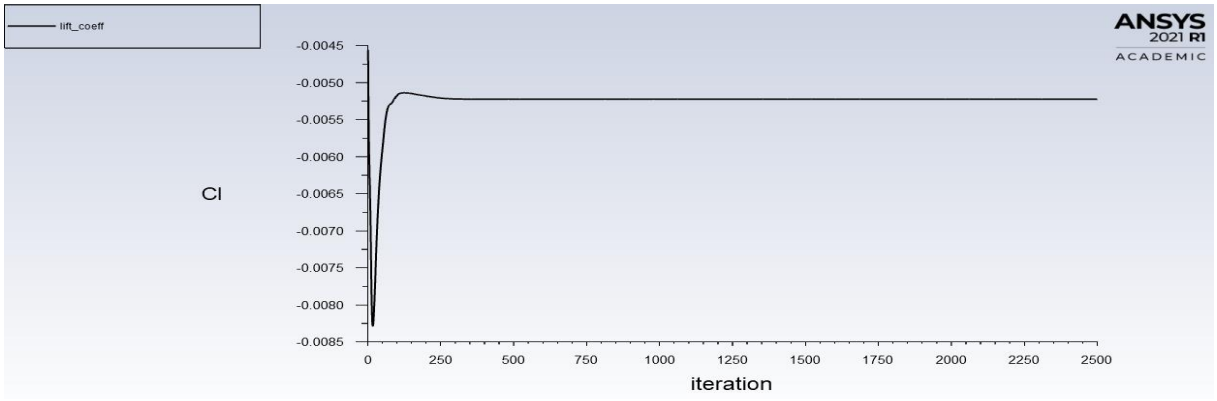

Figure 29. Lift coefficient changes over 2500 iterations

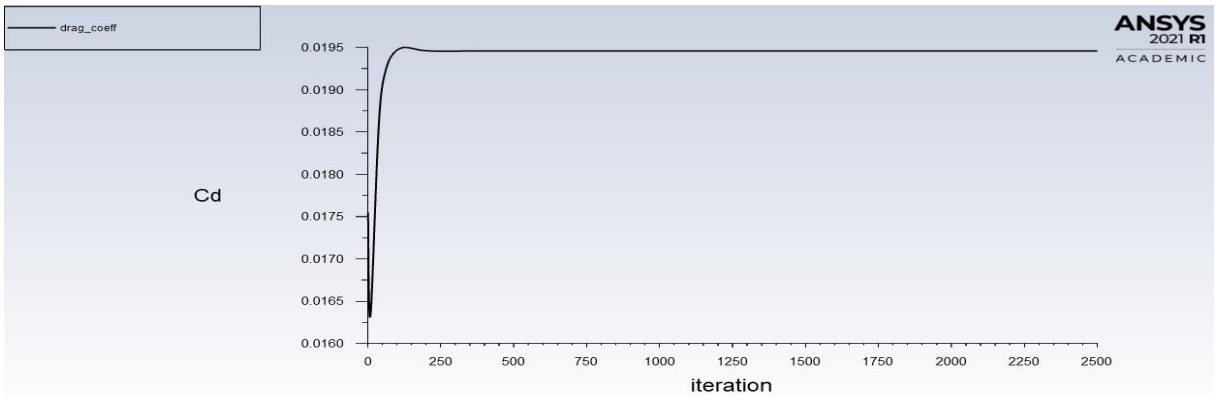

Figure 30. Drag coefficient changes over 2500 iterations

5. CFD Design, Simulation and Analysis of NACA 64_A-204

This chapter will discuss how the CFD setup is used and modeled for the specific case of the NACA 64_A-204 airfoil – the one used in the F-16 wings. Most of the setting and options are described in the chapters above. For additional information please refer to reference [14].

5.1. Grid

Meshing was performed by using the options described in the above chapter.

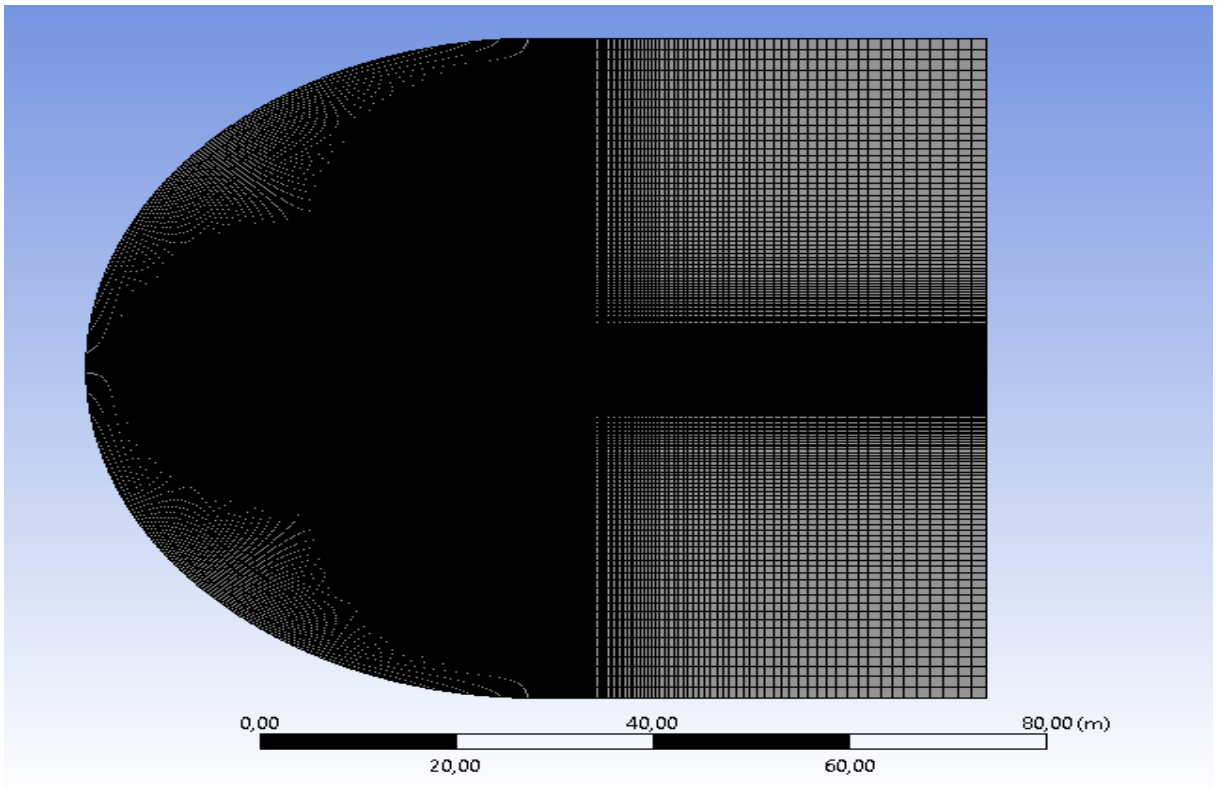

Figure 31. Structured C-section type grid

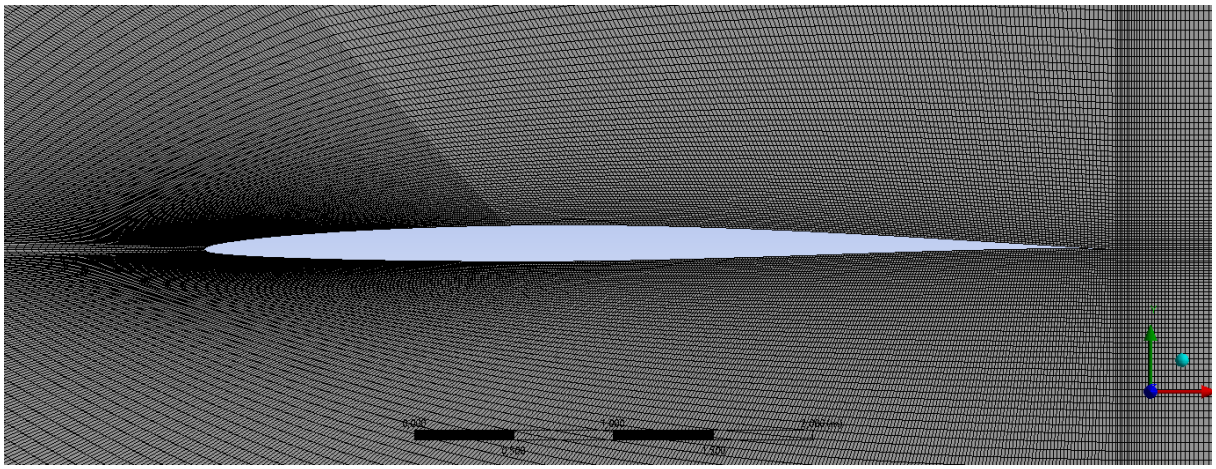

Figure 32. Mesh around the airfoil

A standard C-section type was created. It is a common approach in the external aerodynamical flows over airfoil surfaces. Grid is made in a structural way in order to obtain higher mesh element quality. Even though the Finite Volume method can work with irregular cell shapes, having a structured mesh helps in the amount of time required for the results to converge, as well as in the presentation of the results in the post processing, which will be shown later. Figure 31 shows the structured grid over the entire flow domain.

The entire grid domain is focused around the airfoil – which is the most important part of the flow field. Figure 32 shows the element distribution closely around the airfoil surface.

5.2. Setup, solver and boundary conditions

For the solver, the **pressure-based solver** is selected. Reasons for selecting this solver are described in the previous chapters. It is a truly versatile solver which can be used for many different aerodynamical external flows. It certainly covers the conditions under which the flow is modeled for this case. Velocity formulation is absolute, and since no axes were used for any kind of symmetry the 2D space is defined as **planar**. Time is steady – there are no changes to the flow after setting the initial boundaries and conditions.

The point of the simulation was to conduct studies by solving full Navier-Stokes equations and that is why the viscosity effects could not be omitted. Since that is the case, the solver is set to viscous k-w SST two equations model which is explained in more detail in **Appendix A**. The ability of the solver to change its mathematical formulation depending on the distances from the wall is a key factor which had to be taken into account.

Material selected for the flow fluid is air, but in order to account for the compressibility at higher Ma numbers, the density is based on the ideal gas law. Viscosity of the air is based on the Sutherland's three coefficient law. Since the thermal reactions and thermal analysis isn't the focus of this study, the material from which the airfoil is created isn't important.

For the boundary conditions, the flow inlet was selected as the Far Field Pressure inlet which is used to model free-stream compressible flow at infinity, with free-stream Mach number and static conditions specified. This boundary type is used only for compressible flows. As discussed earlier, the idea was to create a large enough flow field and then to cut out the surface of the airfoil so it will act as a wall over which the flow will stream. That is why the airfoil surface is defined as a **no-slip wall** boundary. Which means that the velocity profile at the distance next to the wall is equal to 0.

The reference value used for calculation of the lift and drag forces and coefficients is based on the length of the airfoil chord. Since this is a 2D study case, the area of importance is simply the product of the airfoil chord length times one. c = 4.58m , A=4.58m^2

The pressure-velocity coupling scheme is set to Coupled. The spatial discretization settings are shown in the figure 33.

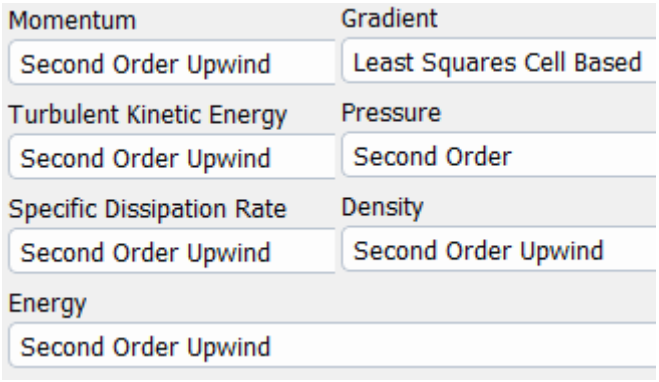

Figure 33. Spatial discretization settings

In order to make a change in the Angle of attack, the pressure far field inlet was varied based on the X and Y vector components of the incoming steam. By simple calculation of the cos() and sin() values of a desired angle and the initial velocity value, different angles of attack were simulated.

5.3. Results

Figures 34. And 35. show the pressure coefficient distribution for subsonic and supersonic cruise configurations, respectively, under Ma = 1.5 condition.

Figure 36. shows velocity and pressure distribution around the airfoil in the subsonic cruise configuration at Ma = 1.5 and AoA = 0 ^{o}, whereas figure 37. shows the distribution around the reflexed for high speed cruise configuration.

Stronger shockwave can be observed on the figure 36., thus resulting in a slightly larger drag coefficient value for the 0 degrees angle of attack. It can also be seen how the position of the largest pressure value is slightly above the nose of the airfoil which results in a negative value of the lift coefficient.

By reducing the camber line – employing the supersonic cruise configuration – the highest pressure is moved somewhat towards the centerline resulting in a smaller negative lift coefficient.

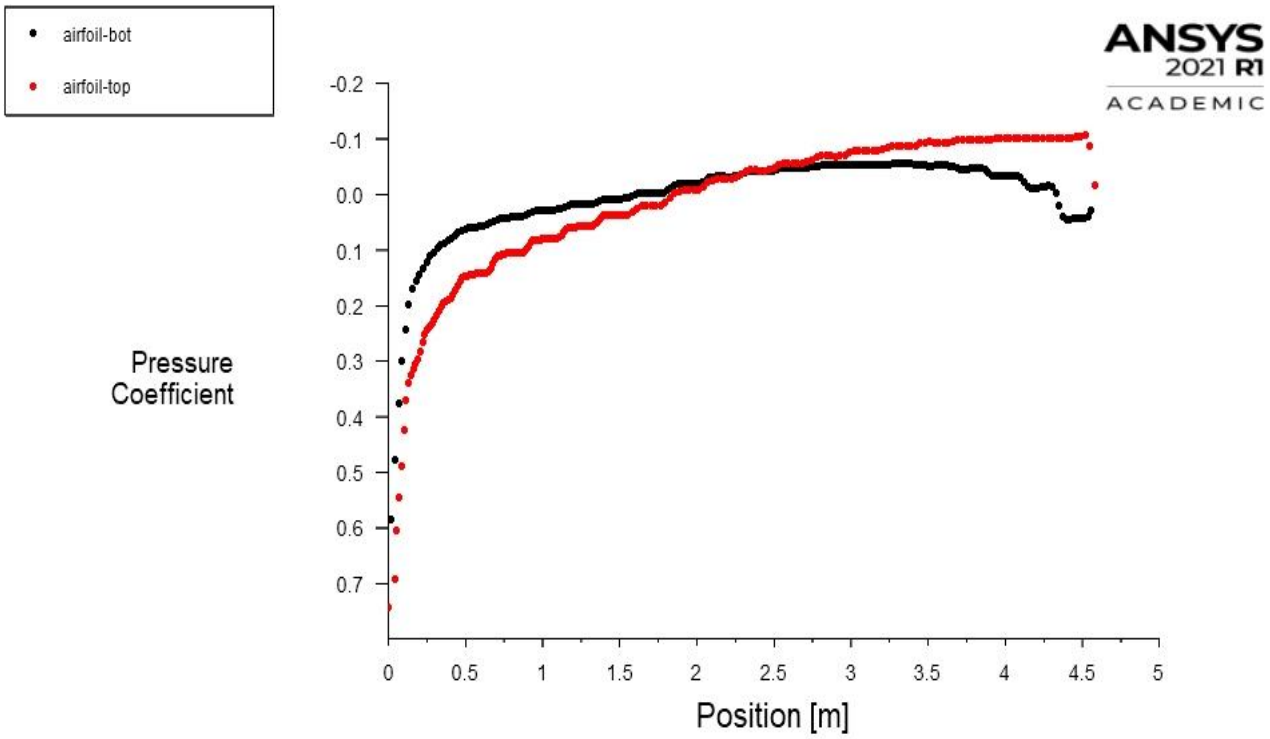

Figure 34. CFD pressure coefficient distribution - subsonic cruise configuration, Ma=1.5, AoA=0°

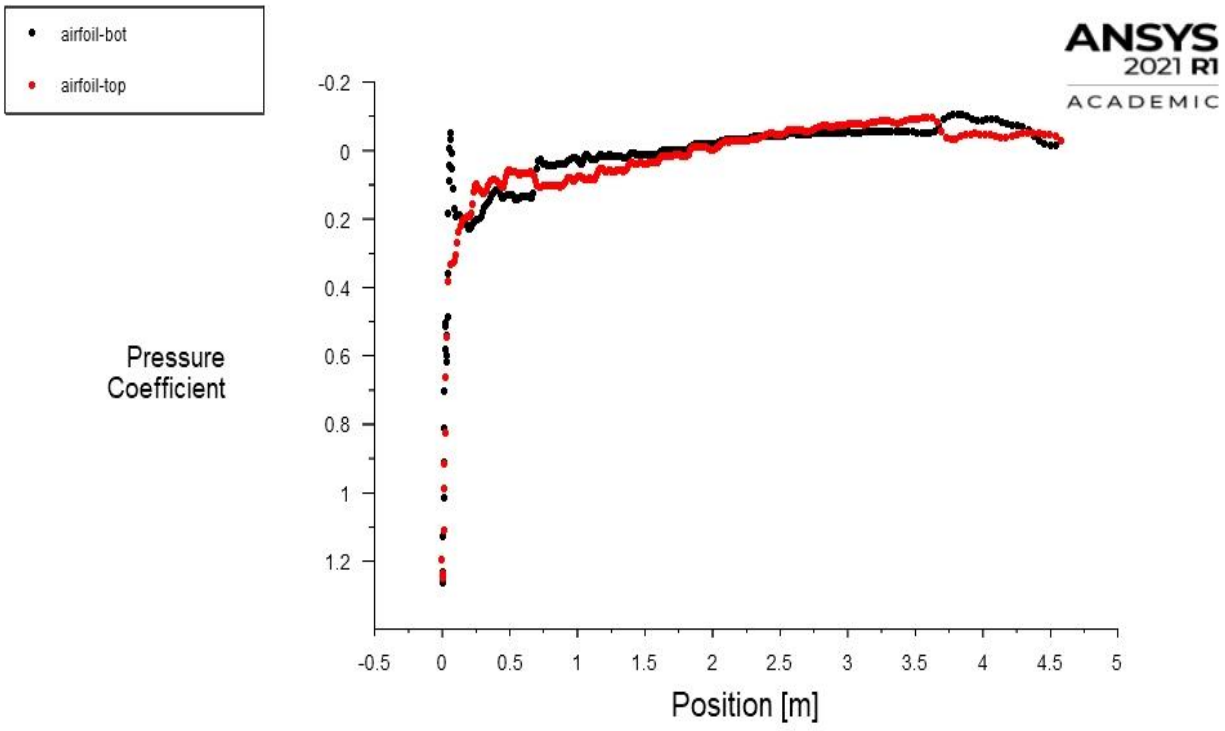

Figure 35. CFD pressure coefficient distribution - supersonic cruise configuration, Ma=1.5, AoA=0°

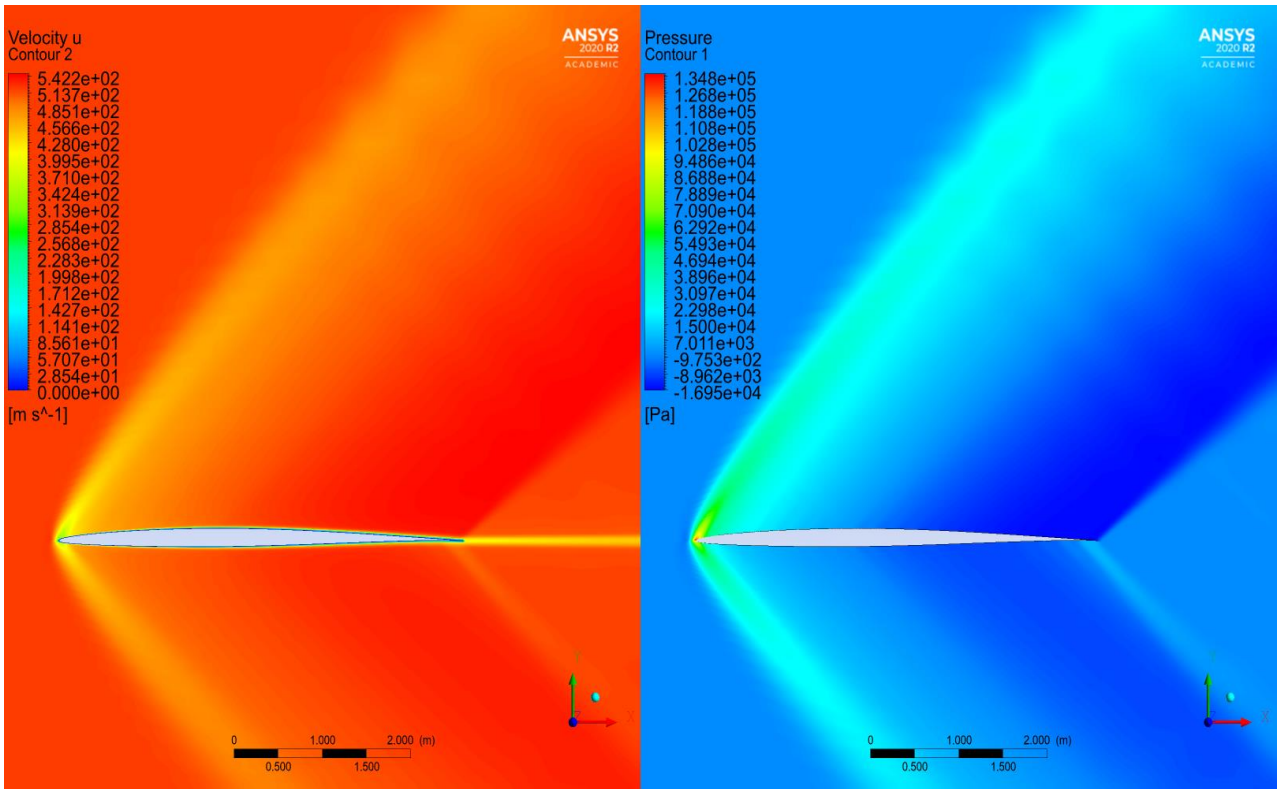

Figure 36. Pressure and velocity distribution, Ma=1.5, AoA=0 °, subsonic cruise configuration

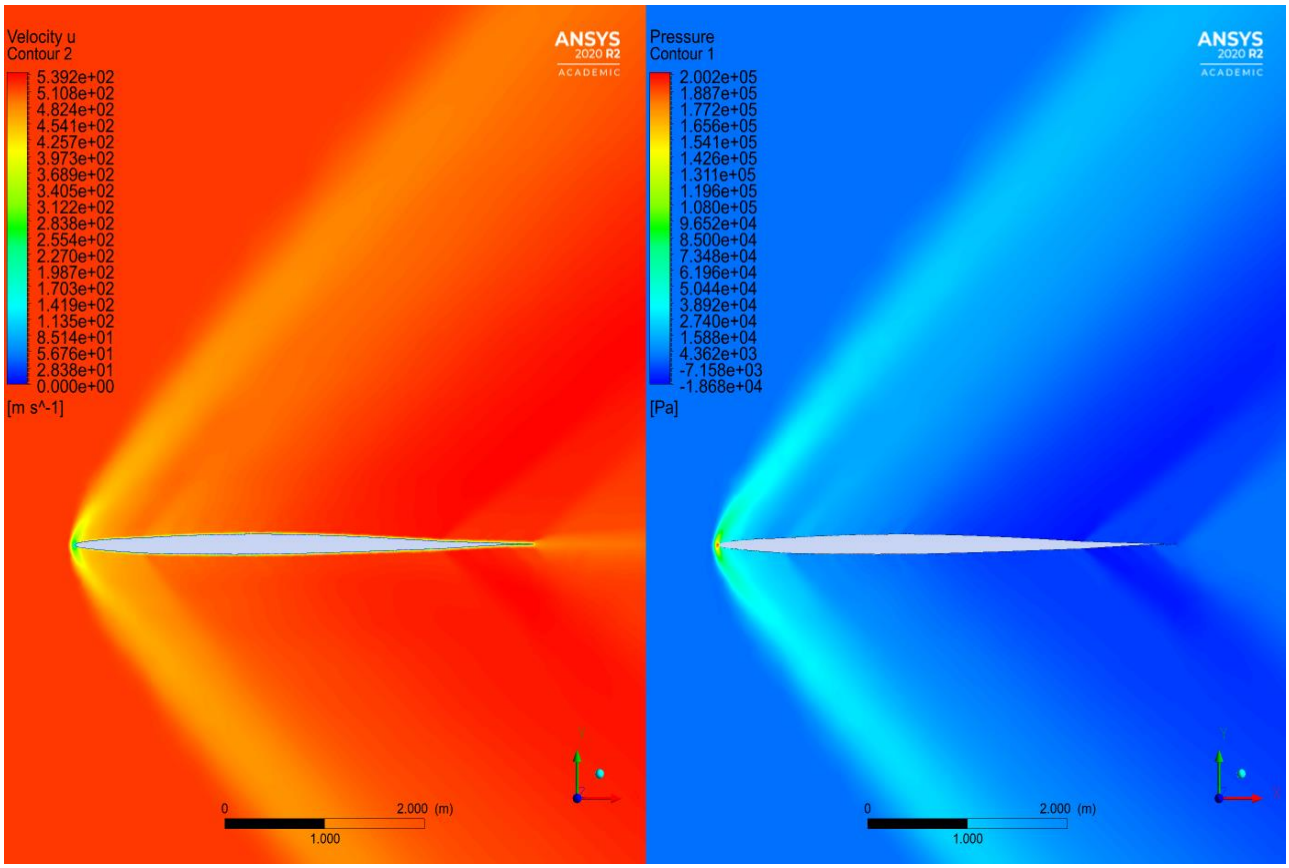

Figure 37. Pressure and velocity distribution, Ma=1.5, AoA=0 °, supersonic cruise configuration

As with the analytical part, the simulations were conducted degree by degree up to 12 degrees angle of attack. The results for lift and drag coefficients can be seen in the table below.

Table 4. Lift and drag coefficients predicted by the CFD for AoA=0:12

Angle of attack	Subsonic cruise configuration		Supersonic cruise configuration	
	Cl	Cd	Cl	Cd
0°	-0.0052	0.0195	-0.0044	0.0175
1°	0.0568	0.0201	0.0574	0.0185
2°	0.119	0.023	0.1194	0.0216
3°	0.1816	0.0281	0.1818	0.0269
4°	0.2443	0.0354	0.2447	0.0345
5°	0.3085	0.0452	0.308	0.0444
6°	0.3719	0.0564	0.3724	0.0571
7°	0.4377	0.0711	0.4383	0.0719
8°	0.505	0.0884	0.5044	0.0891
9°	0.5744	0.1086	0.5707	0.1085
10°	0.6468	0.1318	0.6385	0.1304
11°	0.7239	0.1587	0.7102	0.1555
12°	0.8081	0.1894	0.7833	0.1835

Even though the focus of this study is on the supersonic flight regime, subsonic simulation was conducted to observe the differences between configuration behaviors. Figures 38. through 41. show pressure and velocity distribution during subsonic flight.

It can clearly be seen how there are local supersonic regions at both of the airfoils. There are differences however. Figure 38 shows almost fully developed shockwave at around 0.6c, whereas figure 40 shows how the airfoil in supersonic configuration does not exempt such behavior. There are 2 shockwaves in creation under the specified circumstances. One on the upper and one on the lower surface, and they both are weaker than the shockwave from figure 38. The creation of a single stronger shockwave is more suitable than having multiple shockwaves and regions of diverse changes throughout the airfoil. Figures 39 and 41 show the pressure coefficient changes following the shockwaves.

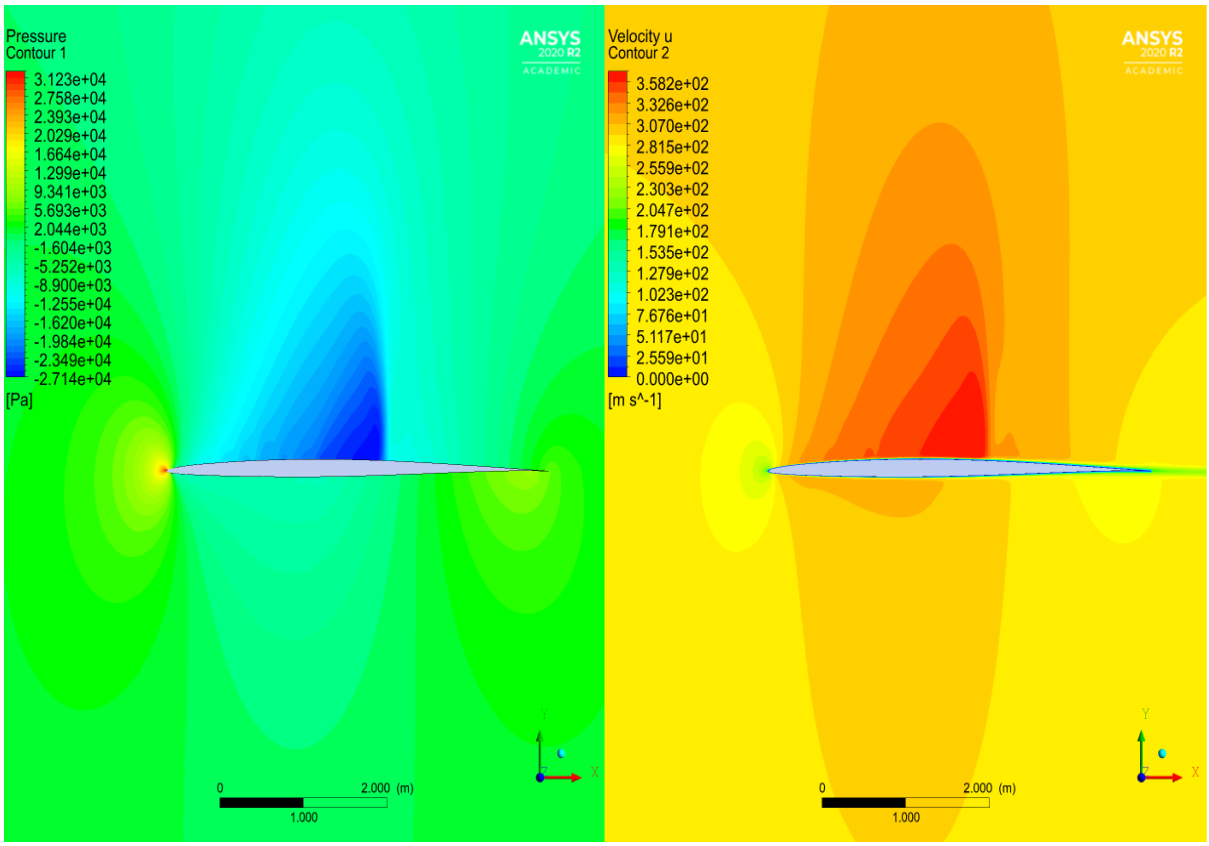

Figure 38. Pressure and velocity distribution, Ma=0.85, AoA = 0 °, subsonic cruise configuration

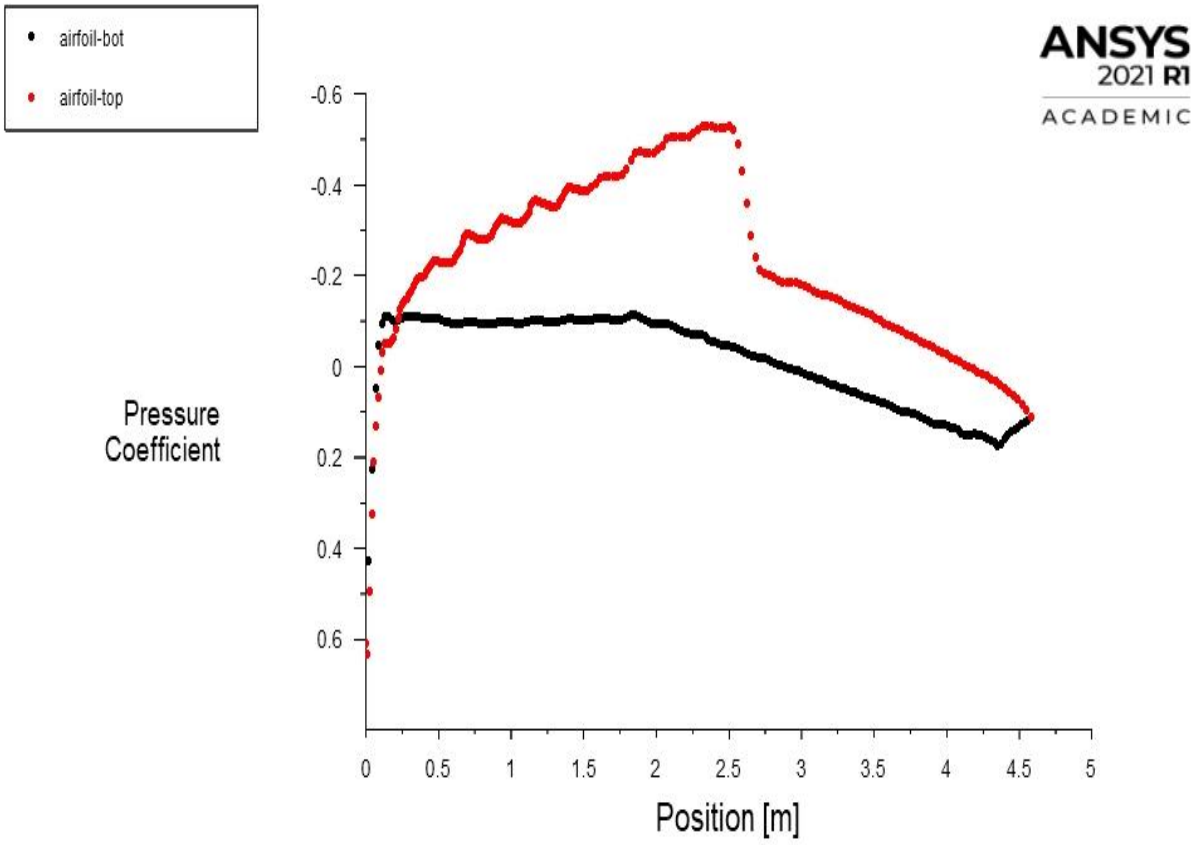

Figure 39. Pressure coefficient distribution for subsonic cruise configuration at Ma=0.85, and AoA=0°

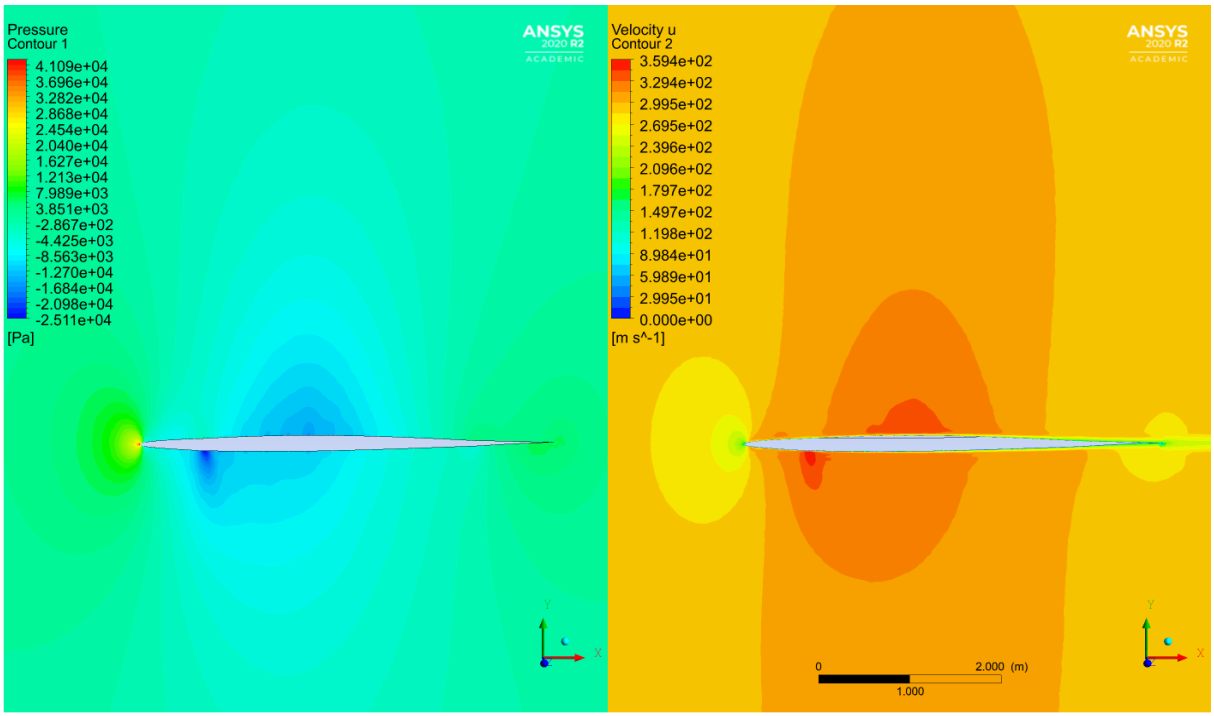

Figure 40. Pressure and velocity distribution, Ma=0.85, AoA=0°, supersonic cruise configuration

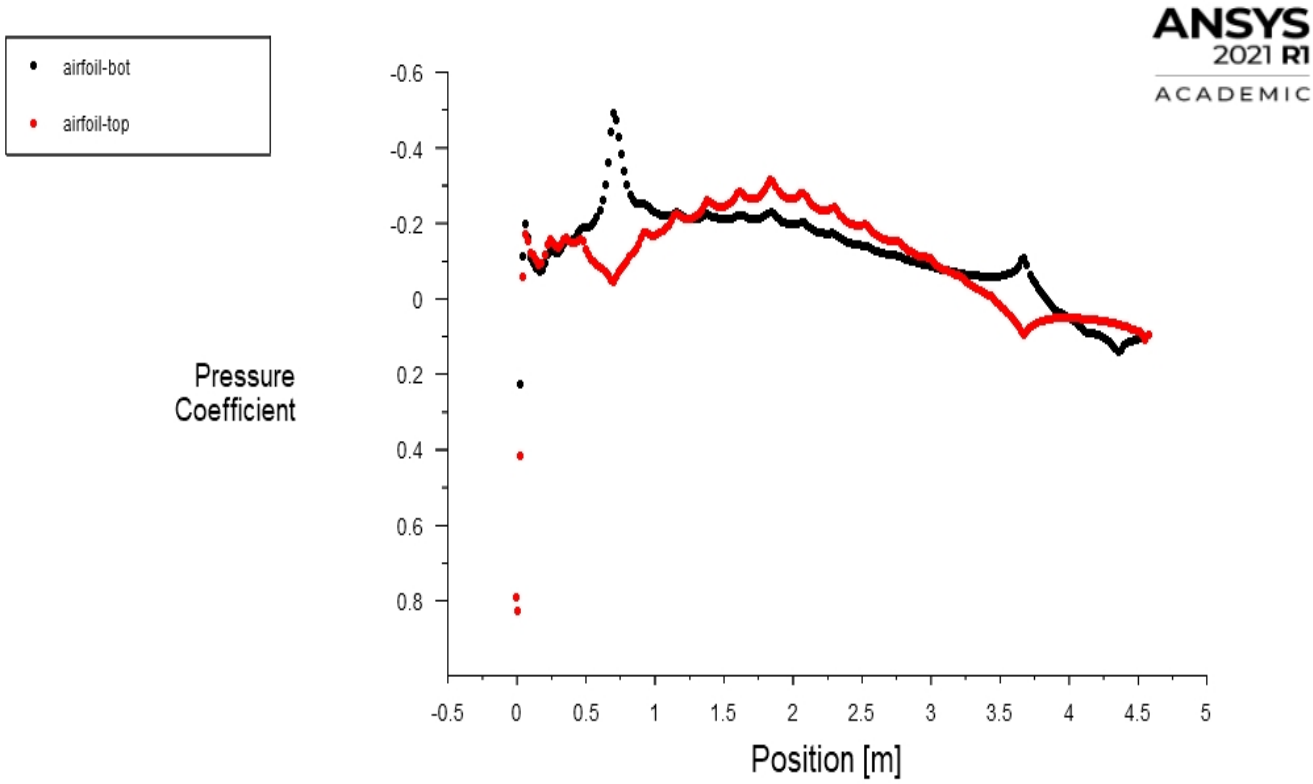

Figure 41. Pressure coefficient distribution for supersonic cruise configuration at Ma=0.85, and AoA=0°

Finally, let us observe how the velocity and pressure distribution changes with the change in angle of attack for a peculiar configuration called high ‘g’ maneuver. It is a configuration used only for performing turns at high speeds and high velocities – hence its

name. Simulations were conducted for the high ‘g’ maneuver configuration at Ma=0.54 for angles of attack ranging from 0:10. The configuration is intended to be used at subsonic conditions. Figures 42 to 45 show CFD fluid airfoil interaction at Ma=0.54 and AoA = 0° & 10°.

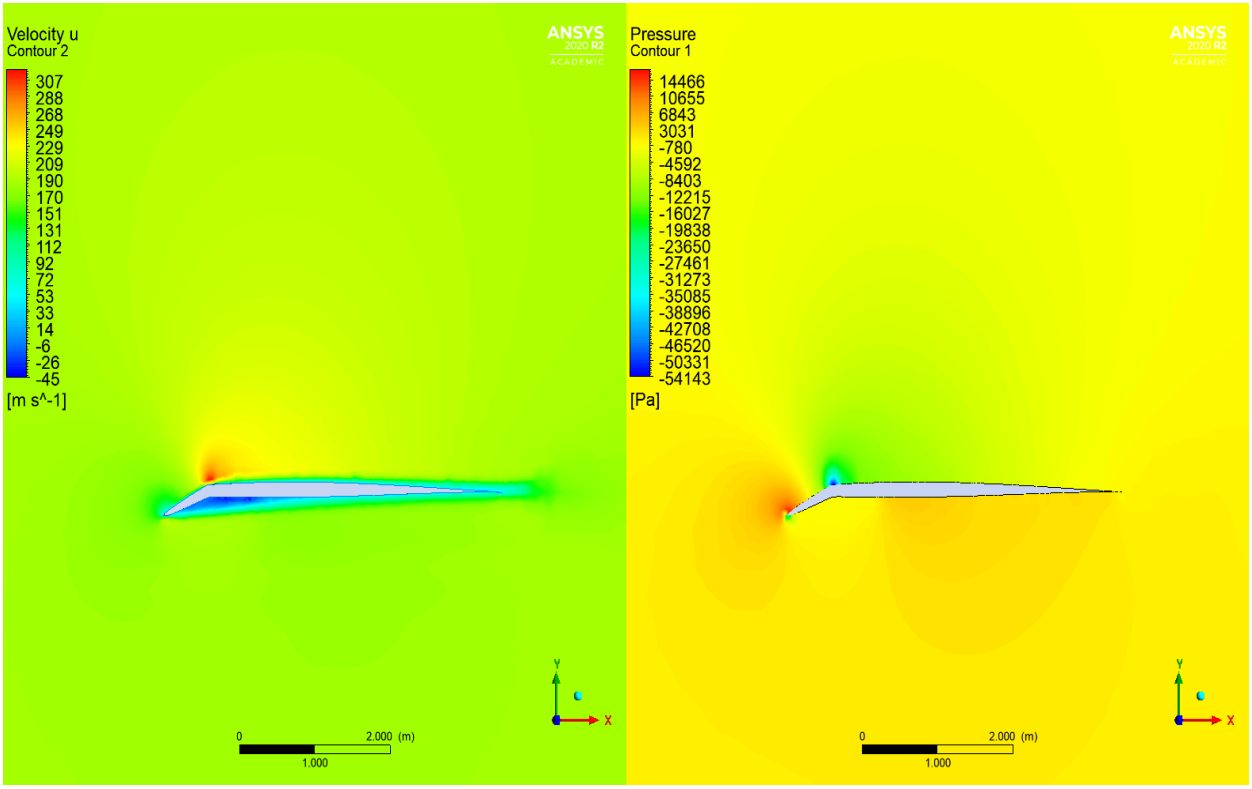

Figure 42. Velocity and pressure contours for high 'g' maneuver configuration at Ma=0.54 and AoA=0°

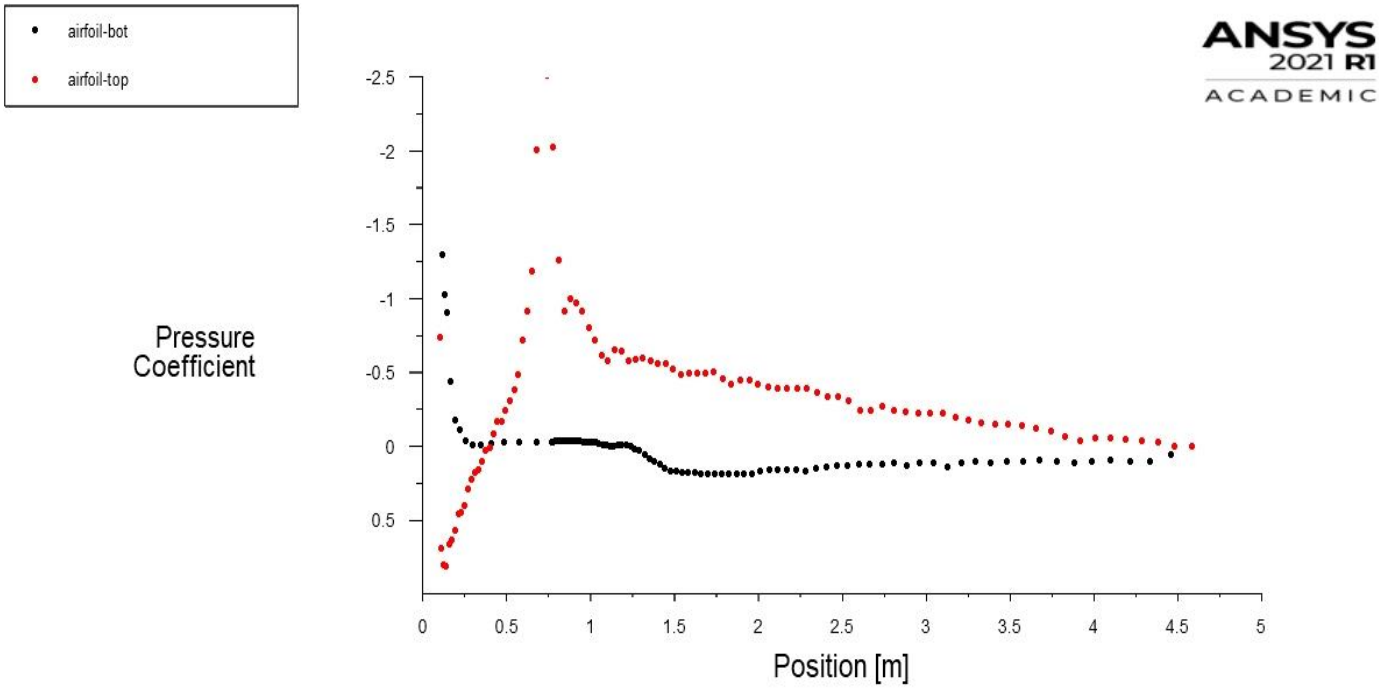

Figure 43. Pressure coefficient distribution along upper and lower surfaces for high 'g' maneuver configuration at Ma=0.54 and AoA=0°

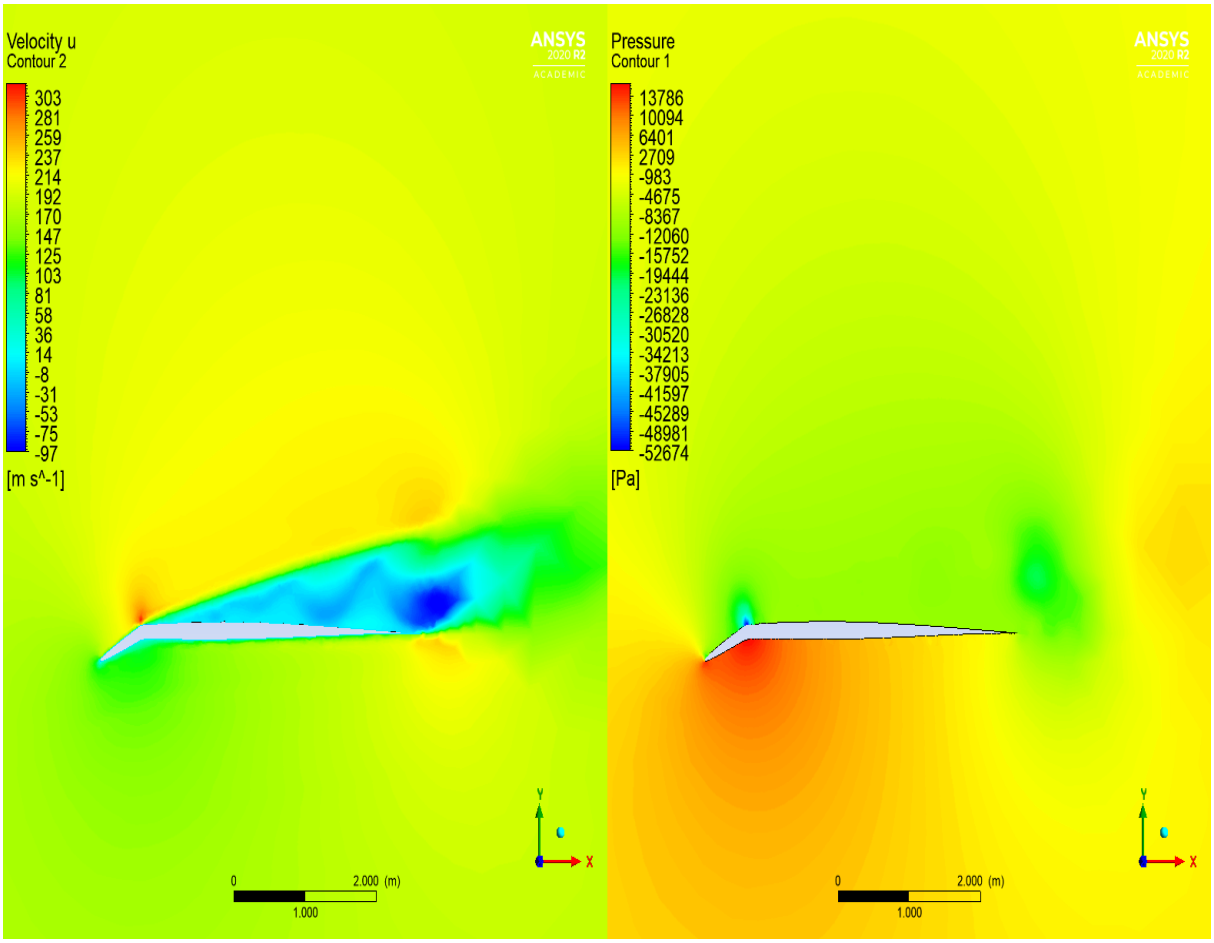

Figure 44. Velocity and pressure contours for high 'g' maneuver configuration at Ma=0.54 and AoA=10°

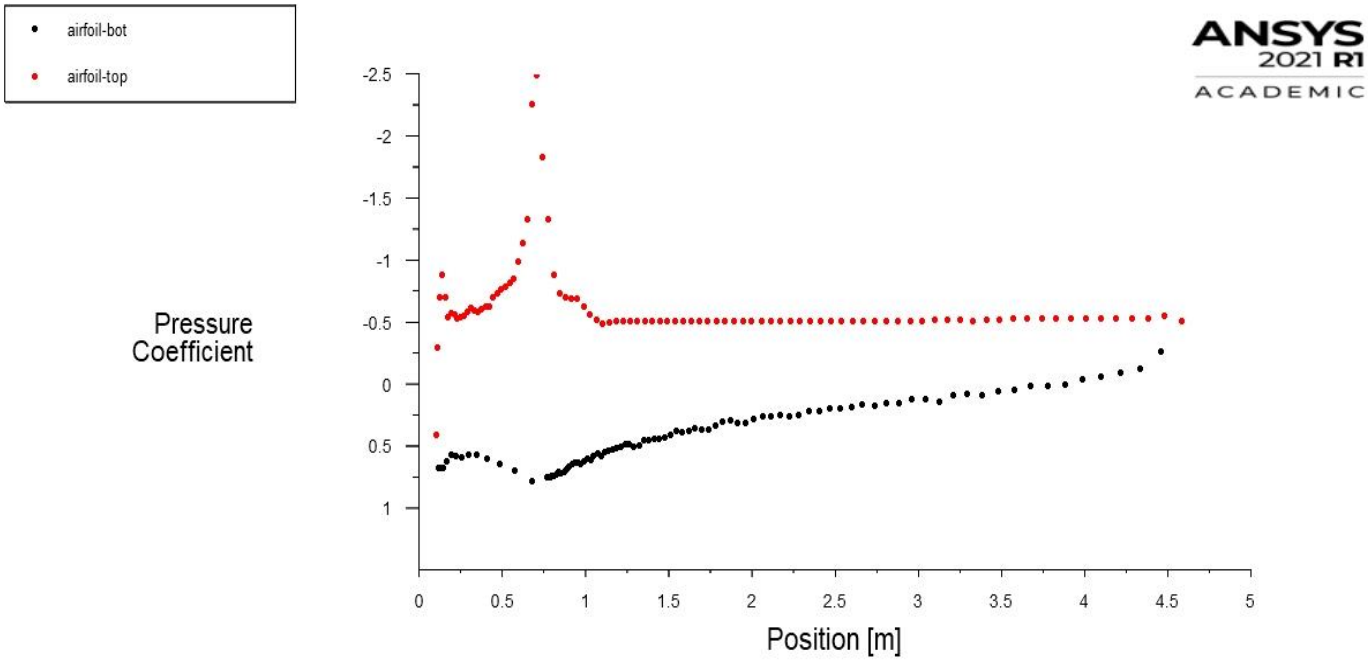

Figure 45. Pressure coefficient distribution along upper and lower surfaces for high 'g' maneuver configuration at Ma=0.54 and AoA=10°

6. Discussion

In the previous chapters two methods of calculating lift, drag and pressure coefficients were discussed. Firstly, the calculations were approached via theoretical analysis based on the analytical terms that ignore viscous effects and can be used only for thin airfoils without adverse changes in the shape of the airfoil. All the terms and formulas were based on the thin airfoil linearized theory. In order to validate the results obtained by the linear theory, CFD study was conducted under the same conditions and for the same airfoil configurations. Since the linear theory is known only to be correct for airfoils without adverse changes in pressure gradients – it could only be applied to the two configurations which didn't have sudden or steep changes in their airfoil shapes. The two positions mentioned are the subsonic and supersonic cruise configurations. The only difference between those two configurations is that the supersonic cruise configuration has its nose and rear deflected by -2 degrees. That reduces the camber line to almost none. By reducing the camber line, small but sufficient effect is achieved – and that is drag reduction. All the studies were conducted under the Ma=1.5 velocity. Further analysis under different conditions, such as Ma higher than 1.5, going all the way up to maximum speed at full usage of afterburner at around Ma~2 could possibly yield additional results and confirmation on just how impactful is the two-degree deflection in airfoil surface.

On the figure 46 there are four data sets which represent pressure distribution over the top and bottom surfaces of the airfoil. Dashed lines are values obtained through the analytical terms of the linearized theory, and the dotted lines are values calculated by the CFD approach via the ANSYS software. The correlation is very acceptable.

It can be seen how the CFD lines are smoother, and do not have the steps that can be seen in the dashed lines. The steps happen because of the coordinate points distribution in the MATLAB.

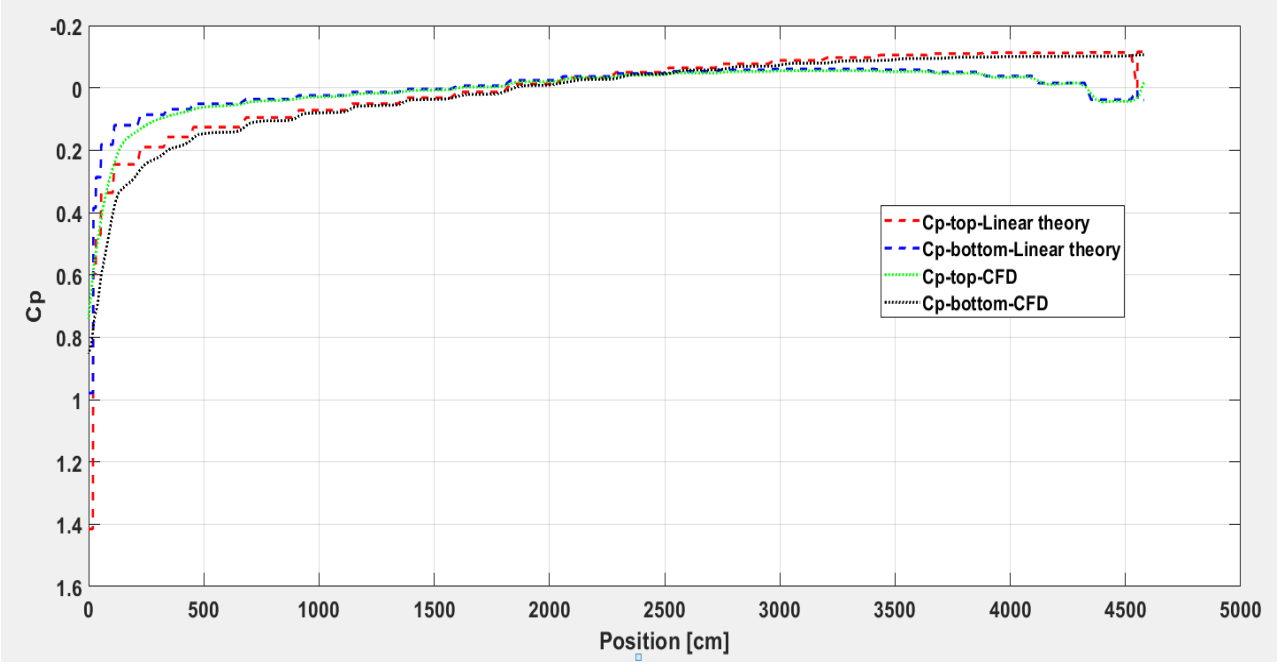

Figure 46. Pressure coefficient distribution comparison for linear and CFD approaches for Ma=1.5, AoA=0°, subsonic cruise configuration

It can be seen how the pressure coefficient distribution is almost identical. There is a larger value of pressure coefficient at the leading edge of the airfoil in the MATLAB results, however the rest of the graph aligns in a very solid manner.

In a similar matter, figure 47 shows the comparison of the pressure coefficient distribution between values obtained in MATLAB and in ANSYS for the supersonic cruise configuration. The results are very similar.

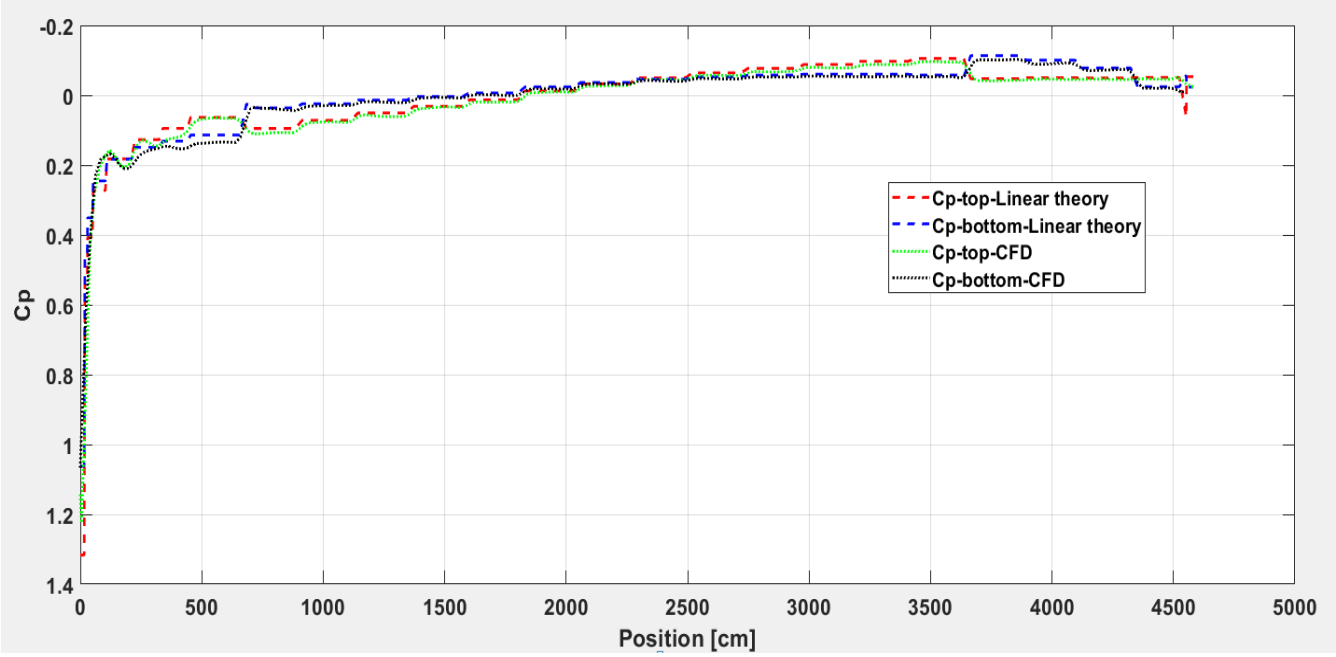

Figure 47 Pressure coefficient distribution comparison for Ma=1.5, AoA=0°, supersonic cruise configuration

Figure 48 shows how the lift and drag coefficients change by changing the angle of attack. Changes shown are based on both the linear and CFD calculations.

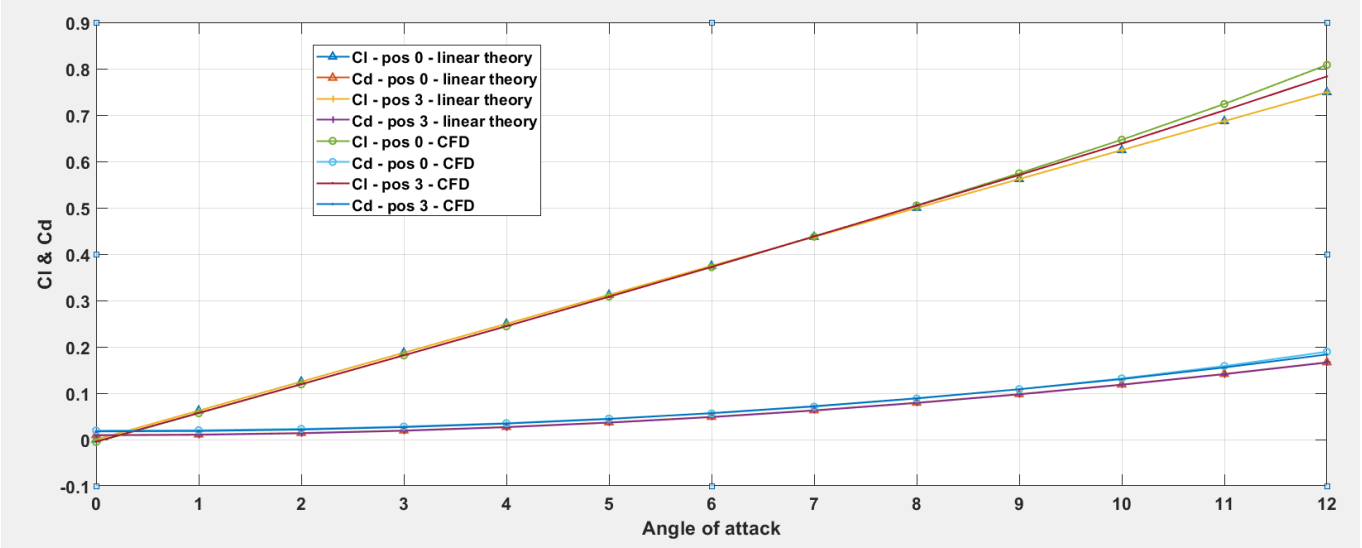

Figure 48. Lift and drag as functions of angle of attack for positions 0 and 3, obtained by both linear theory and CFD approach, for Ma=1.5 and AoA=0:12

Next, on the following figure, 49, comparison is shown between the lift and drag values obtained for AoA = 0:12, under the Ma =1.5 condition, by linear theory and by CFD. The main

difference is in the predicted drag coefficient. As expected it is greater in the CFD analysis due to viscous effects.

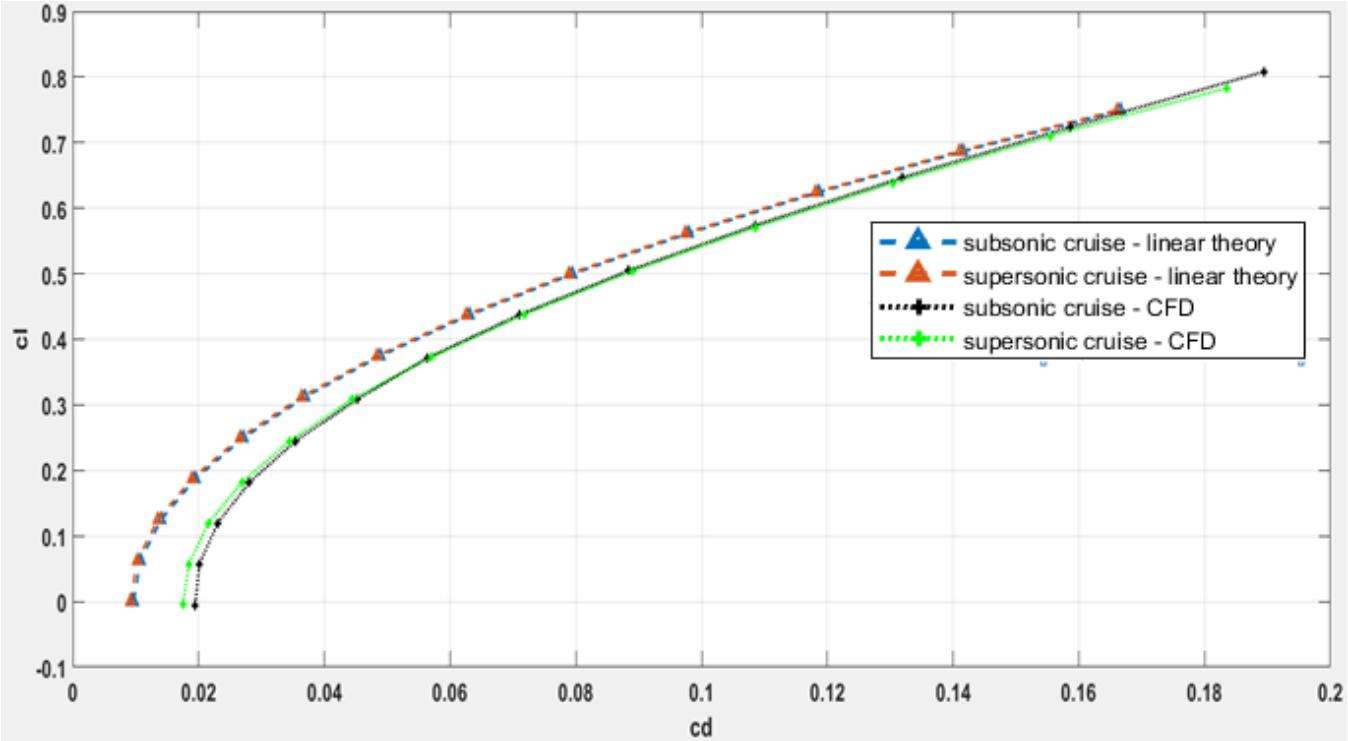

Figure 49. MATLAB and ANSYS lift and drag coefficients comparison for Ma=1.5, AoA=0:12

And finally, on the figure 50 lift do drag ratio against angle of attack is shown for both approaches.

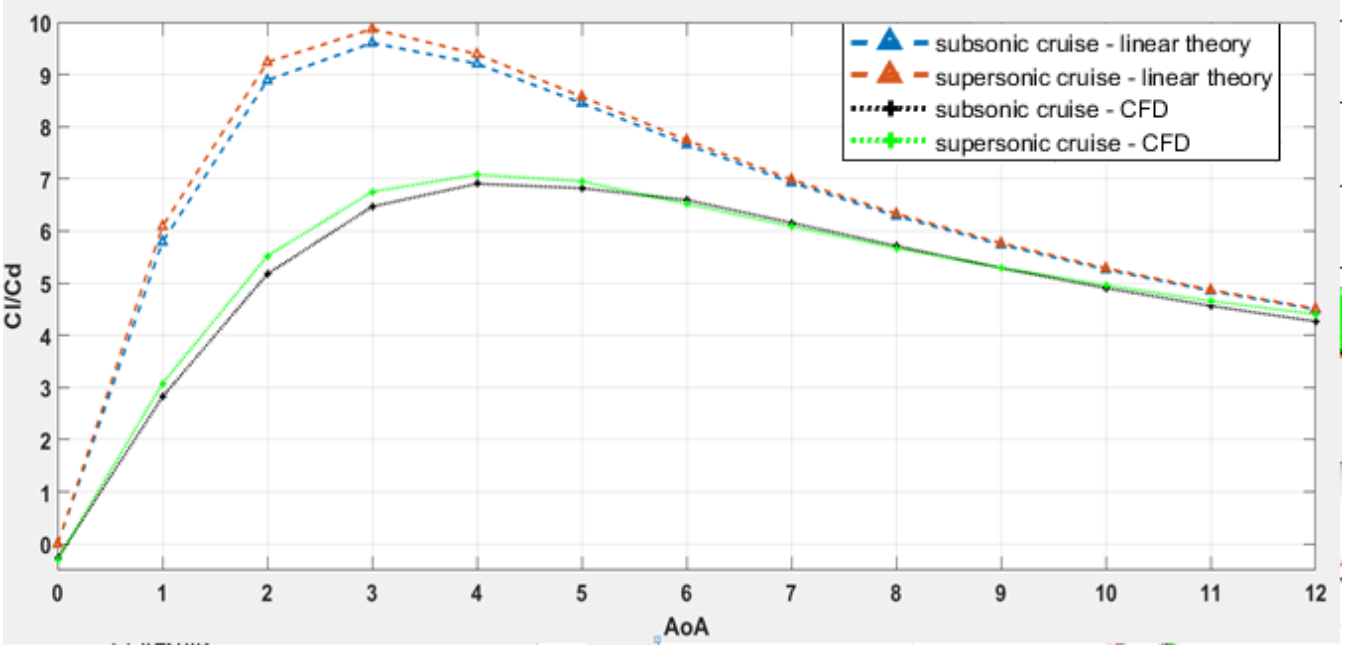

Figure 50. Lift to drag ratio for linear and CFD approaches, Ma=1.5, AoA=0:12

It is interesting to observe how both approaches seem to give equal results of Cl/Cd values at higher angles of attack. Even though drag predictions of the linear theory are lower at smaller angles of attack, they start increasing as the angle of attack increases. This behavior is

explained by the term (31) derived in the chapter 2.3. which states how drag value depends on three factors, drag due to thickness, drag due to camber and drag due to **angle of attack.**

Figures 49. And 50. both show how the supersonic configuration provides higher value of lift coefficient to lower value of drag coefficient, thus making it more efficient to use for cruising at higher Ma values. Especially at angles of attack ranging from 1 to 5 degrees. This effect is obtained by reducing the camberline of the airfoil to zero, instead of the standard 2 degree for subsonic cruise configuration. It is reasonable to assume how a supersonic aircraft while cruising at supersonic speeds will not fly at angles of attack larger than 5 degrees.

Table 5. Difference in supersonic cruise configuration and subsonic cruise configuration for lift to drag coefficient ratio, values obtained by linear theory and CFD

Angle of Attack [°]	Linear theory	CFD
	Difference in Cl/Cd ratio for supersonic cruise configuration [%]	Difference in Cl/Cd ratio for supersonic cruise configuration [%]
0	0	-6.71
1	5.16	10.31
2	3.91	6.95
3	2.79	4.5
4	1.99	2.72
5	1.45	1.77
6	1.09	-1.03
7	0.84	-0.99
8	0.67	-0.84
9	0.54	-0.57
10	0.45	-0.17
11	0.37	0.11
12	0.32	0.05

Table 5 shows just how big of an impact does 2 degree camberline difference makes. At 1-degree angle of attack, there is 5.16% based on linear theory, and 10.31% increase based on the CFD approach of the lift to drag coefficient ratio. For a supersonic flight regime which relies heavily on fuel consumption, utilizing full afterburner effects, such an increase plays a detrimental role.

7. Conclusion

The research goal of this project was to evaluate the impact of the variable geometry airfoil used in the F-16 wings. However, the aim was also to provide insight in just how correct and reliable the linear theory for calculating lift and drag coefficients was. Linear theory is known to provide satisfying results only for slender body airfoils without steep changes in the airfoil surfaces. CFD techniques however, are improving every day, and it is now possible to conduct simulations for very complex aerodynamical bodies with great precision.

At the beginning of the thesis, theoretical analysis was given along with the introduction of the linear theory and its application by the MATLAB software for the airfoil analysis. Somewhat later, CFD techniques were discussed in detail and results obtained via simulations were presented in multiple tables and figures. It is worth noting how the CFD application in this paper was only a tip of the iceberg, for CFD has much greater capacities for real world usage. Engineers today are using CFD methods for solving sets of equations with over billion unknown variables over highly complex shapes in 3D space.

Linear theory certainly has its limitations and its results can be very linear and untrue. In figure 14. it is shown how the lift to drag curve predicted by the linear theory is perfectly symmetric for angles of attack ranging from -24 deg to 24 deg. That cannot be the case during real flight. In table 2 it can be seen how the lift coefficient values are exactly the same for both subsonic and supersonic airfoil configurations for angles of attack ranging from 0 to 12 deg at Ma=1.5. The reason for that is that the linear theory predicts lift coefficient on an analytical term which takes only the angle of attack as a deciding parameter. However, on following figures, 15 and 16, linear theory predicted pressure distribution can be seen along the upper and lower surfaces of the airfoil.

Later in the paper, by conducting the CFD analysis which takes forces like viscosity, friction and wall shear stresses it can be observed how the pressure distribution predicted by ANSYS Fluent aligns very closely with the pressure distribution predicted by the linear theory. Furthermore, the results for lift and drag coefficients for the subsonic and supersonic configurations, given by the CFD, also match the results obtained by the linear theory. They do not align perfectly, which was expected, however they match very closely taking into consideration how simple and easy the linear theory is.

The real value of the CFD approach is the visualization of the fluid flow field around the airfoil. In later chapters, figures are presented which demonstrate just how the pressure and velocity are distributed around the airfoil for given conditions. Using the information provided by the simulation, aircraft designers are able to pinpoint places of major phenomena, such as shockwave position, the stagnation point, or just to determine the place where the maximum velocity and/or minimum pressure is present. None of those occurrences have been previously possible to capture without sophisticated and complicated techniques involving wind tunnels and different methods for visualization of the flow field.

Finally, in the discussion chapter figures which contain results obtained by both the linear theory and the CFD approach are compared, and it can be seen just how close the pressure distributions are, thus further validating the results obtained by both the linear theory and CFD methods for thin airfoil bodies. On the final two figures, it can be seen how the supersonic

cruise configuration yields greater values for the lift coefficient under the supersonic (Ma=1.5) flight regime. That was the aim of the research, to prove why the supersonic cruise configuration is used. The difference is greatest for angles of attack from 1 to 5. Even though the subsonic cruise configuration values of lift coefficient start matching the supersonic cruise configuration at angles of attack larger than 5, it is highly unlikely that the F-16 will cruise at supersonic speeds at larger angles of attack.

The F-16 variable camber airfoil has many advantages. It is able to provide higher lift coefficients during take-off and ground roll, it can then easily translate to subsonic cruise configuration and thus elevate to heights at about 35 000ft and cruise efficiently. If necessary the aircraft can turn on the afterburner, followed by reduction of the airfoil camber, and go into full supersonic mode

References

[1] J. John D. Anderson, Modern Compressible Flow, New York: McGraw-Hill, 2003..

[2] j. John D. Anderson, Fundamentals of Aerodynamics, New York: McGraw-Hill, 2001..

[3] E. N. W. K. E. P. R. M. Jacobs, "The characteristics of 78 related airfoil sections from tests in the variable-density wind tunnel," NACA, 1935..

[4] Stanford edu., "The NACA airfoil series".

[5] R. Fitzpatrick, "Fluid Mechanics," 2016.. [Online]. Available: https://farside.ph.utexas.edu/teaching/336L/Fluid/Fluidhtml.html. [Accessed 20 March 2021.].

[6] M. D. V. Dyke, *A study of second order supersonic flow*, Pasadena: California Institute of Technology, 1949.

[7] E. Angelo Miele, Theory of Optimum Aerodynamic Shapes, New York: Academic Press, 1965..

[8] A. Ferri, "Experimental Results with Airfoils Tested in the High-Speed Tunnel at Guidonia," NACA TM 946, Guidonia, 1940.

[9] Airfoil tools, "Airfoil tools," [Online]. Available: http://airfoiltools.com/index. [Accessed 21. January 2021.].

[10] L. Milne-Thomson, Theoretical Aerodynamics. Physics of Fluids A., Dover Publications, 1973..

[11] L. F. Richardson and S. Chapman, Weather prediction by numerical process, Dover Publications, 1965..

[12] L. F. Richardson, Lewis Fry Richardson and his contributions to mathematics, meteorology, and models of conflict, Dover Publications, 1922..

[13] A. S. J.L.Hess, "Calculation of potential flow about arbitrary bodies," *Progress in Aerospace Sciences*, vol. 8, pp. 1-138, 1967.

[14] ANSYS, Inc., Ansys help manual, Canonsburg, Pennsylvania: Ansys, 2021.

[15] M. F.R., "Two-Equation Eddy-Viscosity Turbulence Models for Engineering Applications," *AIAA Journal*, vol. 32, no. 8, pp. 1598-1605, 1994..

[16] J. John D. Anderson, Computational Fluid Dynamics, The Basics with Applications, New York: McGraw-Hill, 1995..

[17] U.S. Air force, "Air Force," September 2015.. [Online]. Available: https://www.af.mil/About-Us/Fact-Sheets/Display/Article/104505/f-16-fighting-falcon/. [Accessed 21. January 2021.].

[18] W. Mason, *Supersonic Aerodynamics*, Seattle, 2016..

[19] I. Ibrahim, E. Ng and K. Wong, ""Flight Maneuverability Characteristics of the F-16 CFD and Correlation with its Intake Total Pressure Recovery and Distortion".," *ngineering Applications of Computational Fluid Mechanics*, pp. 223-224, 4 November 2014..

[20] Jane's All The World's Aircraft, *Lockheed Martin F-16 Fighting Falcon*, Chicago, 2008..

[21] J. E. W. Carl S. Droste, "A case study on F-16 fly-by-wire flight control system," General Dynamics, Chicago.

List of Figures

Appendix A.

The standard **k-e** transport equations for kinetic turbulent energy (**k**), and dissipation of kinetic energy (**epsilon**) are as follows:

$$\frac{\partial(\rho k)}{\partial t} + \nabla \cdot (\rho \boldsymbol{U} k) = \nabla \cdot \left(\left(\mu + \frac{\mu_t}{\sigma_k} \right) \nabla k \right) + P_k - \rho \epsilon \tag{1}$$

$$\frac{\partial(\rho \epsilon)}{\partial t} + \nabla \cdot (\rho \boldsymbol{U} \epsilon) = \nabla \cdot \left(\left(\mu + \frac{\mu_t}{\sigma_k} \right) \nabla \epsilon \right) + C_{1\epsilon} P_k \frac{\epsilon}{k} - C_{2\epsilon} \rho \frac{\epsilon^2}{k} \tag{2}$$

By substituting the term:

$$\epsilon = C_\mu k \omega \tag{3}$$

Into the dissipation equation of the **k-e** model we get a term that is identical to the transport equation for the specific dissipation of the k-w model with one additional term:

$$\frac{\partial(\rho \omega)}{\partial t} + \nabla \cdot (\rho \boldsymbol{U} \omega) = \nabla \cdot \left(\left(\mu + \frac{\mu_t}{\sigma_k} \right) \nabla \omega \right) + \frac{\gamma}{\nu_t} P_k - \beta \rho \omega^2 + \underbrace{2 \frac{\rho \sigma_{\omega 2}}{\omega} \nabla k : \nabla \omega}_{\text{Additional Term}} \tag{4}$$

The Transport equation for the specific turbulence dissipation rate used in the k-w model is:

$$\frac{\partial(\rho \omega)}{\partial t} + \nabla \cdot (\rho \boldsymbol{U} \omega) = \nabla \cdot \left(\left(\mu + \frac{\mu_t}{\sigma_k} \right) \nabla \omega \right) + \frac{\gamma}{\nu_t} P_k - \beta \rho \omega^2 \tag{5}$$

In order to blend those two models, a new blending function is introduced to allow for smooth transition between models. The **F1** function – the blending function – is a function that can take any value from 0 to 1 and if the function **F1 = 0** then the additional term exists and **k-e** model is in use, however if the function has a value of **F = 1**, then the product of **(1-F1)** with the additional term is equal to 0, and then the **k-w** model is used.

$$2(1 - F_1) \frac{\rho \sigma_{\omega 2}}{\omega} \nabla k : \nabla \omega \tag{6}$$

The term $\nabla k : \nabla w$ isn't the most commonly used notation, it represents the tensor inner product of the two gradient terms (the kinetic energy, and the specific dissipation rate). In its full form it can be written as:

$$\nabla k : \nabla \omega = \frac{\partial k}{\partial x_j}\frac{\partial \omega}{\partial x_j} = \frac{\partial k}{\partial x}\frac{\partial \omega}{\partial x} + \frac{\partial k}{\partial y}\frac{\partial \omega}{\partial y} + \frac{\partial k}{\partial z}\frac{\partial \omega}{\partial z} \tag{7}$$

The **F1** function is a scalar field function. Each cell in the mesh has a **F1** value assigned to it. All the variables calculated at each cell center are affected with the value of the blending function. Every cell in the mesh is going to have a different value of **F1**.
On the figure below is a portion of a mesh near the wall. The **k-w SST** model guides the software to use the **F1 = 0**, or the **k-e** model calculations for the cells which are further away from the wall, and **F1 = 1** or the **k-w** model for the cells which are next to the wall.

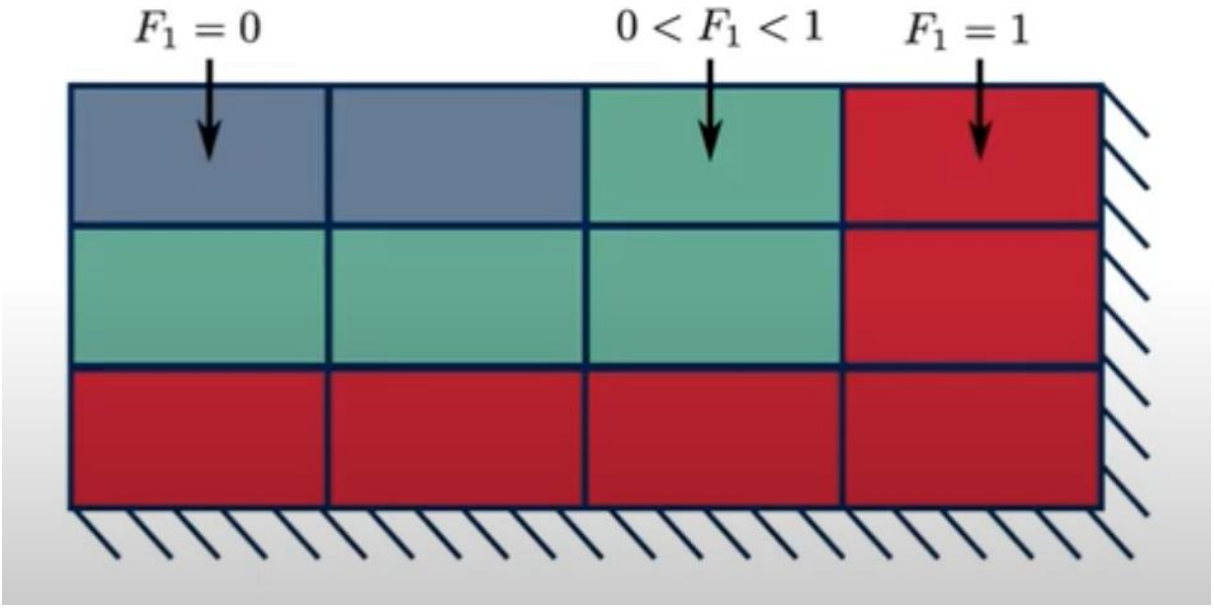

Figure 51. Near wall treatment

The current form used for the **F1** function is a hyperbolic tangent function

$$F1 = \tanh(\arg 1^4) \tag{8}$$

And the reason why it is a hyperbolic tangent function, is because it gives a really smooth transition from one model to another. Whatever the argument for the function is, on the figure below it can be seen that when the argument is small the **k-e** model is used, and when the argument increases the **F1** function will tend towards the value of **1** which will activate the **k-w** model.

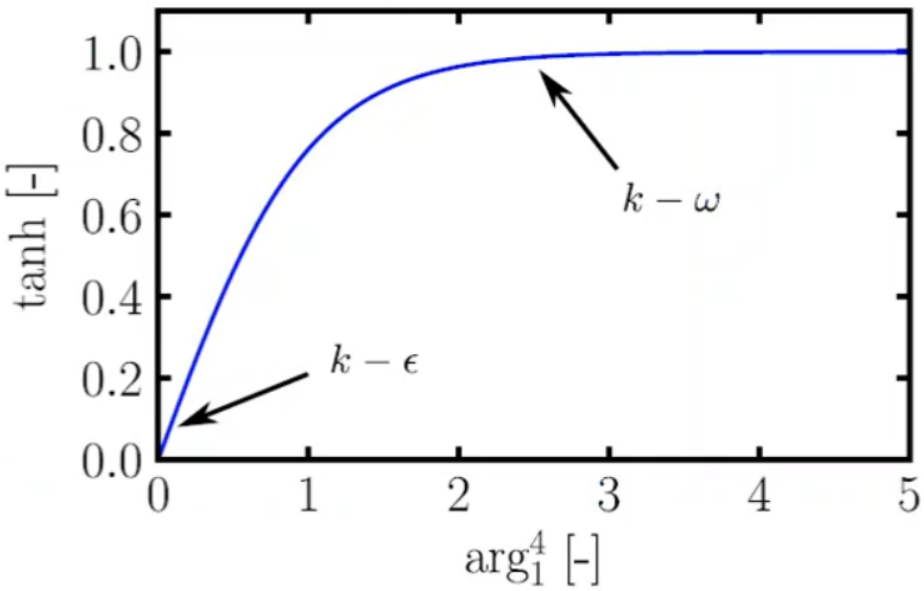

Figure 52. Hyperbolic tangent function behavior

Arg1 depends on the distance closest to the wall **d**. It is not necessary to discuss all the arguments in the function because the important factor for this discussion is the distance from the wall **d**. For additional information see reference.

$$\arg_1 = \min\left[\max\left(\frac{\sqrt{k}}{\beta^{\star}\omega d}, \frac{500\nu}{d^2\omega}\right), \frac{4\rho\sigma_{\omega 2}k}{CD_{k\omega}d^2}\right] \tag{9}$$

As can be seen every cell in the mesh will have a value of **d** assigned to it which will be defined by its distance to the closest wall. By decreasing the value **d**, **arg1** increases, and the **F1** then increases and thus the model switches to **k-w** model for the near wall treatment.

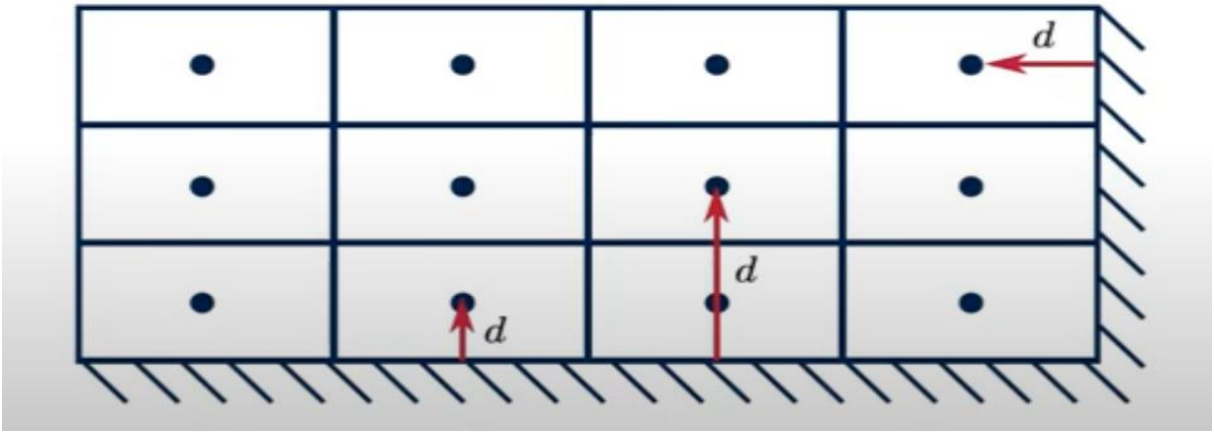

Figure 53. Distance to the wall determination

However, even with the usage of the blending function **F1** it was noted how the simulations still overpredicted the wall shear stress. That is why the **viscosity limiter** is introduced. And the **viscosity limiter** looks like the term in equation 10. On the left side of the term is the original form for the turbulent dynamic viscosity, and that is the term that needs to be limited. So by reducing the viscosity when the cells are near the wall, when the shear is high, the shear stress will get reduced faster and it is more likely to achieve separation. The viscosity limiter will

return to the original viscosity form if the product of **S** and **F2** are small, and that will happen far away from the wall. However, if the product of **S** and **F2** is large then the turbulent viscosity will be limited and will be smaller than what would be achieved by the original models.

$$\underbrace{\mu_t = \frac{\rho k}{\omega}}_{\text{Original}} \qquad \underbrace{\mu_t = \frac{a_1 \rho k}{\max\left(a_1 \omega, S F_2\right)}}_{\text{SST Model}} \tag{10}$$

S is the magnitude of the shear strain, and **F2** is another blending function. **F2** is empirically calibrated. **F2** also takes the form of the hyperbolic tangent function form so to ensure that the transition between the original viscosity and the limited viscosity is smooth. **Arg2** also depends on the distance to the nearest wall **d.** As **d** reduces the software is closer to the wall, the argument decreases and therefore **F2** increases and thus limits the turbulent viscosity.

$$\begin{aligned} F_2 &= \tanh\left(\arg_2^2\right) \\ \arg_2 &= \max\left(\frac{2\sqrt{k}}{\beta^\star \omega d}, \frac{500\nu}{\omega d^2}\right) \end{aligned} \tag{11}$$

After extensive analysis and improvements, it is safe to say that the **k-w SST** model gives much better agreement with experiments for external aerodynamic applications such as flow over wings or flow over an airfoil.

DECLARATION OF ACADEMIC INTEGRITY AND CONSENT

I declare and confirm by my signature that this diplomski rad
is an exclusive result of my own work based on my research and relies on published literature,
as can be seen by my notes and
references.
I declare that no part of the thesis is written in an illegal
manner,

nor is copied from unreferenced work, and does not infringe upon anyone's copyright.

I also declare that no part of the thesis was used for any other work in

any other higher education, scientific or educational institution.

I hereby confirm and give my consent for the publication of my diplomskog rada

titled **Aerodynamic Characteristics Estimation of Variable Geometry Airfoil in Supersonic Air Flow**

on the website and the repository of the Faculty of Transport and Traffic Sciences and

the Digital Academic Repository (DAR) at the National and University Library in Zagreb.

Student:

In Zagreb, 29 April 2021 Leo Matak

(signature)